2014-12-01

Synthesis and Characterization of Complex Molecular Assemblies on Surfaces

Nitesh Madaan
Brigham Young University - Provo

Synthesis and Characterization of Complex Molecular Assemblies on Surfaces

Nitesh Madaan

A dissertation submitted to the faculty of
Brigham Young University
in partial fulfillment of the requirements for the degree of

Doctor of Philosophy

Matthew R. Linford, Chair
Adam T. Woolley
John N. Harb
David V. Dearden
Daniel E. Austin

Department of Chemistry and Biochemistry
Brigham Young University
December 2014

ABSTRACT

Synthesis and Characterization of Complex Molecular Assemblies on Surfaces

Nitesh Madaan
Department of Chemistry and Biochemistry, BYU
Doctor of Philosophy

The research presented in this dissertation is focused on the construction of complex molecular structures on planar gold and silicon dioxide surfaces using a variety of surface modification techniques, along with thorough surface characterization at each modification step. The dissertation is structured into six separate chapters. In Chapter 1, an introduction to the importance and implications of molecular level surface modification, commonly employed surface modification methods, and available surface characterization techniques is presented. Chapter 2 shows applications of novel methodologies for the functionalization of gold surfaces using alkane dithiol self-assembled monolayers and thiol-ene click chemistry. The resulting functionalized gold substrates demonstrate higher chemical stability than alkanethiol self-assembled monolayers alone and allow spatially controlled functionalization of gold surfaces with light. In Chapter 3, work on tunable hydrophobic surfaces is presented. These surfaces are prepared using a combination of organosilane chemistry, layer-by-layer polyelectrolyte deposition, and thiol-ene chemistry. These hydrophobic surfaces demonstrate high mechanical and chemical stability, even at low pH (1.68). The pinning of water droplets could be tuned on them by the extent of their thermal treatment. Comprehensive surface characterization using X-ray photoelectron spectroscopy (XPS), time-of-flight secondary ion mass spectrometry (ToF-SIMS), spectroscopic ellipsometry, atomic force microscopy, and water contact angles was carried out on the molecular assemblies prepared on gold and silicon dioxide surfaces. Chapters 4 and 5 are focused on the application, data interpretation, and enhancement in sensitivity of different surface characterization methods. In Chapter 4, XPS, ToF-SIMS, and principal components analysis are used to probe a real world corrosion-type problem. This systemic study showed the destruction of a protective coating composed of a nitrilotris(methylene)triphosphonic acid by a low-intensity fluorine plasma. In Chapter 5, enhancement in ToF-SIMS signals is shown via bismuth metal deposition. These surfaces are also probed by spectroscopic ellipsometry using the interference enhancement method. Finally, Chapter 6 concludes this dissertation by describing possible future work.

Keywords: Self-assembled monolayer (SAM), X-ray photoelectron spectroscopy (XPS), time-of-flight secondary ion mass spectrometry (ToF-SIMS), ellipsometry, water contact angle, thiol-ene click chemistry, layer-by-layer (LBL) polyelectrolyte deposition, silane chemistry, gold, thiol, hydrophobic, metal assisted SIMS (meta-SIMS), interference enhancement method.

ACKNOWLEDGEMENTS

I am sincerely thankful to Dr. Matthew R. Linford for the guidance, support, encouragement, patience as a PhD guide, and especially for being a wonderful teacher.

I thank my committee members Dr. Adam T. Woolley, Dr. John N. Harb, Dr. David V. Dearden, and Dr. Daniel E. Austin for their support and insightful suggestions.

I am thankful to fellow graduate students Dr. Feng Zhang, Dr. Gaurav Saini, Dr. Lei Pei, Dr. Tony Pearson, Dr. David S. Jensen, Dr. Landon A. Wiest, Anubhav Diwan, Hao Wang, Supriya Kanyal, Chuan-Hsi Hung, and Bhupinder Singh for their support and collaboration.

I thank the Department of Chemistry and Biochemistry, Brigham Young University for the opportunity to pursue graduate studies in analytical chemistry.

I am grateful to my family, especially my mother Smt. Bhagwan Devi, for their unconditional love and support.

TABLE OF CONTENTS

LIST OF SCHEMES ix

LIST OF FIGURES x

LIST OF TABLES xiv

Chapter 1: Introduction to Surface Modification and Characterization 1

1.1. Introduction 1

1.2. Surface Chemistry 4

1.2.1. Self-Assembled Monolayers 4

1.2.1.1. Organosilane Chemistry 5

1.2.1.2. Thiol Monolayers on Gold 6

1.2.1.3. Organophosphonic Acid SAMs 8

1.2.2. Layer-by-Layer Deposition 9

1.2.3. Thiol-Ene Click Chemistry 11

1.2.4. Miscellaneous Chemistries 13

1.2.5. Coupling Chemistries 13

1.3. Surface Characterization 14

1.3.1. X-ray Photoelectron Spectroscopy 15

1.3.2. Time-of-Flight Secondary Ion Mass Spectrometry 16

1.3.3. Spectroscopic Ellipsometry 18

1.3.4. Contact Angle Goniometry 21

1.3.5. Atomic Force Microscopy 22

1.3.6. Other Techniques 24

1.4. Overview of Dissertation 24

1.5. References 27

Chapter 2: Thiol-ene-thiol Photofunctionalization of Thiolated Monolayers with Polybutadiene and Functional Thiols, Including Thiolated DNA 37

2.1. Abstract 37

2.2. Introduction 38

2.3. Experimental Section 42

2.3.1. Materials 42

2.3.2. Preparation of Gold Substrates 44

2.3.3. Note on Gold Substrates 44

2.3.4. Preparation of SAMs 45

2.3.5. PBd Attachment to HDT/Au and ODT/Au Monolayers by Thiol-Ene Chemistry 45

2.3.6. PBd Functionalization via Thiol-Ene Chemistry 46

2.3.7. Modification of SiO_2/Si with MPTMS 46

2.3.8. Thiol-ene Chemistry on Thiol-Terminated SiO_2/Si 47

2.3.9. Stability Studies 48

2.3.10. Surface Analytical Techniques 48

2.4. Results and Discussion 49

2.4.1. Preparation of SAMs and Attachment of PBd to SAMs 49

2.4.2. Modification of PBd/HDT/Au by Thiol-Ene Chemistry 53

2.4.3. Attachment of DNA-SH to PBd/MPTMS/SiO_2/Si 56

2.4.4. Stability Comparison of PDT/PBd/HDT/Au and PDT/Au 57

2.5. Conclusions 62

2.6. Acknowledgment 62

2.7. References 62

Chapter 3: Complex, Stable Molecular Assemblies Prepared by the Integration of Multiple Surface Reactions: Layer-by-Layer, Thiol-ene, Bioconjugate, and Silanization Chemistries .. 67

3.1. Abstract 67

3.2. Introduction 68

3.3. Experimental 72

3.3.1. Materials 72

3.3.2. Electrostatic Layer-by-Layer (LBL) Assembly of PAH and PAA 72

3.3.3. Thermal Cross-Linking 73

3.3.4. Conversion of Amines to Thiols 73

3.3.5. Thiol-ene Chemistry 74

3.3.6. APTES Deposition 75

3.3.7. Sample Characterization 75

3.4. Results and Discussion 75

3.4.1. LBL Assembly of Films of PAH and PAA 75

3.4.2. Stability of LBL PAH/PAA Assemblies to XPS Analysis 79

3.4.3. Thermal Cross-Linking of LBL Films of PAH and PAA 81

3.4.4. LBL Film Stability in Solvents and at Low and High pH 85

3.4.5. Thiol Termination of PAH-Terminated PAH/PAA LBL Assemblies 88

3.4.6. Analysis and Prevention of –SH Group Oxidation 91

3.4.7. Rinsing of Thiol Terminated Assemblies with Acetic Acid 94

3.4.8. Thiol-Ene Attachment of 1,2-Polybutadiene to –SH Terminated Assemblies 94

3.4.9. Thiol-ene Attachment of Perfluorodecanethiol to PBd Terminated Assemblies 96

3.4.10. Stability of Hydrophobic Assemblies, Including Prevention of Film Delamination by Substrate Silanization 99

3.4.11. Controlling Surface Wetting with Cross-Linking 100

3.5. Conclusion 100

3.6. References 101

Chapter 4: Fluorine Plasma Treatment of Bare and Nitrilotris(methylene) triphosphonic acid (NP) Protected Aluminum. An XPS and ToF-SIMS Study 106

4.1. Abstract 106

4.2. Introduction 107

4.3. Experimental 111

4.3.1. Samples 111

4.3.2. X-ray Photoelectron Spectroscopy 111

4.3.3. Time-of-flight Secondary Ion Mass Spectrometry (ToF-SIMS) 112

4.4. Results and Discussion 112

4.4.1. XPS of Surfaces Before and After NP Deposition and Before and After Fluorine Plasma Treatment 112

4.4.2. Effects of Rinsing 119

4.4.3. Heating of Plasma-Treated Samples in the Air and Under Vacuum 120

4.4.4. Evolution of the Samples with Aging 123

4.4.5. Comments on the ToF-SIMS Data, Including a PCA Analysis 125

4.5. Conclusions 135

4.6. References 136

Chapter 5: Metal-Assisted Secondary Ion Mass Spectrometry (MetA-SIMS) with Bismuth 140

5.1. Abstract 140

5.2. Introduction 141

5.3. Experimental 146

5.3.1. Materials 146

5.3.2. Sample Preparation 146

5.3.3. Time-of-flight Secondary Ion Mass Spectrometry (ToF-SIMS) 147

5.3.4. Spectroscopic Ellipsometry 147

5.4. Results and Discussion 148

5.4.1. Determination of Bi Film Thicknesses on the Silicon Substrate and on PDADMAC Layers 148

5.4.2. MetA-SIMS Signal Enhancements Provided by Bi 153

5.5. Acknowledgements 162

5.6. References 162

Chapter 6: Conclusions and Future Work 165

6.1. Conclusions 165

6.2. Future Recommendations 166

Appendix A: Regression of Experimental Electron Binding Energies with Matrix Algebra. Semiempirical Predictions of Bohr's Theory to Multielectron Atoms 169

A.1. Abstract 169

A.2. Introduction 169

A.3. Solving a Simple Problem with Matrix Algebra 171

A.4. Fitting a Series of Data Points to a Straight Line using Matrix Algebra 173

A.5. Extending this Procedure to a Polynomial 178

A.6. Comparing/Fitting the 1s Binding Energies of the Elements to Bohr's Theory, AZ^2, and $AZ^2 + BZ + C$ 179

A.7. References 183

Appendix B: Abbreviations 184

LIST OF SCHEMES

Scheme 1.1. X-ray photoelectron spectroscopy (XPS)..... 17

Scheme 1.2. Time-of-flight secondary ion mass spectrometry (ToF-SIMS)..... 17

Scheme 1.3. Spectroscopic ellipsometry 19

Scheme 1.4. Contact angle goniometry 23

Scheme 1.5. Atomic force microscopy 23

Scheme 2.1. Functionalization of (a) Au(111) by HDT and (b) Si(100) by MPTMS and subsequent thiol-ene additions of 1,2-PB and other thiolated moieties (e.g. octadecanethiol, 1H,1H,2H,2H-perfluoroalkanethiol, and DNA-SH)..... 43

LIST OF FIGURES

Figure 2.1. Positive ion mode ToF-SIMS spectrum (all spectra scaled to the m/z = 41 peak) of (a) PBd reference, (b) PBd/HDT/Au, and (c) ODT/Au 'reacted' with PBd. 52

Figure 2.2. C1s XP narrow scans of (a) PDDT/PBd/HDT/Au and (b) PBd/HDT/Au 'reacted' with PFO. 55

Figure 2.3. N1s XP narrow scans of (a) DNA-SH/PBd/MPTMS/Si and (b) PBd/MPTMS/Si reacted with DNA. 59

Figure 2.4. C1s XP narrow scans of (a) PDT/PBd/HDT/Au and (b) PDT/Au immediately after preparation and (c) PDT/PBd/HDT/Au and (d) PDT/Au after exposure to light and air for 2 weeks followed by rinsing with water. 61

Figure 3.1. Thicknesses and roughnesses of PAH/PAA LBL assemblies prepared at pH 5 on silicon substrates. The numbers on the x-axis represent the total number of adsorbed layers (PAH or PAA). The '+' and '–' symbols on the x-axis labels represent the nature of the final polyelectrolyte layer: cationic (+) or anionic (-). 77

Figure 3.2. Comparison of the thicknesses of PAH/PAA LBL assemblies prepared at pH 8 and pH 5 on silicon substrates. The numbers on the x-axis represent the total number of adsorbed layers (PAH or PAA). The '+' and '–' symbols on the x-axis labels represent the nature of the final polyelectrolyte layer: cationic (+) or anionic (-). 78

Figure 3.3. XPS N 1s narrow scans fitted with two 100% Gaussians of equal width from three identical analyses performed sequentially on the same spot on uncross-linked LBL samples. The peak positions of the '-NH_3^+' and 'Amide' signals were allowed to float in the fitting. The signals of these peaks were 402.8 eV and 401.1 eV, 402.9 eV and 401.1 eV, and 402.9 eV and 401.1 eV in Analyses 1, 2, and 3, respectively. 80

Figure 3.4. XPS N 1s narrow scans fitted with two 100% Gaussians of equal width for (a) an uncross-linked PAH/PAA LBL assembly, and (b, c, and d) PAH/PAA LBL assemblies cross-linked for 2 h at 150 °C, 200 °C, and 250 °C, respectively. The Gaussian at higher binding energy is assigned to ammonium (-$NH_3^{+)}$, and the Gaussian at lower binding energy to amide, -NH-C(O)-, nitrogen. The peak positions of the '-NH_3^+' and 'Amide' signals were allowed to float in the fitting. The signals of these peaks were (a) 401.2 and 399.3, (b) 400.8 and 399.2, (c) 401.4 and 399.6, and (d) 402.4 and 399.5. These spectra were reference to the C 1s peak, which is why their peak positions are lower than those in Figure 3.3, which were not referenced. 84

Figure 3.5. Stability of uncross-linked (triangles) and cross-linked (circles) LBL assemblies before and after sonication in water for 20 min, THF for 15 min, and ethanol for 20 min, and after exposure to aqueous buffers at pH 1.68, 10, and 13. 87

Figure 3.6. Thickness changes by ellipsometry (circles) and S 2s/N 1s ratios (triangles) for PAH-terminated PAH/PAA assemblies treated with Traut's reagent under different conditions, as indicated above. All LBL assemblies were uncross-linked, except as indicated above. All exposures were for 30 min. This XPS analysis was carried out only for the uncross-linked LBL assemblies reacted with 0.1 M Traut's reagent, as shown in this figure. 90

Figure 3.7. XPS S 2s narrow scans of thiol-terminated samples before and after 24 h and 48 h exposures to air and light. The S 2s peak is fitted with three 80:20 Gaussian:Lorentzian peaks of equal width. The peaks are designated as oxidized sulfur, thiol (-SH), or thiolate ($-S^-$). 93

Figure 3.8. XPS 2s narrow scans of –SH terminated assemblies before and after rinsing with dilute (0.1 M) acetic acid for varying amounts of time. 95

Figure 3.9. Ellipsometric thicknesses and water contact angles after reaction of –SH terminated cross-linked with 1,2-polybutadiene (PBd) under different experimental conditions. The data points marked with '*' are for –SH terminated uncross-linked assemblies reacted in air instead of inert atmosphere. 97

Figure 3.10. Ellipsometric thicknesses and water contact angles of PBd coated surfaces reacted with perfluorordecanethiol (PDT) under different experimental conditions. 98

Figure 4.1. Structure of nitrilotris(methylene)triphosphonic acid (NP). 109

Figure 4.2. (a) P/Al and N/Al, and (b) O/Al, F/Al, and C/Al XPS pear area ratios of bare aluminum (Al-0s), bare aluminum after 8 s of fluorine plasma treatment (Al-8s), aluminum coated with NP (NP-0s), and NP-coated aluminum after exposure to a fluorine plasma for 4s – 20 s before (solid symbols) and after (open synbols) rinsing with water. 114

Figure 4.3. (a) P 2p, (b) N 1s, (c) Al 2p, (d) O 1s, and (e) F 1s XPS narrow scans of bare aluminum (Al-0s), bare aluminum after 8 s of fluorine plasma treatment (Al-8s), aluminum coated with NP (NP-0s), and NP-coated aluminum after exposure to a fluorine plasma for 4s – 20 s before (solid lines) and after (dashed lines) rinsing with water. 116

Figure 4.4. Survey and Al 2p narrow scans of bare aluminum and NP-coated aluminum samples treated with fluorine plasma for 8 s followed by baking for 5 hours at 300 °C in air. 121

Figure 4.5. ToF-SIMS spectra of the 'Al-8s' sample without any heat treatment (top), after heating at 300 °C in vacuum (middle), and after heating at 300 °C in the air for 5 h (bottom). The '300 °C, 5 h, Vacuum' sample was immediately analyzed without breaking vacuum. 122

Figure 4.6. Evolution of XPS P/Al, N/Al, F/Al, O/Al, and C/Al ratios of uncoated and plasma treated samples over three weeks. 124

Figure 4.7. The PCA loadings for PC 1, which captured the variation due to the fluorine plasma. The variables are labeled with molecular formulae of the ion observed in the mass spectrum. Note

that, for example, ‘PO_3-‘should be read as ‘PO_3^-‘. Refer to Table 4.1 for greater clarification. Please note that these are tentative assignments that may be incorrect for variables 13 - 21, which are for the fluorinated peaks. 128

Figure 4.8. The PCA scores for PC 1, which captured the variation in the samples induced by the fluorine plasma. The sample dots are enclosed in color coded boxes for the same type of samples. Two sets of samples from the same batch were analyzed with a one week gap between their analyses. The sample names used here have four parts separated by hyphens: (1) NP and Al for NP coated and bare aluminum, respectively, (2) a number (0, 4. 8, 12, 16, and 20) corresponds to the plasma exposure time in seconds, (3) a second number: ‘1’ or ‘2’ indicates samples analyzed the first or a week after, respectively, and (4) a third number: ‘1’ or ‘2’ that refer to samples numbers for the same type of samples that were analyzed at the same time. 129

Figure 4.9. The PCA loadings and scores for PC 2, which captured the variation in the NP layer. The variables are labeled with the molecular formulae of the ion observed in the mass spectrum. Note, for example, that ‘PO_3-‘should be read as ‘PO_3^-‘. Refer to Table 4.1 for additional clarification. Please note that these are tentative assignments that may be incorrect for variables 13 - 21, which are for the fluorinated peaks. 131

Figure 4.10. The PCA loadings and scores for PC 2, which captured the variation due to the NP layer. The sample dots are enclosed in color-coded boxes for the same type of samples. Two sets of samples from the same batch were analyzed at one week gap. The sample names used here have four parts separated by hyphens: (1) NP and Al for NP coated and bare aluminum, respectively, (2) a number (0, 4. 8, 12, 16, and 20) corresponds to the plasma exposure time in seconds, (3) a second number: ‘1’ or ‘2’ indicates samples analyzed the first or a week after, respectively, and (4) a third number: ‘1’ or ‘2’ that refer to samples numbers for the same type of samples that were analyzed at the same time. 132

Figure 4.11. The PCA loadings and scores for PC 3, which captured the variation among the samples induced by the fluorine plasma. The variables are labeled with the molecular formulae of the ion observed in the mass spectrum. Note, for example, that ‘PO_3-‘ should be read as ‘PO_3^-‘. Refer to Table 4.1 for additional clarification. Please note that these are tentative assignments that may be incorrect for variables 13 - 21, which are for the fluorinated peaks. 133

Figure 4.12. The PCA loadings and scores for PC 3, which captured the variation among the samples induced by the fluorine plasma. The sample dots are enclosed in color coded boxes for same type of samples. Two sets of samples from the same batch were analyzed at one week gap. 134

Figure 5.1. Structure of polydiallyldimethylammonium chloride (PDADMAC)..... 145

Figure 5.2. SE models used to determine the optical properties/thicknesses of (a) the thick oxide silicon/silica substrate, (b) a PDADMAC layer on the thick oxide silicon/silica substrate, (c) a Bi

layer on the thick oxide silicon/silica substrate, and (d) a Bi layer on a PDADMAC film on the thick oxide silicon/silica substrate. 149

Figure 5.3. Results of SE uniqueness testing on thick oxide silicon/silica substrates coated with Bi or PDADMAC and Bi. 154

Figure 5.4. ToF-SIMS signals assigned to $C_{23}H_{29}N_2^+$ (m/z 333) (left column) and $C_{18}H_{35}N_2^+$ (m/z 279) (right column) for (a) Si(100) spin coated with PDADMAC and 6 nm of Bi, (b) Si(100) spin coated with PDADMAC, (c) bare Si(100), and (d) Si(100) coated with 6 nm of Bi. 157

Figure 5.5. (a) MetA-SIMS enhancement factors in the range of ca. 10 – 100 for various ions from a PDADMAC sample coated with different thicknesses of bismuth, (b) MetA-SIMS enhancement factors in the range of ca. 100 – 1600 for various ions from a PDADMAC sample coated with different thicknesses of bismuth, and (c) Plot of MetA-SIMS enhancement factors vs. ion m/z value. 159

Figure 5.6. The evolution of positive ion mode ToF-SIMS signals (see Table 1) with time for PDADMAC polymer while the flood gun is (a) off, (b) on. The evolution of positive ion mode meta-SIMS signals (see Table 1) with time for PDADMAC polymer coated with 6 nm of bismuth layer while the flood gun is (c) off, (d) on. 161

Figure A.1. Graph of the points: (0, 0.1), (0.9, 1.1), (2.2, 1.9), (3.0, 2.7), and (4.1, 4.2), and the linear fit to them. 174

Figure A.2. Binding energies of the 1s electrons in the elements with Z = 1 to 92. The black dotted line represents the $-13.6Z^2/n^2$ (n = 1 for the 1s electrons) predictions from Bohr's theory. The dashed line represents a one-parameter Z^2 model, and the solid red line represents a three-parameter Z^2 model. 180

Figure A.3. Binding energies (open circles) of the $2p_{1/2}$ electrons in the elements with Z = 10 to 92. The dotted line represents the $-13.6Z^2/n^2$ (n = 2 for the $2p1_{/2}$ electrons) predictions from Bohr's theory. The dashed line represents a one-parameter Z^2 model, and the solid red line represents a three-parameter Z^2 model. 182

LIST OF TABLES

Table 2.1. Characterization of 1,6-hexanedithiol/gold (HDT/Au) and octadecanethiol/gold (ODT/Au) monolayers by spectroscopic ellipsometry and advancing water contact angles before (left) and after (right) reaction with polybutadiene (PBd). 51

Table 2.2. Characterization of PBd/HDT/Au monolayers by spectroscopic ellipsometry and advancing water contact angles before (left) and after (right) reaction with 1H,1H,2H,2H-perfluorododecanethiol (PDDT) and perfluorooctane (PFO), respectively. 54

Table 2.3. Ellipsometric thicknesses and advancing water contact angles of 3-mercaptopropyltrimethoxysilane (MPTMS) thin films on Si, PBd-terminated MPTMS/Si surfaces, and PBd/MPTMS/Si surfaces after exposure to DNA-SH and DNA. 'Si' indicates silicon surfaces terminated with native oxide. 58

Table 3.1. Initial and final ellipsometric thicknesses and XPS O 1s/N 1s ratios for PAH/PAA LBL films before and after thermal treatment. Times and temperatures were chosen to conform to a star-shaped experimental design. Three replicates were performed in the center of the design (at 200 °C and 2 h). The average O1s/N 1s ratio before cross-linking was 1.97, and the standard deviation and relative standard deviation for this set of data were 0.10 and 5.00%, respectively. 82

Table 3.2. Ellipsometric thicknesses of LBL assemblies before and after thermal cross-linking at 250° C for at least for 2 h. 86

Table 4.1. Peaks from the negative ion spectra selected for a principal components analysis (PCA) of the ToF-SIMS data. 127

Table 5.1. Thicknesses of bismuth layer measured by quartz crystal microbalance and spectroscopic ellipsometry. 152

Table 5.2. Ions from PDADMAC that showed significant signal enhancement in Bi MetA-SIMS with possible molecular assignments. 156

Chapter 1: Introduction to Surface Modification and Characterization

1.1. Introduction

Nature is flooded with complex molecular structures and assemblies at different length scales that are consistently carrying out complicated tasks in an autonomous manner. These provide tremendous motivation and inspiration to the scientific enterprise. However, reproducing many of these phenomena in the laboratory is still a daunting task, even for skilled scientists. DNA and proteins are especially inspirational. Both types of biomacromolecules contain significant amounts of the abundant, low atomic mass elements carbon (C), oxygen (O), and nitrogen (N). DNA consists of long chains of nucleic acid that can fold following specific H-bonding interactions to code genetic information and direct the production of specific proteins. Proteins are arguably more complex and even more interesting. They are polymeric chains of roughly twenty amino acids that fold into complex three-dimensional structures that ultimately carry out specific tasks – many proteins are essentially molecular scale machines with a vast array of functions. For example, as enzymes they may catalyze chemical reactions that would otherwise be extremely difficult to carry out in the rather mild, aqueous environments of cells. It is absolutely fascinating that Nature has the ability to drive so much complicated chemistry using only sunlight and a relatively small handful of elements without any continued intelligent intervention. Everything appears to self-assemble and self-improvise to continue survival. We, humans, are one of the best products of Nature. Compared to the capabilities of Nature, chemistry as we know it is still in its infancy.

All of this is not to imply that we, humans, have not reached significant milestones. We have discovered electricity and magnetism, quantum mechanics, and have progressed remarkably in making semiconductor devices. We manufacture complex devices like cellphones, computers, air conditioners, cars, airplanes, etc., that we use daily. We have engineered sophisticated scientific instruments that include scanning electron microscopes, mass spectrometers, X-ray spectrometers, etc. These devices are quite unique in nature. Although our innovations might be relatively small compared to what Nature has achieved in billions of years of evolution, our advances definitely bear some significance and novelty. We have progressed remarkably in the field of health sciences, where many diseases are entirely curable, and we are still working to find cures for scourges like cancer and AIDS. Computers have proved to be remarkable tools to speed our research in every area of science. The size of devices continues to shrink, thanks to great achievements in microfabrication that include photolithography, thin film deposition, etc. Of course the motivation behind making smaller devices is that, in general, they require less power, allow more functionality in the same space, are made from fewer raw materials, and are more economical. Indeed, to some degree we are already starting to work at molecular and atomic scales. For example, we have imaging techniques that enable us to see single atoms e.g. transmission electron microscopes. But, in terms of manipulating matter at the atomic level, we still have long way to go. That is, in spite of where we stand in the current era of miniaturization, we are merely entering the realm of molecular scale devices. Perhaps the main motivation behind the creation of devices at the molecular scale, in addition to what has been mentioned, is that they promise possibilities and solutions to problems that are beyond our imagination, as suggested and demonstrated by Nature itself.

Clearly a disadvantage of working in the molecular regime is that our top-down manufacturing approaches, like photolithography, become less and less applicable as we approach atomic/molecular length scales due to the diffraction limit of light. Nevertheless, our huge advantage now is that we can adopt or mimic many amazing phenomena directly from Nature, provided we can understand them, to self-assemble functional molecular devices for our use. For instance, we might be able to create a molecular device that can capture sunlight with substantially higher efficiency than is possible now, converting it into electricity, i.e., a man-made photosynthetic machine. Indeed, the sun illuminates the earth with more than enough photons to meet all our energy needs but we do not have technology to adequately capture this energy. Or, we could create enzymes to better convert cellulose into combustible fuel and other enzymes to convert emitted CO_2 back into carbon and oxygen at rates comparable to fuel consumption. But before we can realize any or all of these possibilities that the molecular regime has to offer, we need to understand the principles that govern atomic length scales with the same level of understanding and precision as we know the laws of motion that allow us to send a rocket into space. In this context, surface science offers an important platform to prepare, interact, and physically and chemically understand complex molecular functional devices on surfaces. Some of the complex molecular devices that might be constructed and understood with the apparatus of surface science include biosensors, solar cells, nanoscale electronic circuits, catalysts, nanobatteries, and molecules for transporting electrons in molecules, etc. There are two equally important aspects of surface science: surface chemistry and surface characterization. In this dissertation I explore a series of surface chemistries and surface characterization tools to make and analyze complex molecular assemblies. I firmly believe that this work, along with that of many other scientists, will bring mankind closer to its goal of imitation and even improvement of Nature.

1.2. Surface Chemistry

Surface chemistry often deals with the attachment of chemical moieties to solid surfaces, where this is often achieved via various coupling chemistries. The solid surface or substrate that is typically used for this purpose can be planar or particulate. Essentially any solid material can be coated. These may include metals (e.g., Au, Ag, Cu, Pt), alloys, semiconductors (e.g., Si, Ge, GaAs), oxides (e.g., SiO_2, indium tin oxide (ITO), CuO_2), plastics, and polymers (e.g., polycarbonate, polyethylene, polymethylmethacrylate). Of the thousands of good examples of surface chemistry in the literature, here are two that show some practical applicability to photovoltaics and immunosensing. Yamada et al. modified ITO with porphyrin-fullerene dyads to create a molecular level photovoltaic device.[1] Liu et al. demonstrated label free immunobiosensing with biotin on functionalized glassy carbon electrodes so that they could detect antibodies.[2] The attachment of porphyrin – fullerene dyads or biotin to a surface transformed a molecular signal into an amperometric one that could be more easily interpreted.[1-2] Such an integration of molecular scale devices with semiconductor technology/electronics demands in-depth knowledge of surface chemistry. Ultimately, this ability should give us precise control that will include precise positioning of adsorbates, a high degree of stability, reversibility (if it is required), and the desired functionality. The following is an overview of some well-known surface chemistry methods that can be employed to construct complex molecular structures on surfaces.

1.2.1. Self-Assembled Monolayers

Self-assembled monolayers (SAMs) can be defined as one molecule thick, continuous layers of a chemical species that spontaneously form on a surface when it is immersed in a solution of an adsorbate or comes in contact with its vapors. Sometimes additional treatments like thermal

curing or application of a voltage bias are required for these depositions. The most common precursors and surfaces in this category are organosilane monolayers on hydroxylated surfaces, thiol monolayers on gold, phosphonate monolayers on oxide surfaces, aryl diazonium salt derived layers, alkenes and alkynes on hydrogen-terminated silicon, and layer-by-layer electrostatic assemblies. The choice of self-assembly method depends significantly on the nature of the substrate.

1.2.1.1. Organosilane Chemistry

In 1980, Sagiv et al. first demonstrated covalent attachment of chlorosilane and alkoxysilanes to an oxidized substrate.[3] Since that time, this chemistry has found numerous practical and theoretical applications due to its broad applicability on many types of hydroxylated surfaces – silicon oxide, alumina, zinc oxide, iron oxide, polyvinyl alcohol, oxidized polyethylene, etc.[4-7] Silane deposition generally gives quite dense layers, but reproducibility in monolayer formation can be a challenging task when dealing with trichloro- and trialkoxysilanes due to cross-linking (polymerization) between silane molecules.[8-9] Nevertheless, it has been widely employed e.g., to make reversed phase stationary phases in chromatography, for coating glass.[10-11] The attachment of silane molecules to surfaces proceeds through the reaction of alkoxy- or halogen-groups on the silanes with surface hydroxyl groups.[12] In some cases, prior activation of the surface to increase the number of reactive surface hydroxyl groups on it is necessary.[13] In general all of the hydroxyl groups on a surface do not undergo silanization. The monolayer coverage may be obtained by lateral cross-linking of silane molecules to form long, polymeric chains or networks, and only 10 – 20 % of the concatenated/networked silanes need to form covalent linkages to the surface.[7] A considerable amount of research has been done on organosilane monolayers, which

has included the study of optimum aqueous/non-aqueous deposition conditions, curing temperatures, and orientation of SAM molecules.[14-16]

1.2.1.2. Thiol Monolayers on Gold

Organic molecules containing sulfur atoms in the form of thiol or sulfide moieties, e.g., alkanethiol, alkanedithiol, arenethiol, arenedithiol, dialkyldisulfides, and dialkylsulfides form self-assembled monolayers (SAMs) on a variety of pure metallic surfaces that are free from any native metal oxide layer, which may include Au, Ag, Ni, Pt, Fe, Pd, Cu, etc.[17-21] Thiol SAMs on Au gained special importance because of their ease of preparation, i.e., unlike most other metals Au does not form a stable oxide layer. In 1983, Nuzzo and Allara first demonstrated the affinity of thiol groups for gold vis-à-vis SAMs.[22] The structure of a typical thiol molecule/adsorbate can be subdivided into three parts, (a) a thiol or sulfide head group that interacts with the Au substrate (~50 kcal/mol),[23] (b) a hydrocarbon component (aromatic or aliphatic) that allows weak van der Waals interactions between adsorbates,[23] and (c) a terminal functional group that is chosen to impart a desired surface property, e.g., hydrophilicity or hydrophobicity, or used to further attach other molecules, biomolecules, and polymers of interest to the Au substrate. The exact nature of the Au-S interaction is still debatable; it is believed that upon adsorption the thiol loses its hydrogen to form thiolate species that tether to gold.[24] However, the chemisorption of intact thiols has also been reported.[25-26] Investigations based on density functional theory revealed that while disulfides chemisorb preferentially by thiolate formation, both thiolates and intact thiols can co-exist on a gold surface, where the SAMs were prepared using alkanethiol solutions.[27] In addition, plenty of controversial experimental and theoretical data have been reported in relation to a strong reconstruction of the gold surface during the formation of thiol SAMs.[28] In practice, it is found

that monolayer coverage is achieved in the first few minutes of immersion of a gold substrate in a solution of thiolated molecules. The initial SAM is quite disordered and the thiols are primarily in a lying down phase. However, if the substrate is immersed for hours, van der Waals interactions among any hydrocarbon chains on the adsorbates drives the reorganization of the SAMs into a standing-up phase of densely packed, well organized monolayers.[23, 29-30] The reorganization of SAMs from a lying down phase to standing up phase involves replacement of solvent molecules on the Au surface by thiols and the stretching up of hydrocarbon chains into a trans conformation. In this regard, terminal groups that might have significant affinity for the Au substrate, e.g., in dithiols, can hinder the development of crystalline SAMs or may require longer hydrocarbon chains to enhance the van der Waals interactions to achieve a standing up phase.[31]

The orientation of thiol molecules in well-ordered SAMs is described in terms of three angles with respect to the substrate: (a) the tilt angle, i.e., the angle between the axis of the hydrocarbon chain of the thiol molecule and the surface normal, (b) the twist angle, i.e., the angle of rotation of the hydrocarbon chain with respect to its axis, and (c) the precession angle, i.e., the angle between the projection of the tilt plane, which contains the surface normal and the molecular axis of the thiol molecule, and the substrate plane.[32-33] The typical value of the tilt angle is 30-35°.[25] The most stable lattice structures for thiol SAMs on Au (111) are $\sqrt{3}\ X\ \sqrt{3}\ R\ 30°$ and its C (4 X 2) superlattice.[34-35] The determination of the precise location where sulfur binds to a gold surface is still a subject of investigation. According to the latest gold adatom model, the gold surface undergoes significant reorganization at its interface with a thiol SAM.[36-37] In spite of our incomplete understanding of the Au-SAM interface, the well-known ability of thiol molecules to form dense crystalline SAMs on gold surface is extremely valuable as these surfaces can be consistently modified with high functional density using mild experimental conditions.[38] However,

this system has its limitations. For example, the thiol groups in SAMs are prone to oxidation.[39] Once the thiol group oxidizes, the Au-S bond strength drops substantially, which may lead to detachment of the adsorbate.[40-41] The packing density of SAMs, which depends greatly on the physical shape of the adsorbate, can contribute to their stability. In general, alkanethiols create more organized molecular assemblies than aromatic thiols – the alkanethiols pack quite well in a fully stretched, all-trans configuration. Nevertheless, in spite of their limitations, thiol SAMs serve as a valuable tool for numerous applications e.g., in biosensors for functionalizing gold electrodes with biomolecules in a consistent and facile manner, in microfabrication as resist layers using photooxidation and thiol-exchange reactions, for preventing aggregation of gold nano-architectures, for functionalization of medical devices like gold stents.[42-44]

1.2.1.3. Organophosphonic Acid SAMs

Phosphonic acids possess strong affinity for hydroxylated metal oxide surfaces e.g., zirconia,[45] titania,[46] alumina,[47-48] silica,[49-50] indium tin oxide.[51] Coatings of alkylphosphonic acids have been in use since the early 1970s as corrosion inhibitors of aluminum surfaces and as adhesion promotion layers.[47-48] Solid state NMR and vibrational spectroscopy studies show that phosphonic acid can directly react with hydroxylated surfaces to form strong P-O-X linkages where X can be Al, Si, Zr, Ti, etc.[52] Alkylphosphonic acids have advantages over silanes in that they are not prone to form multilayers by lateral cross-linking,[52-53] do not react with water,[54] and each phosphonate group can form two or three linkages with the substrate, which yields increased stability.[55] Hanson et al. and Raman et al. demonstrated multiple (two and three) linkages of organophosphonates to silica and steel surfaces, respectively.[55-56] Yee et al. functionalized iron oxide nanoparticles with alkylphosphonic acid SAMs and demonstrated higher thermal stability than alkylsulphonic acid

SAMs on iron oxide nanoparticles.[57] Marcinko et al. compared the hydrolytic stability of alkylphosphonic SAMs to alkyltrichlorosilane on titania and zirconia surfaces. Alkylphosphonic acid SAMs demonstrated higher stability at varied pH conditions (from 1-10).[58] In another study, amino acid modified phosphonate SAMs demonstrated greater stability at physiological pH in comparison to organosilane SAMs on Ti-6Al-4V alloys.[59] In comparison to organosilane SAMs, organophosphonic acid SAMs are less studied, but they are gaining attention due to their ease of preparation, handling, and stability.

1.2.2. Layer-by-Layer Deposition

The layer-by-layer (LBL) deposition process is also a self-assembling method, but it is not restricted to monolayer formation. Rather it allows the creation of multilayer structures. In LBL assembly, alternating layers of polymers, nanoparticles, molecules, or biomolecules that possess affinity for each other are deposited. The interaction between successive layers can be covalent,[60-62] electrostatic, H-bonding,[63-64] metal-ligand,[65-66] and pi-pi[67] in nature. The natural tendency of biological moieties to explicitly bind with their counterpart has also been exploited for creating LBL assemblies.[68-69] The most prevalent among them are the LBL assemblies based on electrostatic interactions. In fact, the first LBL assembly ever prepared was based on electrostatic interactions only.[70-71] Such assemblies are prepared by immersing substrates in solutions of cationic and anionic polyelectrolytes in an alternating fashion. For instance, a silicon wafer with a native SiO_2 layer is inherently negatively charged due to its silanol groups. When it is immersed in a solution of a cationic polyelectrolyte (e.g., polyallylamine hydrochloride, poly(diallyldimethylammonium chloride, polyethyleneimine), the cationic polyelectrolyte adheres to the substrate through electrostatic interactions. The interesting feature of this system is that once

the surface is covered with a cationic species, no additional material of the same charge will adsorb due to electrostatic repulsion. For example, if a substrate is covered by a polycation, the top surface will possess a positive charge that will prevent further adsorption of cationic species due to repulsion of like charges. This property of charge reversal incorporates a self-limiting feature to LBL depositions.[72] Now, once a surface has a positive charge, it can be immersed in a solution of an anionic polyelectrolyte (e.g., polyacrylic acid, polystyrene sulfonate, polyvinyl sulfonate) to deposit another layer in a similar self-limiting manner.[72-75] The electrostatic LBL deposition process has been successfully applied for applications that include light emitting diodes and non-linear optical optics, with materials that include biomaterials (e.g., DNA, proteins, sugars), nanoparticles, and even viruses.[63, 76-86] A significant amount of research has been performed to understand the LBL process, and it has been found that deposition conditions greatly influence the quality of final assemblies. For an instance, slight variations in the pH of the polyelectrolyte solution, rinsing and drying between each deposition step, the chemical nature and charge density of interacting chains, the presence of salt, and the temperature during the deposition can lead to remarkable variations in film roughnesses, porosities, layer thickness, and stability.[87-90] Thermodynamic studies have shown that the process of polyelectrolyte association is entropy driven and accordingly depends on the release of water of hydration and counterions.[91-92] The preparation of LBL assemblies is very simple because they only require simple, inexpensive equipment like beakers and tweezers. In addition, this process can be easily automated and coupled with spin coating and spray technologies to reduce the preparation time without compromising film quality.[93-98] The LBL process generally yields conformal layers, and due to its self-limiting nature the layer growth can be controlled at the monolayer level. The ease of preparation, molecular level control, and diversity of molecular materials that can be incorporated into these

multilayer structures render huge potential to LBL assemblies for numerous applications e.g., electro- and photo-chromic devices,[99] photovoltaics,[100] fuel cells,[101] field effect transistors,[102] photoluminescence,[103] superhydrophobic, superhydrophillic surfaces.[104-105]

1.2.3. Thiol-Ene Click Chemistry

Thiol-ene chemistry involves the hydrothiolation of carbon-carbon double bond (C=C). The thiol-ene reaction has been well known for over a century for preparing polymeric networks.[106-107] The application of the thiol-ene reaction was generally abandoned in the early 1970s due to a yellow discoloration on the surface of materials where thiol-ene polymer coatings had been employed for protection against wear. Interest in thiol-ene chemistry was renewed in late 1990s and continues to grow today as it has been recently realized that it possesses various attributes of a 'click' chemistry. A 'click' chemistry is one that can be carried out with high quantitative yields and with minimal undesirable byproducts under mild experimental conditions.[108] Depending on the experimental conditions, a thiol-ene reaction can proceed either as (1) a radical mediated chain reaction path,[109] or (2) a base catalyzed nucleophilic addition of an activated 'ene' functionality.[110-111] In the radical mediated mechanism, the S-H bond on a thiol functionality undergoes homolytic cleavage to generate thiyl radicals (R-S•). The thiyl radical initiates the thiol-ene reaction by adding on to C=C in an anti-Markovnikov fashion resulting in a carbon-centered radical. At this point, the reaction propagates in a chain reaction as the carbon-centered radical fetches a hydrogen atom from a new thiol molecule to generate another thiyl radical that can undergo the same fate. The termination of this thiol-ene reaction occurs by the coupling of two radical moieties.

In the case of the base catalyzed mechanism, a weak base, e.g., triethylamine (NEt_3), deprotonates a thiol group to form a thiolate species that can attack an activated C=C moiety. The

activation of the C=C group can be achieved by decreasing its electron density, e.g., by attaching it to an electron withdrawing (e.g., an ester, amide, cyano) group.[112] The radical mediated thiol-ene reaction offers more flexibility than the base catalyzed reaction as it does not require activation of the 'ene' functionality. The generation of the thiyl radical can be achieved by homolysis of the S-H bond by application of heat or UV light, with or without a thermal or photo initiator. A considerable amount of research has gone into understanding the effects of the molecular structures of thiols and alkenes,[113-114] the presence or absence of a variety of initiators, and the presence of oxygen on the kinetics of the thiol-ene reaction. In general, a terminal 'ene' was found to be more reactive than its substituted counterparts.[113] It was observed that the reactivity of the 'ene' reduces with decreasing electron density on the C=C group with the exception of norbornene, which shows high reactivity due to the relief of ring strain upon reaction.[113, 115] Methacrylate, styrene, and conjugated dienes are also exceptions in that they show slow thiol-ene kinetics due to higher stability of their carbon-centered radicals, which abstract H from thiol molecules in a less aggressive manner.[115] The thiol-ene reaction is also reversible in nature leading to isomerization of 'enes' from cis to trans, which can affect the net yield of thiol-ene reactions. With regards to the relationship between the molecular structure and reactivity of thiols, alkyl thiols are less reactive than thio propionate esters or thio glycolate esters. A variety of commercial molecules are available that possess multiple 'ene' or thiol functionalities to create polymeric networks with desired properties. It has also been shown that the thiol-ene reaction can be achieved without initiators at comparatively lower reaction rates.[116] An interesting and useful feature of thiol-ene chemistry is that it can be effectively carried out without being inhibited by oxygen in the reaction solvent.[117] The polymer networks prepared through thiol-ene chemistry possess excellent oxidative and thermal stability because of their thio-ether linkages.

1.2.4. Miscellaneous Chemistries

In addition to the above-mentioned self-assembled systems, other useful chemistries exist that have found application in surface science. For instance, the functionalization of hydrogen-terminated silicon with alkenes and alkynes, first reported by Linford et al.,[118] by application of radicals, heat, or UV light to create surface radicals that attack the double/triple bond of an alkene/alkyne.[118-120] This surface chemistry gained interest because of the robustness of the C-Si bond and also because it was on silicon, a substrate that is central to modern technology. Another system that has gained a great deal of attention is aryl SAMs derived from aryl diazonium salts.[121] The aryl diazonium salt can be electrochemically reduced to form molecular nitrogen and an aryl radical that covalently attaches itself to substrate atoms. This dissociation of diazonium salts can be carried out in aqueous or non-aqueous solvents with or without an applied bias. Compared to thiol SAMs on Au, aryl diazonium salt derived SAMs are extremely robust and can be prepared on a wide variety of substrates – various metals[122] (e.g., Au, Pt, Zn, Pt, Pd, Ni, Cu, Co), carbon nanotubes, other allotropes of carbon,[123-124] and ITO[125]. In general, the deposition conditions must be optimized vis-à-vis salt concentration, applied bias, and reaction time to avoid formation of multilayer polyphenylene structure. Aryl moieties can be protected/designed to limit multilayer formation. In general, –COOH and $–NH_2$ terminated aryl monolayers are most often prepared as they can be rather easily modified if desired.

1.2.5. Coupling Chemistries

In order to immobilize molecules to surfaces to create functional molecular devices, e.g., antibodies in biosensor applications or charge transferring molecules for solar cells, it is necessary to obtain appropriate functionality so that they can interact with the surface to form a bond. For

example, according to the previously described methods, the molecules might be functionalized with SiOR, SiCl, phosphonic acid, etc. groups for anchoring to oxide surfaces, e.g., metal oxides including silicon dioxide, or with diazonium or thiol groups to tether them to metal substrates. A variety of coupling chemistries can be employed to achieve this aim as presented in a review article by Samanta et al.[126] Carbodiimide chemistry[127] is effective in the coupling of carboxylic acid and amine functionalities to form amide bonds. The amide bond appears to be among Nature's favorites and is, of course, ubiquitous in proteins. This amine-carboxylic acid coupling is usually achieved by activation of the carboxylic groups with carbodiimide reagents, followed by nucleophilic attack by the amine. Commonly used carbodiimide reagents are N-[3-(dimethylamino)propyl]-N'-ethylcarbodiimide and N,N'-dicyclohexylcarbodiimide. These reactions have very high yields. Sometimes, N-hydroxysuccinimide is added to these reactions to prevent the formation of unwanted byproducts.[128] Maleimide chemistry can be used for coupling thiols. For example, *N*-succinimidyl 6-maleimidohexanoate possesses a maleimide residue on one end and an *N*-hydroxysuccinimidyl ester group at its other end. These groups react with thiol and amine groups, respectively. Thus, a thiol- or amine-terminated surface can be functionalized with biomolecules containing amine or thiol groups, respectively.

1.3. Surface Characterization

The other important aspect of surface science is surface characterization. Surface modification is usually a multistep process that involves the coupling of biomolecules, polymers, and other molecules of interest to surfaces. These molecules of interest may either be synthesized/modified using conventional solution-based organic chemistry, or a multistep modification procedure can be carried out sequentially on a substrate, which may start with the

initial modification of the surface with a self-assembled monolayer followed by coupling chemistries to bind molecules of interest. In either case it is extremely important to confirm that the intended reactions have occurred as desired on one's surface. A broad range of surface analytical techniques are available to monitor the formation of complex molecular assemblies at each step. These techniques, as discussed below, give information about the chemical and physical properties of the resulting thin films.

1.3.1. X-ray Photoelectron Spectroscopy

X-ray photoelectron spectroscopy (XPS)[129] is a surface sensitive analytical technique in which a sample surface is illuminated with X-rays that eject core electrons from the atoms present near the sample surface (see Scheme 1). To a good first approximation, when an X-ray is absorbed, a fraction of its energy is 'spent' overcoming the nuclear attractive force, and rest of the energy appears as the kinetic energy of the electron leaving the sample surface. The kinetic energy of an ejected electron is measured by an electron spectrometer, and this kinetic energy is subtracted from the original energy of the X-rays to determine the binding energy of ejected electrons. A small correction to this calculation is also made, which involves the spectrometer work function. An XPS spectrum is obtained by plotting the number (counts) of the photoelectrons vs. their binding energies. XPS is a quantitative technique that provides the elemental compositions of the upper ca. 10 nm of surfaces. Electrons originating at depths below ca. 10 nm are unable to leave the sample surface and/or undergo inelastic scattering process before escaping. These phenomena impart surface sensitivity to this technique. In addition to elemental composition, the changes in the peak shapes and positions in XPS spectra provide valuable information about the chemical environments of the elements present in samples. XPS is generally quite non-destructive, although

sample damage does occur, particularly with heavier Z substrates (due to high flux of photoelectrons ejected from the substrate) and/or non-monochromatic sources.

1.3.2. Time-of-Flight Secondary Ion Mass Spectrometry

Time-of-flight secondary ion mass spectrometry (ToF-SIMS)[130] is also a surface sensitive technique that provides chemical information about the upper ca. 2 nm of sample surfaces. In ToF-SIMS (see Scheme 2), the sample is irradiated with short pulses of fast moving primary ions that on impact sputter material off of the sample surface in the form of ions and neutral species. The ions sputtered from a surface in this manner are accelerated under high voltage through a time-of-flight tube (equipped with reflectron), detected, and then registered as a mass spectrum. ToF-SIMS may be performed in either positive or negative ion mode. ToF-SIMS is somewhat destructive in nature. Accordingly, the primary ion dose is typically kept below ca. 10^{13} ions/cm^2, which means that only ca. < 1% of the sample surface is probed (assuming a sample density of ~10^{15} atoms/cm^2). Working within this static limit ensures that the primary ions have a low chance of hitting a damaged (previously probed) spot on a surface. A variety of primary ion sources are available, including Ga^+, In^+, Ar^+, SF_6^+, C_{60}^+, Bi_n^+, and Au_n^+. Unlike XPS, ToF-SIMS is not quantitative in nature because the ionization efficiency of a sample is strongly influenced by its chemistry. This phenomenon is known as the matrix effect of the technique. Ion yields also depend on the nature of the primary ions, where polyatomic primary ions give higher ionization efficiencies, i.e., more intense SIMS signals. In comparison to XPS, ToF-SIMS is more surface sensitive (depth of information is ca. 2 nm) and it often shows much lower limits of detection.

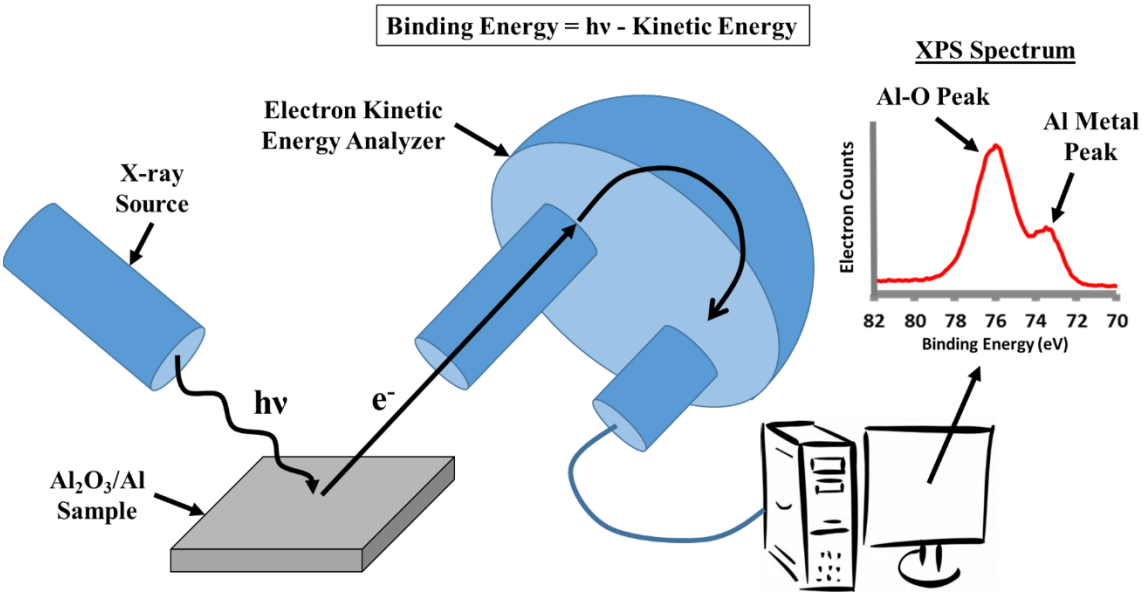

Scheme 1.1. X-ray photoelectron spectroscopy (XPS)

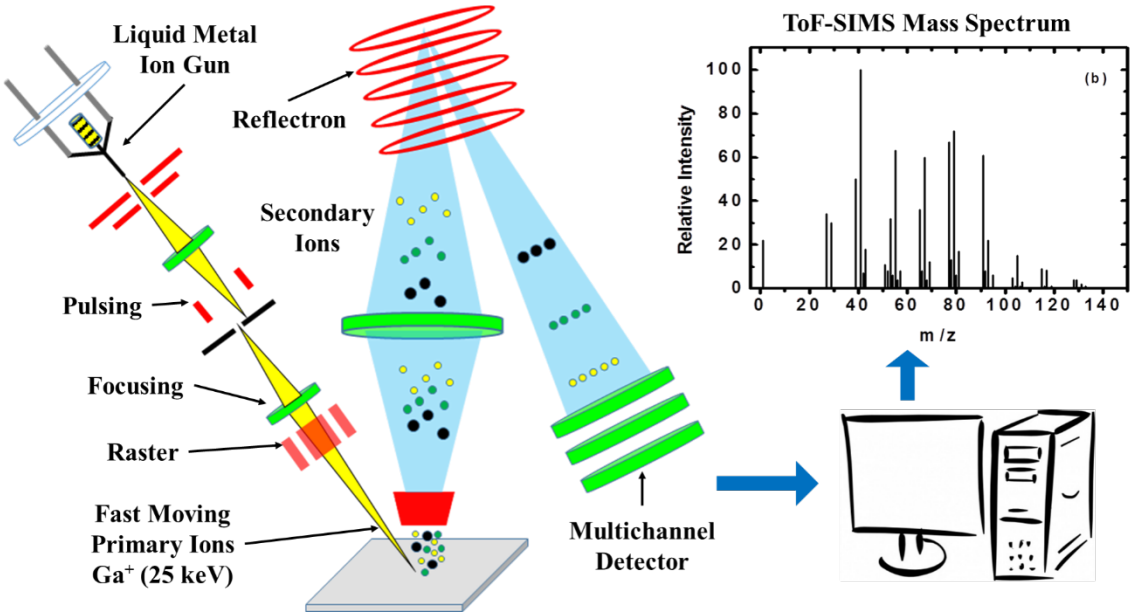

Scheme 1.2. Time-of-flight secondary ion mass spectrometry (ToF-SIMS)

1.3.3. Spectroscopic Ellipsometry

Ellipsometry[131-133] is non-destructive technique that can be applied quickly, often in real time, and at atmospheric pressure, to accurately and precisely determine thicknesses and optical constants of thin films. These days, ellipsometry is usually performed spectroscopically with a range of wavelengths, which remarkably increases the power of the technique. Ellipsometry can also be used to probe surface/material conductivity and crystallinity. Spectroscopic ellipsometry (SE) is based on the measurement of the change in the polarization state of plane polarized light after its specular reflection from a sample surface. Light with another defined polarization state, e.g., circular or elliptical, can also be employed. The p- and s- oriented components of plane polarized light interact differently with surfaces and materials, so the polarization state of the reflected light is often elliptical (see Scheme 3). The change in polarization is captured in the form of the amplitude ratio, $\tan(\psi)$, and phase difference, Δ, between the p- and s- components after reflection from the sample surface. Ellipsometry can also be performed in transmission mode where the change in polarization is measure after the light is made to pass through the sample.

Reflection ellipsometry is the more common approach. Spectroscopic ellipsometry is not a direct technique in the sense that the measured response, i.e., $\tan(\psi)$ and Δ, cannot generally be viewed as the thickness, optical constants, or other properties of interest of a thin film. Rather, a model consisting of different layers in a particular sequence is created that is meant to describe the actual multilayer structure of a sample. The interaction of each layer with incident light depends on its optical constants, thickness, roughness, or presence of voids. In order to find optical constants, film thicknesses, and/or other properties of thin films, the optical response is simulated using an iterative regression procedure where values of the optical constants, thicknesses, and other properties are typically varied to generate $\tan(\psi)_{gen}$ and Δ_{gen} that best fit the experimental values:

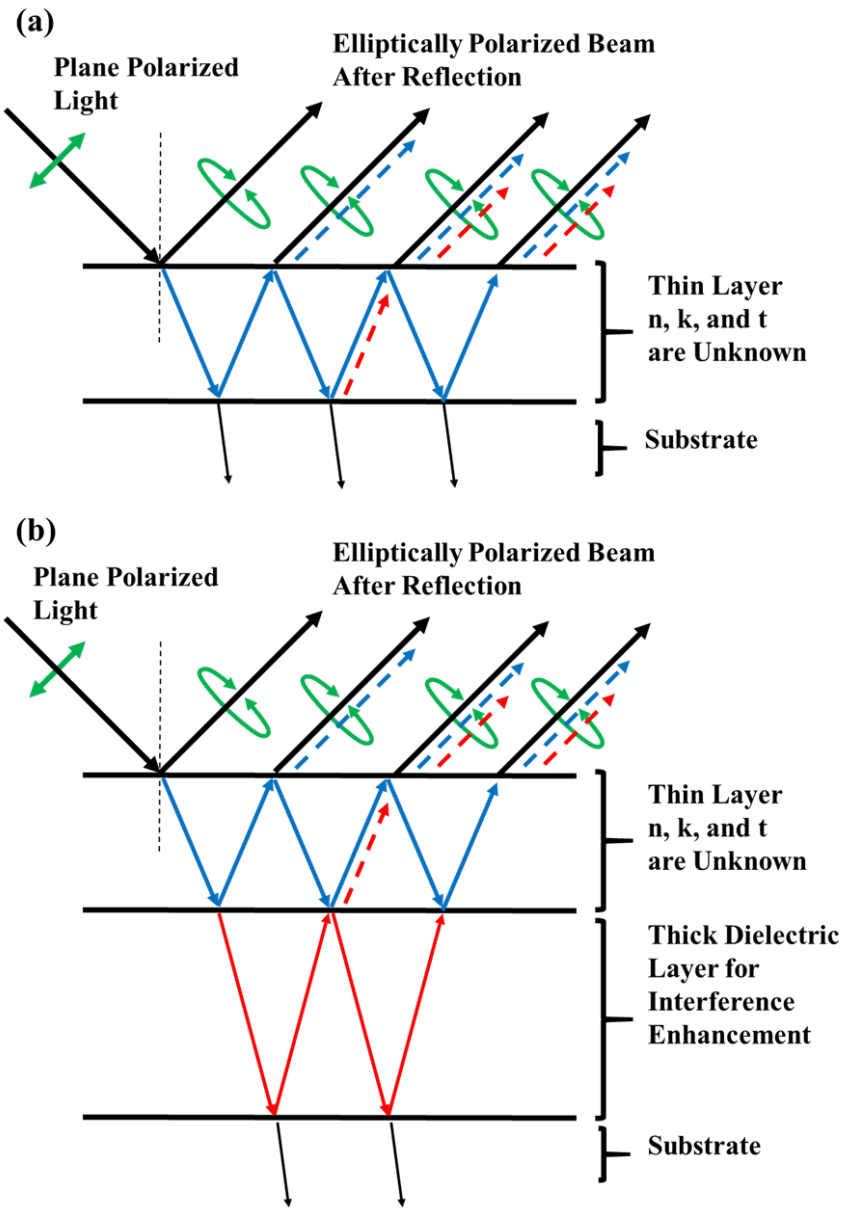

Scheme 1.3. Spectroscopic ellipsometry

$\tan(\psi)_{exp}$ and Δ_{exp}. The goodness of fit between experimental and generated ψ and Δ values can be quantified by calculating the mean square error (MSE) as follows.

$$MSE = \sqrt{\frac{1}{2N-M}\sum_{i=1}^{N}\left[\left(\frac{\psi_i^{mod}-\psi_i^{exp}}{\sigma_{\psi,i}^{exp}}\right)^2+\left(\frac{\Delta_i^{mod}-\Delta_i^{exp}}{\sigma_{\Delta,i}^{exp}}\right)^2\right]} = \sqrt{\frac{1}{2N-M}\chi^2}$$

Where, 'N' is the number of ψ and Δ pairs, 'M' is the number of fit parameters, and $\sigma_{\psi\ or\ \Delta,i}^{exp}$ are the experimental standard deviations of the measurements. If too many parameters are included in a model, correlation may exist between them that can severely limit the model's predictive abilities. Accordingly, uniqueness tests[30] are often performed in which one of the fit parameters is fixed at a series of values over a desired range, and the remaining parameters are adjusted to obtain the best possible fit, i.e., the lowest MSE. The resulting MSE values are plotted against the values of a parameter that is systematically varied. If the resulting plot is a horizontal line, or if it shows a great deal of shallowness, the model shows correlation and is unreliable. In contrast, a good uniqueness plot will show MSE values rising around the optimal value of the parameter that is varied.

Correlation between optical constants and thicknesses is not generally a problem for transparent films, and even semi-transparent films if they have a transparent region, but it is generally an issue for thin absorbing metal layers. Fortunately, methods like interference enhancement exist that make it possible to accurately measure both optical constants and thicknesses of thin metal (absorbing) layers by spectroscopic ellipsometry. In interference enhanced SE, a thick layer (~200-500 nm) of dielectric material is introduced between the substrate and the layer of interest. This additional layer leads to enhancement in the interaction of the light

with the substrate and film, which assists the regression process to allow it to reach a more reliable solution, even for a fairly large number of fit parameters. A uniqueness test of the resulting fit can verify the absence of correlation between these parameters.

1.3.4. Contact Angle Goniometry

Contact angle goniometry is a simple benchtop technique that measures the wettability of surfaces.[134-135] When a droplet of liquid is placed on a surface (see Scheme 4), its shape is determined by the Young equation as follows.

$$\lambda_{SG} = \lambda_{SL} + \lambda_{LG} cos\Theta$$

Here, $\lambda_{SG}, \lambda_{SL}, \lambda_{LG}$ are the solid-gas, solid-liquid, and liquid-gas interfacial energies, respectively. 'Θ' is the contact angle of the probe droplet at the liquid-gas and solid-liquid interface. Contact angle goniometry is an extremely sensitive technique that gives information about the hydrophobic/hydrophilic nature of surfaces. It can be performed with water or hydrophobic probe liquids like hexadecane. The contact angles can be measured with a static sessile drop method or a dynamic method. In the sessile drop method, a drop of known volume is placed on a sample surface and its contact angle is measured. In the dynamic method, advancing and receding contact angles are measured. To measure an advancing contact angle, a droplet of a probe liquid is placed on a surface, after which more liquid is slowly added to the drop until it just moves over the surface. The contact angle of the droplet at this point is its advancing contact angle. Receding contact angles are measured in a similar fashion. However, in this case, liquid is gradually removed from the drop until its contact area with the surface just decreases. The contact angle of the droplet at this point is its receding contact angle. The difference between the advancing and receding contact angles is

known as the contact angle hysteresis and it is a measure of the pinning properties of the liquid drop on the surface. Rougher surfaces tend to show higher hysteresis.

1.3.5. Atomic Force Microscopy

Atomic force microscopy[136-137] is a scanning probe technique in which, in one mode, an oscillating cantilever bearing a sharp tip is rastered in close proximity to a sample surface (see Scheme 5). The amplitude of cantilever oscillations decreases as it approaches the sample surface and vice versa. A constant distance is maintained between the vibrating AFM tip and the sample surface by continuously maintaining the amplitude of cantilever oscillations using a feedback control system at a point set by the user. The feedback system consists of a laser beam that bounces off the back of cantilever to hit a position sensitive detector. When a scanning AFM tip encounters an elevated (or depressed) feature on the sample surface it experiences more (or less) pronounced atomic forces leading to decrease (or increase) in the amplitude of cantilever oscillations. Any changes in the amplitude of cantilever oscillations are detected and corrected by changing the height of the sample with respect to the AFM tip using a piezoelectric crystal. The registered values of x, y (during the rastering), and changes in z (to maintain constant amplitude of cantilever oscillations) are used to construct a three dimensional image of the sample surface. In comparison to scanning electron microscopy, AFM offers various advantages. For instance, it does not require a vacuum for its operation, insulated samples can be analyzed without needing carbon or a metal coating, it gives 3D images of sample topography, and it can be applied to biological samples even under water.

$$\boxed{\lambda_{SG} = \lambda_{SL} + \lambda_{LG}cos\theta}$$

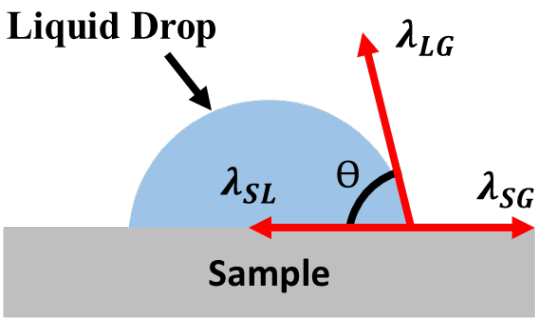

Scheme 1.4. Contact angle goniometry

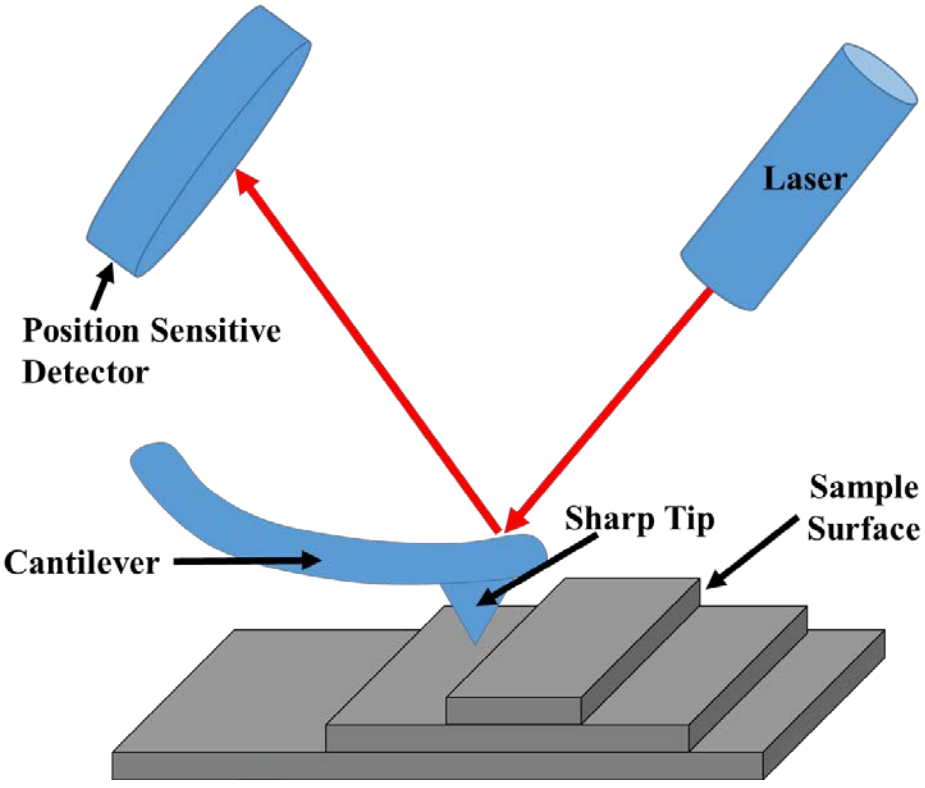

Scheme 1.5. Atomic force microscopy

1.3.6. Other Techniques

In addition to the above described analytical techniques, a large number of additional analytical instruments exist that are regularly used in surface characterization.[138] These include scanning electron microscopy (for surface imaging),[139] attenuated total internal reflectance Fourier transform infrared spectroscopy (for understanding the functional groups at surfaces),[140] Rutherford back scattering,[138] nuclear reaction analysis,[138] etc. Each technique has its own advantages and disadvantages and provides some unique information. A thorough characterization of a surface or material usually involves application of more than one technique. In my research work, I have applied XPS, ToF-SIMS, spectroscopic ellipsometry, water contact goniometry, and on occasion atomic force microscopy.

1.4. Overview of Dissertation

In this dissertation I explore combinations of several different surface chemistries to assemble complex molecular structures with desired properties on planar gold and silicon dioxide substrates. In Chapter 1, an introduction is given to various surface chemistry reactions and surface characterization techniques. In Chapter 2, I demonstrate an alternative surface modification strategy for gold surfaces that shows increased chemical stability. That is, although self-assembled monolayers (SAMs) of thiols on gold are the most common surface functionalization of gold, the resulting assemblies lack stability. In particular, the sulfur in adsorbed thiols is prone to oxidation, which leads to detachment of thiols from gold surfaces, or at least substantial weakening of the Au-S bond, in only a few days after their formation. The short-term stability of thiol SAMs might not be a problem for the purposes of some laboratory research, but industrial applications or applications that demand long-term stability of functionalized gold surfaces require more robust chemical methods. In order to improve the stability of functionalized gold surfaces, I used the self-

assembly of dithiols, instead of monothiols, in combination with thiol-ene click chemistry with 1,2-polybutadiene to create a gold surface terminated with vinyl groups that can be functionalized with single stranded DNA using thiol-ene chemistry. I demonstrated that the final assembly was chemically more stable than thiol SAMs alone. The thiol-ene chemistry is a photochemistry that bears many of the hallmarks of a 'click' chemistry. Clearly this chemistry is also compatible with surface photopatterning.

In Chapter 3, I worked on creating a complex, stable molecular assembly with tunable hydrophobic properties. In this work, I used a combination of layer-by-layer (LBL) polyelectrolyte deposition with polyallylamine hydrochloride (PAH) and polyacrylic acid (PAA), and thiol-ene chemistry with 1,2-polybutadiene and perfluorinated alkanes. The motivation behind using layer-by-layer deposition was that (1) it gives conformal layers, (2) the deposition process can be easily automated, and (3) the thickness of each layer can be well controlled down to nanometer length scales. In addition, alternating layers of PAH and PAA can be thermally cross-linked to form amide bonds to give a chemically robust structure. The amine groups on amine terminated LBL assemblies were converted into thiol groups by Traut's reagent in order to carry out thiol-ene chemistry. I demonstrated that the final assembly was strongly hydrophobic with interesting water droplet pinning properties that could be tuned by the extent of heat treatment of the assemblies. The final structure also demonstrated long term chemically stability, while retaining its hydrophobic properties, at pH 1.68. It was also mechanically stable to wiping with ethanol swabs. Detailed surface characterization with suitable methods was carried out during the preparation of the functional assemblies described in the second and third chapters of this dissertation.

The next chapter focuses on applications of surface characterization to solving real world problems when little is known about the materials in question. That is, in Chapter 4, X-ray

photoelectron spectroscopy (XPS) is used in combination with time-of-flight secondary ion mass spectrometry (ToF-SIMS) to understand the cause of corrosion observed on aluminum based optical devices. In particular, XPS demonstrates that a mild exposure to the down-stream products of a fluorine plasma (as a part of microfabrication of these devices) significantly damages an organic corrosion protection layer of nitrilotris(methylene)-triphosphonate on aluminum, and converts the aluminum oxide beneath the coating to an aluminum oxyfluoride that is more susceptible to corrosion. This aluminum oxyfluoride could be converted back to the more stable aluminum oxide by heating it in the air. Principal components analysis was applied to interpret the complex ToF-SIMS data.

The work in this dissertation is consistent with the fact that surface characterization plays a critical role in understanding thin films and surfaces. Ideally, we would require these techniques to be highly sensitive and accurate. Sometimes, unconventional sample preparation methods are required to enhance the sensitivity and reliability of these analytical methods. In Chapter 5, I explore enhancement of ToF-SIMS signals by depositing ultrathin layers of bismuth onto a sample surface. The sample was a piece of a silicon wafer spin coated with polydiallyldimethylammonium chloride (MW 100,000-200,000). This general method is called metal-assisted SIMS (MetA-SIMS). However, this is the first study that has been carried out with bismuth, which has a very high Z value and in many regards is ideally suited for this purpose. An enhancement in the SIMS signal by a factor of 10 – 1600 was observed. Here, I also point out a source of error in the meta-SIMS work presented in the literature. That is, in the meta-SIMS work reported to date, scientists have used a quartz crystal microbalance for monitoring the thicknesses of the metal films they have deposited, while assuming that the sticking coefficients of the sample and the quartz crystal are the same, i.e., unity. Although, in various research articles it has been pointed out that this

assumption could be inaccurate, no effort has been made to find a solution. Here, for the first time, I incorporate interference enhanced spectroscopic ellipsometry to correctly measure the thicknesses of metal layers directly on sample surfaces. I demonstrate the correctness of the ellipsometric methods using atomic force microscopy and show, for example, that while bismuth sticks to polydiallyldimethylammonium chloride, it does not stick to 1,2-polybutadiene, which was additionally confirmed by ToF-SIMS. Finally I demonstrate that sample preparation can play a huge role in imparting meaningful information to the final data obtained by this approach.

In Chapter 6, a holistic summary of the entire work is given and recommendations are made as to future work that can be pursued. In Appendix A, I present a short tutorial that demonstrates the immense importance of the atomic model first put forward by Niels Bohr about a century ago. Here I relate Bohr's predictions to electron binding energies. Electron binding energies are of central importance in X-ray photoelectron spectroscopy, which is one of the most applied techniques in my work. In this tutorial, I also describe multiple linear regression as an important data fitting tool. In Appendix B, a list of abbreviations used in this dissertation is presented.

1.5. References

1. Yamada, H.; Imahori, H.; Nishimura, Y.; Yamazaki, I.; Ahn, T. K.; Kim, S. K.; Kim, D.; Fukuzumi, S. *J. Am. Chem. Soc.* **2003,** *125* (30), 9129-9139.
2. Liu, G.; Paddon-Row, M. N.; Gooding, J. J. *Chem. Commun.* **2008,** (33), 3870-3872.
3. Sagiv, J. *J. Am. Chem. Soc.* **1980,** *102* (1), 92-98.
4. Le Grange, J.; Markham, J.; Kurkjian, C. *Langmuir* **1993,** *9* (7), 1749-1753.
5. Lee, I.; Wool, R. P. *Thin Solid Films* **2000,** *379* (1), 94-100.

6. Pursch, M.; Vanderhart, D. L.; Sander, L. C.; Gu, X.; Nguyen, T.; Wise, S. A.; Gajewski, D. A. *J. Am. Chem. Soc.* **2000,** *122* (29), 6997-7011.

7. Gooding, J. J.; Ciampi, S. *Chem. Soc. Rev.* **2011,** *40* (5), 2704-2718.

8. Tian, R.; Seitz, O.; Li, M.; Hu, W.; Chabal, Y. J.; Gao, J. *Langmuir* **2010,** *26* (7), 4563-4566.

9. Silberzan, P.; Leger, L.; Ausserre, D.; Benattar, J. *Langmuir* **1991,** *7* (8), 1647-1651.

10. Der Voort, P. V.; Vansant, E. *Relat. Technol.* **1996,** *19* (17-18), 2723-2752.

11. Metwalli, E.; Haines, D.; Becker, O.; Conzone, S.; Pantano, C. *J. Colloid Interface Sci.* **2006,** *298* (2), 825-831.

12. Brzoska, J.; Azouz, I. B.; Rondelez, F. *Langmuir* **1994,** *10* (11), 4367-4373.

13. Zhuravlev, L. T. *Langmuir* **1987,** *3* (3), 316-318.

14. Rozlosnik, N.; Gerstenberg, M. C.; Larsen, N. B. *Langmuir* **2003,** *19* (4), 1182-1188.

15. Wang, Y.; Lieberman, M. *Langmuir* **2003,** *19* (4), 1159-1167.

16. Pasternack, R. M.; Rivillon Amy, S.; Chabal, Y. J. *Langmuir* **2008,** *24* (22), 12963-12971.

17. Azzaroni, O.; Vela, M.; Fonticelli, M.; Benitez, G.; Carro, P.; Blum, B.; Salvarezza, R. *J. Phys. Chem. B* **2003,** *107* (48), 13446-13454.

18. Fonticelli, M.; Azzaroni, O.; Benitez, G.; Martins, M.; Carro, P.; Salvarezza, R. *J. Phys. Chem. B* **2004,** *108* (6), 1898-1905.

19. Bengió, S.; Fonticelli, M.; Benítez, G.; Creus, A. H.; Carro, P.; Ascolani, H.; Zampieri, G.; Blum, B.; Salvarezza, R. C. *J. Phys. Chem. B* **2005,** *109* (49), 23450-23460.

20. Williams, J. A.; Gorman, C. B. *J. Phys. Chem. C* **2007,** *111* (34), 12804-12810.

21. Pirlot, C.; Delhalle, J.; Pireaux, J.; Mekhalif, Z. *Surf. Coat. Technol.* **2001,** *138* (2), 166-172.

22. Nuzzo, R. G.; Allara, D. L.,. *J.Am.Chem.Soc.* **1983,** *105*, 4481-4483.

23. Ulman, A. *Chem. Rev.* **1996,** *96* (4), 1533-1554.

24. Kankate, L.; Turchanin, A.; Gölzhäuser, A. *Langmuir* **2009,** *25* (18), 10435-10438.

25. Nuzzo, R. G.; Zegarski, B. R.; Dubois, L. H. *J. Am. Chem. Soc.* **1987,** *109* (3), 733-740.

26. Hasan, M.; Bethell, D.; Brust, M. *J. Am. Chem. Soc.* **2002,** *124* (7), 1132-1133.

27. Andreoni, W.; Curioni, A.; Grönbeck, H. *Int. J. Quantum Chem.* **2000,** *80* (4-5), 598-608.

28. Maksymovych, P.; Voznyy, O.; Dougherty, D. B.; Sorescu, D. C.; Yates Jr, J. T. *Prog. Surf. Sci.* **2010,** *85* (5), 206-240.

29. Bain, C. D.; Troughton, E. B.; Tao, Y. T.; Evall, J.; Whitesides, G. M.; Nuzzo, R. G. *J. Am. Chem. Soc.* **1989,** *111* (1), 321-335.

30. Vericat, C.; Vela M, E.; Benitez, G.; Carro, P.; Salvarezza, R. C. *Chem. Soc. Rev.* **2010,** *39*, 1805-1834.

31. Millone, M. a. A. D.; Hamoudi, H.; Rodríguez, L.; Rubert, A.; Benítez, G. A.; Vela, M. a. E.; Salvarezza, R. C.; Gayone, J. E.; Sánchez, E. A.; Grizzi, O. *Langmuir* **2009,** *25* (22), 12945-12953.

32. Schreiber, F. *Prog. Surf. Sci.* **2000,** *65* (5), 151-257.

33. Delamarche, E.; Michel, B.; Biebuyck, H. A.; Gerber, C. *Adv. Mater.* **1996,** *8* (9), 719-729.

34. Fenter, P.; Eisenberger, P.; Liang, K. *Phys. Rev. Lett.* **1993,** *70* (16), 2447.

35. Widrig, C. A.; Alves, C. A.; Porter, M. D. *J. Am. Chem. Soc.* **1991,** *113* (8), 2805-2810.

36. Cossaro, A.; Mazzarello, R.; Rousseau, R.; Casalis, L.; Verdini, A.; Kohlmeyer, A.; Floreano, L.; Scandolo, S.; Morgante, A.; Klein, M. *Science* **2008,** *321* (5891), 943-946.

37. Mazzarello, R.; Cossaro, A.; Verdini, A.; Rousseau, R.; Casalis, L.; Danisman, M.; Floreano, L.; Scandolo, S.; Morgante, A.; Scoles, G. *Phys. Rev. Lett.* **2007,** *98* (1), 016102.

38. Chaki, N. K.; Vijayamohanan, K.. *Biosens. Bioelectron.* **2002,** *17* (1), 1-12.

39. Huang, J.; Hemminger, J. C. *J. Am. Chem. Soc.* **1993,** *115* (8), 3342-3343.

40. Willey, T. M.; Vance, A. L.; Van Buuren, T.; Bostedt, C.; Terminello, L.; Fadley, C. *Surf. Sci.* **2005,** *576* (1), 188-196.

41. English, R. D.; Van Stipdonk, M. J.; Sabapathy, R. C.; Crooks, R. M.; Schweikert, E. A. *Anal. Chem.* **2000,** *72* (24), 5973-5980.

42. Levicky, R.; Herne, T. M.; Tarlov, M. J.; Satija, S. K. *J. Am. Chem. Soc.* **1998,** *120* (38), 9787-9792.

43. Brust, M.; Walker, M.; Bethell, D.; Schiffrin, D. J.; Whyman, R. *J. Chem. Soc., Chem. Commun.* **1994,** (7), 801-802.

44. Van Bommel, K.; Friggeri, A.; Mateman, D.; Geurts, F. A.; Van Leerdam, K.; Verboom, W.; Van Veggel, F.; Reinhoudt, D. N. *Adv. Funct. Mater.* **2001,** *11* (2), 140-146.

45. Hevesy, G. v.; Kimura, K. *J. Am. Chem. Soc.* **1925,** *47* (10), 2540-2544.

46. Randon, J.; Blanc, P.; Paterson, R. *J. Membr. Sci.* **1995,** *98* (1), 119-129.

47. Germscheid, H. G.; Friedemann, W.; Geisler, R. ., Process for Treating Aluminum Surfaces. US Patent 3,900,370: 1975.

48. Ahearn, J.; Davis, G. *J. Adhesion* **1989,** *28* (2-3), 75-102.

49. Lukes, I.; Borbaruah, M.; Quin, L. D. *J. Am. Chem. Soc.* **1994,** *116* (5), 1737-1741.

50. Woodward, J. T.; Ulman, A.; Schwartz, D. K. *Langmuir* **1996,** *12* (15), 3626-3629.

51. Gardner, T. J.; Frisbie, C. D.; Wrighton, M. S. *J. Am. Chem. Soc.* **1995,** *117* (26), 6927-6933.

52. Gao, W.; Dickinson, L.; Grozinger, C.; Morin, F. G.; Reven, L. *Langmuir* **1996,** *12* (26), 6429-6435.

53. Zorn, G.; Gotman, I.; Gutmanas, E.; Adadi, R.; Salitra, G.; Sukenik, C. *Chem. Mater.* **2005,** *17* (16), 4218-4226.

54. McDowell, M.; Hill, I.; McDermott, J.; Bernasek, S.; Schwartz, J. *Appl. Phys. Lett.* **2006,** *88* (7), 073505.

55. Raman, A.; Dubey, M.; Gouzman, I.; Gawalt, E. S. *Langmuir* **2006,** *22* (15), 6469-6472.

56. Hanson, E. L.; Schwartz, J.; Nickel, B.; Koch, N.; Danisman, M. F. *J. Am. Chem. Soc.* **2003,** *125* (51), 16074-16080.

57. Yee, C.; Kataby, G.; Ulman, A.; Prozorov, T.; White, H.; King, A.; Rafailovich, M.; Sokolov, J.; Gedanken, A. *Langmuir* **1999,** *15* (21), 7111-7115.

58. Marcinko, S.; Fadeev, A. Y. *Langmuir* **2004,** *20* (6), 2270-2273.

59. Silverman, B. M.; Wieghaus, K. A.; Schwartz, J. *Langmuir* **2005,** *21* (1), 225-228.

60. Kohli, P.; Blanchard, G. *Langmuir* **2000,** *16* (10), 4655-4661.

61. Such, G. K.; Quinn, J. F.; Quinn, A.; Tjipto, E.; Caruso, F. *J. Am. Chem. Soc.* **2006,** *128* (29), 9318-9319.

62. Tian, Y.; He, Q.; Tao, C.; Li, J. *Langmuir* **2006,** *22* (1), 360-362.

63. Stockton, W.; Rubner, M. *Macromolecules* **1997,** *30* (9), 2717-2725.

64. Yang, S. Y.; Rubner, M. F. *J. Am. Chem. Soc.* **2002,** *124* (10), 2100-2101.

65. Altman, M.; Shukla, A. D.; Zubkov, T.; Evmenenko, G.; Dutta, P.; van der Boom, M. E. *J. Am. Chem. Soc.* **2006,** *128* (22), 7374-7382.

66. Wanunu, M.; Vaskevich, A.; Cohen, S. R.; Cohen, H.; Arad-Yellin, R.; Shanzer, A.; Rubinstein, I. *J. Am. Chem. Soc.* **2005,** *127* (50), 17877-17887.

67. Tang, T.; Qu, J.; Müllen, K.; Webber, S. E. *Langmuir* **2006,** *22* (1), 26-28.

68. Anzai, J.-i.; Kobayashi, Y. *Langmuir* **2000,** *16* (6), 2851-2856.

69. Kobayashi, Y.; Anzai, J. I. *J. Electroanal. Chem.* **2001,** *507* (1), 250-255.

70. Decher, G.; Hong, J.; Schmitt, J. *Thin Solid Films* **1992,** *210*, 831-835.

71. Lvov, Y.; Decher, G.; Moehwald, H. *Langmuir* **1993,** *9* (2), 481-486.

72. Berndt, P.; Kurihara, K.; Kunitake, T. *Langmuir* **1992,** *8* (10), 2486-2490.

73. Korneev, D.; Lvov, Y.; Decher, G.; Schmitt, J.; Yaradaikin, S. *Physica. B* **1995,** *213*, 954-956.

74. Hoogeveen, N. G.; Cohen Stuart, M. A.; Fleer, G. J.; Böhmer, M. R. *Langmuir* **1996,** *12* (15), 3675-3681.

75. Chen, W.; McCarthy, T. J. *Macromolecules* **1997,** *30* (1), 78-86.

76. Lvov, Y.; Yamada, S.; Kunitake, T. *Thin Solid Films* **1997,** *300* (1), 107-112.

77. Qi, Z.-m.; Honma, I.; Ichihara, M.; Zhou, H. *Adv. Funct. Mater.* **2006,** *16* (3), 377-386.

78. Shutava, T. G.; Kommireddy, D. S.; Lvov, Y. M. *J. Am. Chem. Soc.* **2006,** *128* (30), 9926-9934.

79. Ishibashi, A.; Yamaguchi, Y.; Murakami, H.; Nakashima, N. *Chem. Phys. Lett.* **2006,** *419* (4), 574-577.

80. Yamauchi, F.; Koyamatsu, Y.; Kato, K.; Iwata, H. *Biomaterials* **2006,** *27* (18), 3497-3504.

81. Luo, L.; Liu, J.; Wang, Z.; Yang, X.; Dong, S.; Wang, E. *Biophys. Chem.* **2001,** *94* (1), 11-22.

82. Voigt, A.; Lichtenfeld, H.; Sukhorukov, G. B.; Zastrow, H.; Donath, E.; Bäumler, H.; Möhwald, H. *Ind. Eng. Chem. Res.* **1999,** *38* (10), 4037-4043.

83. Qiu, X.; Leporatti, S.; Donath, E.; Möhwald, H. *Langmuir* **2001,** *17* (17), 5375-5380.

84. Tian, S.; Liu, J.; Zhu, T.; Knoll, W. *Chem. Mater.* **2004,** *16* (21), 4103-4108.

85. Salgueiriño-Maceira, V.; Correa-Duarte, M. A.; Spasova, M.; Liz-Marzán, L. M.; Farle, M. *Adv. Funct. Mater.* **2006,** *16* (4), 509-514.

86. Lvov, Y.; Haas, H.; Decher, G.; Moehwald, H.; Mikhailov, A.; Mtchedlishvily, B.; Morgunova, E.; Vainshtein, B. *Langmuir* **1994,** *10* (11), 4232-4236.

87. Lvov, Y.; Ariga, K.; Onda, M.; Ichinose, I.; Kunitake, T. *Colloids Surf., A* **1999,** *146* (1), 337-346.

88. Yoo, D.; Shiratori, S. S.; Rubner, M. F. *Macromolecules* **1998,** *31* (13), 4309-4318.

89. Shiratori, S. S.; Rubner, M. F. *Macromolecules* **2000,** *33* (11), 4213-4219.

90. Sukhishvili, S. A.; Kharlampieva, E.; Izumrudov, V. *Macromolecules* **2006,** *39* (26), 8873-8881.

91. Bucur, C. B.; Sui, Z.; Schlenoff, J. B. *J. Am. Chem. Soc.* **2006,** *128* (42), 13690-13691.

92. Bharadwaj, S.; Montazeri, R.; Haynie, D. T. *Langmuir* **2006,** *22* (14), 6093-6101.

93. Shiratori, S. S.; Ito, T.; Yamada, T. *Colloids Surf., A* **2002,** *198*, 415-423.

94. Yamada, M.; Shiratori, S. S. *Sens. Actuators, B* **2000,** *64* (1), 124-127.

95. Chiarelli, P. A.; Johal, M. S.; Holmes, D. J.; Casson, J. L.; Robinson, J. M.; Wang, H. L. *Langmuir* **2002,** *18* (1), 168-173.

96. Campbell, V. E.; Chiarelli, P. A.; Kaur, S.; Johal, M. S. *Chem. Mater.* **2005,** *17* (1), 186-190.

97. Schlenoff, J. B.; Dubas, S. T.; Farhat, T. *Langmuir* **2000,** *16* (26), 9968-9969.

98. Izquierdo, A.; Ono, S.; Voegel, J.-C.; Schaaf, P.; Decher, G. *Langmuir* **2005,** *21* (16), 7558-7567.

99. Liu, S.; Möhwald, H.; Volkmer, D.; Kurth, D. G. *Langmuir* **2006,** *22* (5), 1949-1951.

100. Mwaura, J. K.; Pinto, M. R.; Witker, D. *Langmuir* **2005,** *21* (22), 10119-10126.

101. Jiang, S. P.; Liu, Z.; Tian, Z. Q. *Adv. Mater.* **2006,** *18* (8), 1068-1072.

102. Cui, T.; Liu, Y.; Zhu, M. *Appl. Phys. Lett.* **2005,** *87* (18), 183105.

103. Yang, P.; Li, C.; Murase, N. *Langmuir* **2005,** *21* (19), 8913-8917.

104. Han, J. T.; Zheng, Y.; Cho, J. H.; Xu, X.; Cho, K. *J. Phys. Chem. B* **2005,** *109* (44), 20773-20778.

105. Lee, D.; Rubner, M. F.; Cohen, R. E. *Nano Lett.* **2006,** *6* (10), 2305-2312.

106. Posner, T. *Ber. Dtsh. Chem. Ges.* **1905**, 38 (1), 646-657.

107. Shin, J.; Matsushima, H.; Chan, J. W.; Hoyle, C. E. *Macromolecules* **2009,** *42* (9), 3294-3301.

108. Kolb, H. C.; Finn, M.; Sharpless, K. B. *Angew. Chem., Int. Ed.* **2001,** *40* (11), 2004-2021.

109. Hoyle, C. E.; Lee, T. Y.; Roper, T. *J. Polym. Sci., Part A: Polym. Chem.* **2004,** *42* (21), 5301-5338.

110. Chan, J. W.; Hoyle, C. E.; Lowe, A. B. *J. Am. Chem. Soc.* **2009,** *131* (16), 5751-5753.

111. Chan, J. W.; Yu, B.; Hoyle, C. E.; Lowe, A. B. *Chem. Commun.* **2008,** (40), 4959-4961.

112. Mather, B. D.; Viswanathan, K.; Miller, K. M.; Long, T. E. *Prog. Polym. Sci.* **2006,** *31* (5), 487-531.

113. Roper, T. M.; Guymon, C.; Jönsson, E.; Hoyle, C. *J. Polym. Sci., Part A: Polym. Chem.* **2004,** *42* (24), 6283-6298.

114. Cramer, N. B.; Bowman, C. N. *J. Polym. Sci., Part A: Polym. Chem.* **2001,** *39* (19), 3311-3319.

115. Morgan, C.; Magnotta, F.; Ketley, A. *J. Polym. Sci., Polym. Chem. Ed.* **1977,** *15* (3), 627-645.

116. Cramer, N. B.; Scott, J. P.; Bowman, C. N. *Macromolecules* **2002,** *35* (14), 5361-5365.

117. Gush, D.; Ketley, A. *Mod. Paint Coat.* **1978,** *11*, 68.

118. Linford, M. R.; Chidsey, C. E. D. *J. Am. Chem. Soc.* **1993,** *115*, 12631-12632.

119. Ciampi, S.; Harper, J. B.; Gooding, J. J. *Chem. Soc. Rev.* **2010,** *39* (6), 2158-2183.

120. Boukherroub, R. *Curr. Opin. Solid State Mater. Sci.* **2005,** *9* (1), 66-72.

121. Delamar, M.; Hitmi, R.; Pinson, J.; Saveant, J. M. *J. Am. Chem. Soc.* **1992,** *114* (14), 5883-5884.

122. Bernard, M.-C.; Chaussé, A.; Cabet-Deliry, E.; Chehimi, M. M.; Pinson, J.; Podvorica, F.; Vautrin-Ul, C. *Chem. Mater.* **2003,** *15* (18), 3450-3462.

123. Sinitskii, A.; Dimiev, A.; Corley, D. A.; Fursina, A. A.; Kosynkin, D. V.; Tour, J. M. *ACS Nano* **2010,** *4* (4), 1949-1954.

124. Allongue, P.; Henry de Villeneuve, C.; Cherouvrier, G.; Cortes, R.; Bernard, M.-C. *J. Electroanal. Chem.* **2003,** *550*, 161-174.

125. Maldonado, S.; Smith, T. J.; Williams, R. D.; Morin, S.; Barton, E.; Stevenson, K. J. *Langmuir* **2006,** *22* (6), 2884-2891.

126. Samanta, D.; Sarkar, A. *Chem. Soc. Rev.* **2011,** *40* (5), 2567-2592.

127. Sehgal, D.; Vijay, I. K. *Anal. Biochem.* **1994,** *218* (1), 87-91.

128. Staros, J. V.; Wright, R. W.; Swingle, D. M. *Anal. Biochem.* **1986,** *156* (1), 220-222.

129. Briggs, D.; Seah, M. P. Wiley: Chichester, 1990; Vol. 1.

130. Briggs, D.; Vickerman, J. C. IM: Chichester, 2001.

131. Tompkins, H. G.; McGahan, W. A. Wiley New York: 1999.

132. Fujiwara, H. John Wiley & Sons: 2007.

133. Hilfiker, J. N.; Singh, N.; Tiwald, T.; Convey, D.; Smith, S. M.; Baker, J. H.; Tompkins, H. G. *Thin Solid Films* **2008,** *516* (22), 7979-7989.

134. Cassie, A. *Discuss. Faraday Soc.* **1948**, 3, 11-16.

135. Good, R. J.; Girifalco, L. *J. Phys. Chem.* **1960**, 64 (5), 561-565.

136. Rugar, D.; Hansma, P. *Phys. today* **1990**, 43 (10), 23-30.

137. Meyer, E. *Prog. Surf. Sci.* **1992**, 41 (1), 3-49.

138. Bubert, H.; Rivière, J. C.; Arlinghaus, H. F.; Hutter, H.; Jenett, H.; Bauer, P.; Palmetshofer, L.; Fabry, L.; Pahlke, S.; Quentmeier, A. *Surface and Thin-Film Analysis.* Wiley Online Library: 2002.

139. Goldstein, J. I.; Newbury, D. E.; Echlin, P.; Joy, D. C.; Fiori, C.; Lifshin, E. *Scanning electron microscopy and X-ray microanalysis. A text for biologists, materials scientists, and geologists.* Plenum Publishing Corporation: 1981.

140. Potts, R.; Guzek, D.; Harris, R.; McKie, J. *Arch. Dermatol. Res.* **1985**, 277 (6), 489-495.

Chapter 2: Thiol-ene-thiol Photofunctionalization of Thiolated Monolayers with Polybutadiene and Functional Thiols, Including Thiolated DNA

2.1. Abstract

Self-assembly of organic thiols is the most common way to introduce functional groups onto gold surfaces. The gold-sulfur (Au-S) bond is moderately strong (~45 kcal/mole). However, it is prone to oxidation, which substantially weakens the Au-S interaction. In this work, we describe the creation of more robust molecular assemblies on gold. As a first step, a thiolated monolayer is prepared on gold with an α,ω-dithiol. Experiments are also reported for a mercaptosilane monolayer on silicon dioxide. An oligomer of polybutadiene (PBd) was then tethered to these surfaces using thiol-ene chemistry. Residual groups on the PBd were then reacted with thiols, including octadecanethiol (ODT), 1H,1H,2H,2H-perfluoroalkanethiol, and a thiol-terminated 25-mer of DNA. Little non-specific adsorption of a non-thiolated DNA oligomer was observed. Surface characterization was performed with X-ray photoelectron spectroscopy (XPS), contact angle goniometry, time-of-flight secondary ion mass spectrometry (ToF-SIMS), and spectroscopic ellipsometry. A thiol-gold monolayer and an analogous assembly of the same thiol tethered to gold through PBd on a dithiol monolayer were both exposed to air and light for two weeks and then

rinsed with water. The monolayer on gold was removed in this process while the thiol in the assembly appeared unaffected.

2.2. Introduction

Organic surface functionalization and modification play an important role in many fields, including biosensing, lubrication, electrochemistry, catalysis, nanotechnology, biomaterials, and biotechnology,[1, 2] where two of the persistent requirements for a good surface modification/functionalization are robustness in the chemistry and robustness in the final coating. One of the most studied and used surface modifications is that of self-assembled monolayers (SAMs) of thiols on gold.[3-7]

The ultimate utility of SAMs depends critically on their long-term stability, and a great deal of work has been done to understand the role of oxygen,[8] ozone, ultraviolet (UV) radiation,[9, 10] hydrocarbon chain length, end group properties,[11-13] substrate structure,[14] and reaction environment (air, water, and ethanol)[15, 16] on degradation of SAMs. For example, it is now well known that when thiol SAMs on gold are exposed to the ambient environment, oxidation of the sulfur head groups occurs, rendering the gold-sulfur (Au-S) bond very weak. Oxidized thiols in SAMs desorb upon simple aqueous rinsing, undergoing exchange reactions in fresh thiol solutions, even with shorter alkanethiols. Desorption and displacement of oxidized thiols in SAMs shows their decreased affinity for gold. The short-term durability of SAMs has made possible their extensive characterization, but significantly restricted their possible widespread technological application. In comparison to thiol SAMs on gold, silane SAMs on silicon oxide surface have demonstrated better thermal[17] and tribological stability.[18] SAMs on silicon[19] and scribed silicon[20, 21] in general are also more stable than SAMs on gold. Nevertheless, due to its unique optical and

chemical properties, gold[2] is widely used in nanotechnology, either in planar or nanoparticle form, as a substrate for SAMs.

Various attempts have been made, going back to the early 1990s, to evaluate and improve the stability of SAMs. For example, the effect of chemical structure on stability of a variety of aromatic/aliphatic SAMs using thermal[22-24] and/or electrochemical[25-29] desorption methods has been studied. In a few cases, the effects of aggressive solvents on SAM stability have been evaluated.[30] Remarkable improvements in the stability of SAMs were achieved by introducing additional, stronger intermolecular interactions, including covalent cross-linking and hydrogen bonding. Whitesides et al. achieved five times improvement in the thermal stability of 11-mercapto-undecanyl-1-boronic acid SAMs on gold by using the reversible cross-linking (via dehydration) of their terminal boronic acid groups.[24] The stabilities of SAMs containing a diacetylene group ($SH(CH_2)_{10}$-$(C{\equiv}C)_2$-$(CH_2)_{10}COOH$) were compared before and after photopolymerization at 254 nm. The resulting cross-linked SAMs were extremely stable when subjected to aggressive solvents, high temperatures (200 °C), and electrochemical desorption.[30] Also terphenyl methanethiol, benzyl mercaptan, and decanethiol SAMs were exposed to 245 nm UV radiation. Sulfur oxidation was not observed in the irradiated terphenyl methanethiol SAMs, as measured by X-ray photoelectron spectroscopy (XPS).[31] Intermolecular cross-linking of aromatic SAMs has also been achieved by low energy electron irradiation, although electron irradiation usually has a destructive effect on SAMs. (In the case of aromatic SAMs, radiation-induced cross-linking overpowers radiation induced desorption.) Zharnikov et al. fabricated stable cross-linked SAMs of [1,1';4',1"-terphenyl]-4,4''-dimethanethiol (TPDMT) and used them for depositing thin metal films of nickel.[32] The same group also showed that SAMs of perfluoroterphenyl-substituted alkanethiols can be cross-linked by low energy electron radiation

to improve their stability.[33] Electron irradiated, cross-linked SAMs of 1,1'-biphenyl-4-thiol (BPT) were prepared that were thermally stable up to 1000 K, where BPT SAMs that were not cross-linked were only stable up to 400 K.[23] Beyer et al. created stable chemical patterns by localized electron induced cross-linking of 4'-nitro-1,1'-biphenyl-4-thiol (NBPT) SAMs followed by exchange reactions over the rest of the uncross-linked NBPT with BPT. BPT was unable to displace cross-linked NBPT SAMs. The electron exposure also converted (reduced) the nitro groups on NBPT to amine groups.[34]

Improved SAM stability has been achieved by intermolecular hydrogen bonding, instead of covalent cross-linking.[22, 35, 36] In all the literature discussed above, a number of extremely stable SAMs were fabricated. However, synthesis of thiolated moieties with complex functionalities like diacetylene and di- or terphenyl groups for cross-linking is not an easy task. None of this cited research focused on developing a general method for introducing different functional groups onto their assemblies in a stable manner. In view of the potential technological importance of robust gold surface functionalization, the search for a more versatile strategy has become the goal of this work.

Thiols have been very useful in another field of chemistry, that of "thiol-ene" chemistry. Thiol-ene reactions carry many of the attributes of a click chemistry – they only require mild experimental conditions with readily available starting materials, show high yields, require small concentrations of benign catalysts, have rapid reaction rates, require essentially no clean up, and are insensitive to ambient oxygen and water. These exceptional qualities have made thiol-ene chemistry amenable to a variety of applications. Thiol-ene free radical addition can be initiated thermally as well as photochemically without addition of any catalyst. Thus, light-mediated thiol-ene radical reactions have the combined benefits of click chemistry and the advantages of a

photoinitiated process, which can be activated at specific times and locations. The ability to functionalize/pattern surfaces simply by exposure to light has made thiol-ene chemistry a popular surface modification reaction. In 2008, pioneering work by Waldmann and co-workers showed photoimmobilization of alkene-functionalized biotin and farnesylated proteins onto thiol-modified surfaces, offering a facile method for making protein microarrays.[37] Bertin and Schlaad functionalized thiol-terminated surfaces with allyl-α-D-glucopyranoside, perfluoro-1-decene, and 1,2-polybutadiene (PBd).[38] Thiol-ene chemistry was exploited as a robust, efficient and orthogonal reaction for fabrication of tunable polyethylene glycol- (PEG) and polysiloxane-based cross-linked materials for imprint lithography applications.[39] It was also used to transfer metallic patterns from one substrate to another[40] and to make photocurable stamps from a mixture of poly[(3-mercaptopropyl)-methylsiloxane] and triallyl cyanurate.[41] Recently, immobilization of a range of thiols including *N*-acetyl-L-cysteine, D,L-dithiothreitol, 3-mercaptopropionic acid, and tetraacetylgalactoside or galactoside-thiol conjugate on alkene-terminated SAMs was achieved by photochemical microcontact printing.[42] An alkene-terminated, striped, patterned surface obtained by Langmuir-Blodgett lithography was successfully functionalized with a fluorescent rhodamine thiol using thiol-ene chemistry.[43] Thiol-ene chemistry has been exploited to fabricate microarrays covalently attached to hydrogel substrates based on PEG[44] and for modification of planar polymer surfaces[45] as well as polymer microspheres,[46, 47] covalent layer-by-layer assembly of dithiols and dienes[48] and for the fabrication of polymer-coated surfaces by free radical polymerization.

In this paper we explore a method for making thiol-on-gold monolayers more resistant to the effects of oxidation. This process appears to involve robust chemistry and leads to more robust coatings. This chemistry begins with the formation of dithiol monolayers on gold (Scheme 2.1a), which are then modified with PBd via thiol-ene photochemistry.[38, 45, 48, 49] The attachment/cross-

linking of PBd to surface thiol groups appears to provide stability to the underlying SAM. In this process, only a fraction of the vinyl groups in the PBd appear to be used in its immobilization, allowing subsequent photochemical modification of residual carbon-carbon double bonds with other thiols (see Scheme 2.1). The resulting films appear to be more stable against air oxidation than comparable thiol-on-gold monolayers. Mercaptosilane monolayers on silicon wafer (SiO_2/Si) (Scheme 2.1b) could also be modified with thiolated DNA. Ultimately the presence of immobilized DNA oligomers on these surfaces may serve to anchor other DNA oligomers or DNA origami in a robust manner.[50] After each reaction, surfaces were analyzed by contact angle goniometry, optical ellipsometry, XPS and/or time-of-flight secondary ion mass spectrometry (ToF-SIMS).

2.3. Experimental Section

2.3.1. Materials

Gold pellets (99.999%, 1/8" Diameter × 1/8" Length) and chromium plated tungsten rods were obtained from the Kurt J. Lesker Co., Clairton, PA. Silicon wafers (SiO_2/Si) with (100) crystallographic orientation, were obtained from University Wafers, Boston, MA. 1,6-hexanedithiol (HDT) (≥ 97%), octadecanethiol (ODT) (98%), 1,2-polybutadiene (PBd) (approx. 62 mole % 1,2-addition; M_n = 2.8 kg/mol, M_w = 4.6 kg/mol, as determined by size exclusion chromatography), 1H,1H,2H,2H-perfluorododecanethiol (PDDT), 1H,1H,2H,2H-perfluorodecanethiol (PDT) (97%), perfluorooctane (PFO) (98%), and 3-mercaptopropyltrimethoxysilane (MPTMS) (95%) were obtained from Sigma-Aldrich, St. Louis, MO. Thiolated DNA (DNA-SH) 25-mer and an otherwise identical, non-thiolated DNA were obtained from Eurofins MWG Operon, Huntsville, AL; sequence: 5'-AACCCGCGAGGTCCCCGCCCTACGT-thiol-3'. The obtained DNA was stored in TE buffer

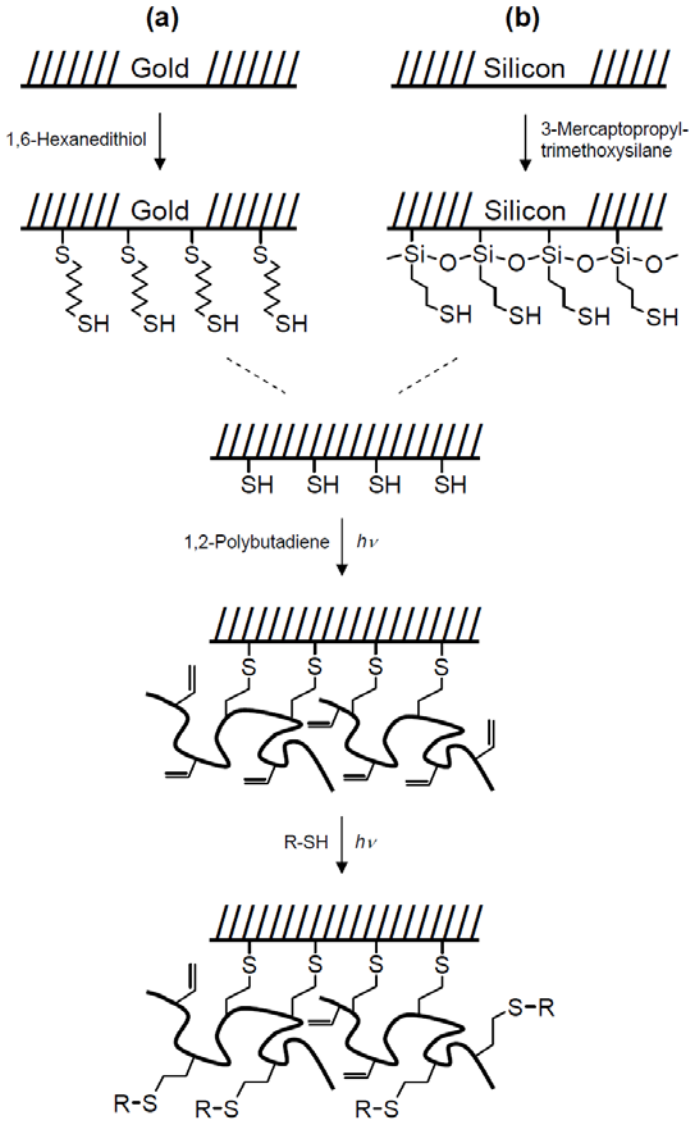

Scheme 2.1. Functionalization of (a) Au(111) by HDT and (b) Si(100) by MPTMS and subsequent thiol-ene additions of 1,2-PB and other thiolated moieties (e.g. octadecanethiol, 1H,1H,2H,2H-perfluoroalkanethiol, and DNA-SH).

(10 mM Tris, 1 mM EDTA, with pH 8-8.5). Ethanol-200 proof (EtOH), was obtained from Decon Labs Inc., King of Prussia, PA. Stabilized tetrahydrofuran (THF) was obtained from Mallinckrodt, Phillipsburg, NJ. All chemicals and materials were used as received.

2.3.2. Preparation of Gold Substrates

Without any prior cleaning, and in a clean room environment, new silicon wafers (4" diameter) were coated by thermal evaporation with an adhesion layer of 10–20 nm of chromium, followed by 200 nm of gold. Vacuum was not broken between depositions. The thicknesses of the Chromium and gold layers were determined with a quartz crystal thickness monitor in the chamber. Based on literature precedent, the gold is expected to have a substantial (111) texture.[51] The resulting gold coated silicon wafers were then broken into small pieces (ca. 1×1 cm^2), which are referred to herein as gold substrates or Au(111). For all experiments, the Au(111) was prepared fresh and used immediately.

2.3.3. Note on Gold Substrates

In our thermal evaporator, up to eighteen silicon wafers could be coated simultaneously. Hence, it would have been preferable to process eighteen wafers at a time and to then store them for future experiments. To test this possibility, ODT monolayers were prepared on fresh gold substrates, EtOH submerged gold substrates (freshly prepared gold substrates that had been stored under EtOH), and also on 'older' gold substrates, which had been stored for weeks in the air in the laboratory. Prior to monolayer deposition, the 'older' gold substrates were plasma cleaned or cleaned with piranha solution. ODT SAMs were also prepared on gold substrates that had been stored in a clean room. With the exception of the fresh Au(111), lower water contact angles and

ellipsometric thicknesses were observed on all other gold substrates. These results point to some sort of almost irreversible contamination and/or change to the high free energy gold surface during storage. Similar statements regarding gold's propensity to contaminate exist in the literature.[52-55] Therefore, fresh gold substrates were used in all of the experiments reported herein. The optical constants of the gold substrates were determined by spectroscopic ellipsometry prior to monolayer formation.

2.3.4. Preparation of SAMs

For the preparation of HDT SAMs, freshly prepared Au(111) was immersed in 10 mM solutions of HDT in EtOH for at least 24 h in the dark. Disposable 20 mL polypropylene vials, which were rinsed with EtOH prior to use, were used for this procedure. ODT SAMs were prepared from 1 mM solutions in EtOH. After 24 h, Au(111) were carefully removed from the vials, rinsed with copious quantities of EtOH, dried under a stream of nitrogen, and fully analyzed. This assembly will be referred to as HDT/Au and ODT/Au in the remainder of this work.

2.3.5. PBd Attachment to HDT/Au and ODT/Au Monolayers by Thiol-Ene Chemistry

To reduce any disulfide bonds that may have formed at the monolayer surface, HDT/Au monolayers were immersed in a 100 mM dithiothreitol (DTT) solution in a 50 mM aqueous pH ~8 buffer.[56] ODT/Au control monolayers underwent the same treatment. The surfaces were then rinsed with copious amounts of ultrapure water, after which they were dried and placed in 20 mL glass scintillation vials, which contained at least 10-15 mL of a 10% w/v solution of PBd in THF, where the glass vials were rinsed with THF prior to use. This PBd/THF solution was prepared by heating the PBd in THF to solubilize it, although sonication could also be employed for this

purpose. To drive the thiol-ene chemistry, the vials were next placed under a 100 W soft white light for at least 24 h. After this reaction, the samples and controls were carefully removed from the vials, sonicated for 2 min in THF, rinsed with copious amounts of THF, dried under a stream of nitrogen, and analyzed. The sample assembly will be referred to as PBd/HDT/Au in the remainder of this work.

2.3.6. PBd Functionalization via Thiol-Ene Chemistry

The PBd/HDT/Au assembly was reacted with neat PDDT. Accordingly, a small volume of PDDT, enough to cover the surface, was dispensed onto a PBd/HDT/Au surface. A glass cover slip was placed over the liquid to make a sandwich. This sandwich was then placed in a glass Petri dish, which was sealed with Parafilm. The Petri dish was lined with a piece of filter paper that was wet with THF, and the sandwich sat on the filter paper. The sandwich/Petri dish were placed under a 100 W soft white light for at least 24 h and under these conditions the sandwiches did not dry out. Although, 24 h may be more than enough to complete the reaction, no effort was made optimize this exposure time. After reaction, the samples were carefully removed, washed with copious amounts of THF, dried under a stream of nitrogen, and analyzed. As a control, PBd/HDT/Au was also reacted with PFO under the same experimental conditions. The sample assembly will be referred to as PDDT/PBd/HDT/Au in the remainder of this work.

2.3.7. Modification of SiO_2/Si with MPTMS

Shards of SiO_2/Si were oxygen plasma cleaned (200 W) and then reacted with MPTMS by chemical vapor deposition (CVD) in a YES 1224P plasma/chemical vapor deposition system (Yield Engineering Systems, Livermore, CA). The samples were kept on the float plate for plasma

cleaning, which should lead to little or no increase in the oxide thickness.[57] The volume of the silane introduced to the vacuum chamber for CVD was 2 mL. This assembly will be referred to as MPTMS/SiO_2/Si in the remainder of this work.

2.3.8. Thiol-ene Chemistry on Thiol-Terminated SiO_2/Si

Shards of thiol-terminated Silicon wafer (MPTMS/SiO_2/Si) were reacted with PBd under the same experimental conditions as for HDT/Au. The PBd/MPTMS/SiO_2/Si assembly was then reacted with DNA-SH. As a control, PBd/MPTMS/SiO_2/Si was also reacted with otherwise identical non-thiolated DNA. The DNA-SH and DNA solutions were 100 μM in water with excess of tris(2-carboxyethyl)phosphine (TCEP). TCEP was added to reduce DNA-S-S-DNA to 2 DNA-SH. No effort was made to remove unreacted/reacted TCEP as it was not expected to interfere with the thiol-ene chemistry. Droplets of the DNA-SH and DNA solutions were placed on PBd/MPTMS/SiO_2/Si surfaces. No glass cover slip was placed over the surface. To prevent drying, the samples were placed in a 6" diameter Petri dish, which was then placed in a larger container with water at its bottom. The top of the container was covered with clear plastic wrap and exposed to soft white light for at least 24 h. Under these conditions, the droplets of DNA-SH and DNA solutions remained visible on the PBd/MPTMS/SiO_2/Si surfaces over the entire reaction period. After the reaction, the samples were rinsed with copious amounts of ultrapure water, dried with a stream of nitrogen, and analyzed by spectroscopic ellipsometry, contact angle goniometry, and XPS.

2.3.9. Stability Studies

The stability in the air of PDT/PBd/HDT/Au was compared to that of a PDT SAMs on Au(111). The PDT/PBd/HDT/Au assembly was prepared in the same way as PDDT/PBd/HDT/Au. The SAMs of PDT were prepared by immersing freshly prepared Au (111) in a 1 mM ethanolic solution of PDT in the dark for 24 h, after which the SAMs were rinsed with copious amounts of EtOH and dried under stream of nitrogen. Some samples of PDT/PBd/HDT/Au and PDT/Au were analyzed immediately after formation by XPS. Others were placed in empty beakers and covered with transparent plastic wrap. The plastic wrap was pierced at several spots to allow passage of air. The samples were kept in glass beakers for 2 weeks (in the air and exposed to room light), removed, rinsed with copious amounts of water, and analyzed by XPS.

2.3.10. Surface Analytical Techniques

Advancing water contact angles were measured with a contact angle goniometer (model 100-00) from Ramé-Hart Inc., Netcong, NJ. Thin film thicknesses were measured with an M-2000 ellipsometer from the J. A. Woollam Co., Lincoln, NE. XPS was performed with a model SSX-100 spectrometer with a hemispherical analyzer and a monochromatic Al Kα source. Time-of-flight secondary ion mass spectrometry (ToF-SIMS) was performed with a ToF-SIMS IV instrument (ION-TOF, Münster, Germany) with a gallium liquid metal ion source.

2.4. Results and Discussion

2.4.1. Preparation of SAMs and Attachment of PBd to SAMs

It is known that ethanolic solutions of ODT at millimolar concentrations can produce closely packed SAMs on gold surfaces. Literature thicknesses (ca. 22 Å)[18] and advancing water contact angles (ca. 114°)[58] of ODT SAMs closely match our results (see Table 2.1). For α,ω-dithiols, it had been a topic of debate whether they form monolayers in a standing up phase (one sulfhydryl group remaining unreacted) or in a lying down phase (both thiols binding to the surface). As recently shown by Esaulov et al., these results depend on the length of the dithiol;[58] dispersion forces between methylene units appear to play a crucial role in dithiol monolayer formation, where dithiols containing fewer than six methylene units were always found to attach to gold in a lying down phase. At six methylene units, the formation of a lying down or a standing up phase depends on reaction conditions (the solvent and oxygen content of the solvent), but dithiols with nine or more methylene units always produce monolayers in a standing up phase. Our HDT/Au monolayers (six methylene units) were consistently ca. 6-7 Å thick, which is about 1/3 the thickness of our ODT/Au monolayers (eighteen methylene units), and suggests a standing up phase. (With older HDT solutions or extended periods of self assembly, i.e. a few days, thicknesses up to 15 Å were observed, which might be due to multilayer formation via disulfide linkages. When these samples were immersed in DTT solutions for 10 minutes, a decrease in thickness was observed. In all experiments reported here, the self assembly of HDT on gold was stopped after 24 h by removing and rinsing the sample.) Water contact angles of HDT/Au monolayers were 62-72° (see Table 2.1). These and the ellipsometry results suggest that our HDT/Au monolayers exist in a standing up phase with free surface thiol groups. The attachment of PBd to these surfaces helps to further confirm this hypothesis (vide infra). XPS of ODT/Au monolayers show the expected

strong carbon signal. ToF-SIMS of both ODT/Au and HDT/Au shows S^- and SH^- peaks in its negative ion mode.

As formed, the HDT/Au surface may possess a few disulfide linkages that could affect the efficiency of thiol-ene chemistry. Hence, HDT/Au was activated by immersion in a solution of DTT for 10 minutes. The samples were then reacted with PBd. After this reaction, a consistent increase in thickness of 6.3-7.5 Å was observed (see Table 2.1), and advancing water contact angles increased to 81° which is very close to the reported contact angle of 87° of a PBd functionalized MPTMS/glass surface.[37] However, when a control surface, ODT/Au, was similarly exposed to PBd, no change in water contact angle or thickness was observed. This was expected because, unlike HDT/Au, there are no surface thiol groups on ODT/Au to react with PBd. Positive ion ToF-SIMS of HDT/Au and ODT/Au after reaction with PBd corroborates these claims. Figure 2.1a shows a reference spectrum for PBd,[44] where peaks at m/z = 77, 79, 91, and 105 are characteristic of this material. Figure 2.1b shows the ToF-SIMS spectrum of HDT/Au after reaction with PBd. All of the peaks characteristic of PBd are observed. Figure 2.1c shows the ToF-SIMS spectrum of ODT/Au after reaction with PBd. The characteristic peaks of PBd are missing. On the basis of these results we conclude that under our deposition conditions HDT forms SAMs in the standing up phase that successfully react with PBd to form PBd/HDT/Au assemblies.

#	HDT/Au		PBd/HDT/Au	
	Ellipsometric Thickness (Å)	Water Contact Angle (°)	Ellipsometric Thickness (Å)	Water Contact Angle (°)
1	6.9	68	13.8	81
2	6.1	72	12.4	79
3	7.3	62	14.8	82
Average	6.8 ± 0.6	67 ± 5	13.7 ± 1.2	81 ± 2

#	ODT/Au		ODT/Au reacted with PBd	
	Ellipsometric Thickness (Å)	Water Contact Angle (°)	Ellipsometric Thickness (Å)	Water Contact Angle (°)
a	23.3	112	22.3	>110
b	22.8	115	22.8	>110
c	21.7	114	21.7	>110
Average	22.6 ± 0.8	114 ± 2	22.3 ± 0.5	

Table 2.1. Characterization of 1,6-hexanedithiol/gold (HDT/Au) and octadecanethiol/gold (ODT/Au) monolayers by spectroscopic ellipsometry and advancing water contact angles before (left) and after (right) reaction with polybutadiene (PBd).

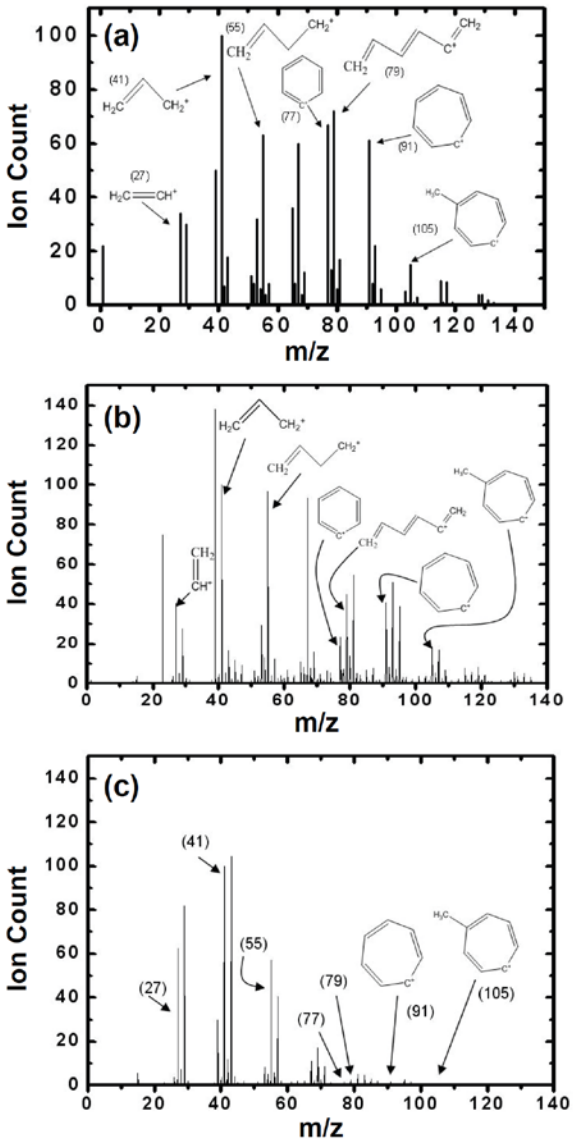

Figure 2.1. Positive ion mode ToF-SIMS spectrum (all spectra scaled to the m/z = 41 peak) of (a) PBd reference, (b) PBd/HDT/Au, and (c) ODT/Au 'reacted' with PBd.

2.4.2. Modification of PBd/HDT/Au by Thiol-Ene Chemistry

The PBd/HDT/Au assembly discussed in the previous section was expected to possess unreacted vinyl groups at its surface that could further react with different thiols through thiol-ene chemistry. Accordingly, PBd/HDT/Au assemblies were reacted with neat PDDT, a concentrated solution of ODT in THF, and also neat PFO as a control. When PBd/HDT/Au was reacted with PDDT, increases in thickness (6.3 Å) and advancing water contact angles (to 101.5°) were observed (see Table 2.2). When PBd/HDT/Au was reacted with ODT, an increase in thickness of 12.8 Å was observed, and the advancing water contact angle of the surface increased to 105° (see Table 2.2). These results suggest that, in addition to PDDT and ODT, a variety of thiols could be successfully attached to PBd/HDT/Au. As a control, PFO (bearing no SH group and thus not expected to react with PBd) was placed on PBd/HDT/Au. In this case, the thickness of the assembly increased slightly and its water contact angles dropped to the range of 55-65° (see Table 2.2). These results suggest a small degree of contamination of the surface (vide infra), but do not appear to be consistent with attachment of PFO. These results are further confirmed by XPS of the PBd/HDT/Au assembly after reaction with PDDT and PFO (see Figure 2.2). XPS is quite sensitive to fluorine. Interestingly, a strong F1s signal is observed after 'reaction' with both PDDT and PFO, which would appear to contradict the results above. However, a closer examination of the spectra, and in particular the XPS C1s narrow scans, shows a strong peak due to carbon chemically shifted by fluorine after the PBd/HDT/Au + PDDT reaction (Figure 2.2a), where this signal is completely absent after PBd/HDT/Au 'reacts' with PFO (Figure 2.2b). We conclude that the thiol-ene chemistry is working as expected, but that some contaminant, perhaps an inorganic fluoride, is introduced onto the PBd/HDT/Au surface from the PFO.

#	PDDT/PBd/HDT/Au		PBd/HDT/Au reacted with PFO	
	Ellipsometric Thickness (Å)	Water Contact Angle (°)	Ellipsometric Thickness (Å)	Water Contact Angle (°)
1	20.1	101	14.7	55
2	19.8	102	14.6	65
Average	20.0 ± 0.2	102 ± 1	14.7 ± 0.1	60 ± 5

#	ODT/PBd/HDT/Au	
	Ellipsometric Thickness (Å)	Water Contact Angle (°)
1	26.8	-
2	28.0	105
Average	27.4 ± 0.9	105

Table 2.2. Characterization of PBd/HDT/Au monolayers by spectroscopic ellipsometry and advancing water contact angles before (left) and after (right) reaction with 1H,1H,2H,2H-perfluorododecanethiol (PDDT) and perfluorooctane (PFO), respectively.

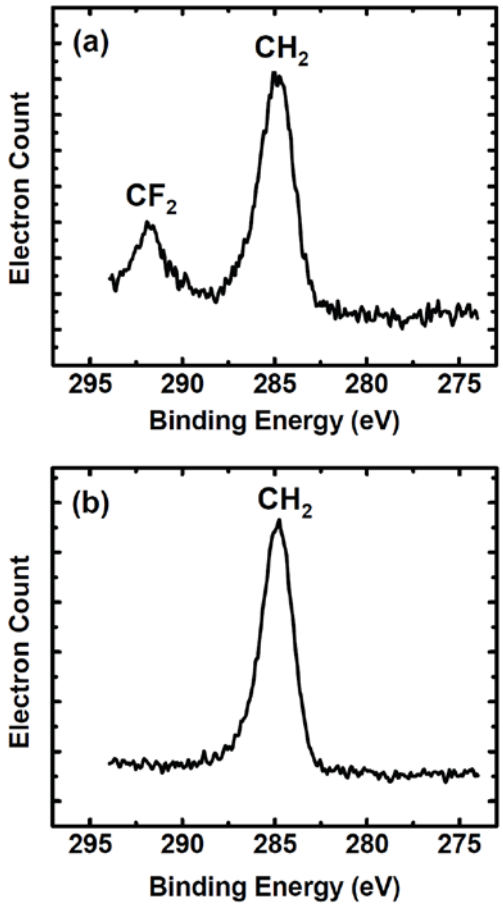

Figure 2.2. C1s XP narrow scans of (a) PDDT/PBd/HDT/Au and (b) PBd/HDT/Au 'reacted' with PFO.

2.4.3. Attachment of DNA-SH to PBd/MPTMS/SiO_2/Si

A question/concern raised in the previous section might be regarding the actual position of attachment of the PDDT and/or ODT to the PBd/HDT/Au surface. That is, while in theory the Au surface should be blocked by HDT, and it is further covered with a layer of PBd, one might argue that because of the well-known tendency for thiols to replace each other on gold,[59, 60] there are actually two possible attachment points for the thiols on PBd/HDT/Au: to the vinyl groups from PBd and to the gold surface itself. In other words, perhaps there is no reaction between vinyl groups on PBd and the two thiols, i.e., they simply bind to the gold surface. Of course the observed changes in water contact angles and ellipsometric thickness are more consistent with thiol attachment to vinyl groups in PBd than to the gold surface, but these data do not completely dismiss this issue. Accordingly, we created a thiolated monolayer using CVD of MPTMS on a different substrate that does not react with thiol groups: SiO_2/Si. This new monolayer (MPTMS/SiO_2/Si) was then reacted with PBd to make PBd/MPTMS/SiO_2/Si, which was in turn exposed to DNA-SH and DNA.

The thickness of the SiO_2 native oxide layer on Si(100) shard was not measured so we could not find the exact thickness of the MPTMS layer. However, assuming an SiO_2 thickness of 2 nm, which is very typical for the many native oxide layers we have measured in our laboratory, we find an increase in thickness of ca. 5 Å for MPTMS (see Table 2.3). The average water contact angle for MPTMS/SiO_2/Si was 65° (see Table 2.3), which closely matches the advancing water contact angle of the HDT/Au surface (see Table 2.1) as well as a literature value (~68°) for a thiol-terminated surface.[61] Note that these results further support the assumption above that our HDT/Au monolayer has (at least) a major contribution from its standing up phase. After reaction with PBd, MPTMS/SiO_2/Si surfaces showed increases in thickness of ~9 Å and water contact angles of 81°.

This thickness increase is a little more than was observed for the addition of PBd to HDT/Au, but the water contact angles of both surfaces are the same.

The PBd/MPTMS/SiO_2/Si samples were reacted with DNA-SH and an average increase in thickness of 7 Å and decrease in contact angle from 81° to 55° were observed (see Table 2.3). This was expected as DNA is more hydrophilic than PBd. For addition of the non-thiolated DNA, no difference in film thickness was observed, although the water contact angles of the surfaces decreased somewhat (see Table 2.3). XPS of these materials helps clarify these results. The XPS of PBd/MPTMS/SiO_2/Si reacted with DNA-SH showed a strong nitrogen peak, which is consistent with DNA-SH attachment (see Figure 2.3a). This peak is much smaller, but not entirely absent, in the control in which PBd/MPTMS/SiO_2/Si was 'reacted' with DNA (Figure 2.3b). Thus, it appears that a small amount of non-specific attachment occurred between DNA and the PBd/MPTMS/SiO_2/Si assembly, which would explain the surface characterization results. Hence, these results are consistent with specific and preferred DNA-SH attachment to PBd/MPTMS/SiO_2/Si via thiol-ene chemistry, and by extension they point to specific attachment of thiols to the vinyl groups of PBd/HDT/Au. We expect that the above prepared DNA terminated surfaces will also undergo hybridization with complementary DNA strands based on available literature where even electrostatically immobilized DNA probes demonstrated efficient hybridization.[62-64]

2.4.4. Stability Comparison of PDT/PBd/HDT/Au and PDT/Au

Freshly prepared PDT/PBd/HDT/Au and PDT/Au assemblies were analyzed by XPS. For both samples, the C 1s narrow scan obtained by XPS revealed two peaks. The peak at higher binding energy (~290 eV) corresponds to carbon bonded to >1 fluorine (C-F peak) and the peak at

#	MPTMS/Si		PBd/MPTMS/Si	
	Total Ellipsometric Thickness (Å)	Water Contact Angle (°)	Total Ellipsometric Thickness (Å)	Water Contact Angle (°)
1	25.7	67	35.2	80
2	25.0	62	37.5	80
3	26.1	63	34.3	82
4	28.9	68	34.0	82
Average	26 ± 2	65 ± 3	35 ± 2	81 ± 1

#	DNA-SH/PBd/MPTMS/Si		PBd/MPTMS/Si reacted with DNA	
	Total Ellipsometric Thickness (Å)	Water Contact Angle (°)	Total Ellipsometric Thickness (Å)	Water Contact Angle (°)
1	42.4	52	30.5	66
2	41.0	58	35.2	-
Average	42 ± 1	55 ± 4	33 ± 3	66

Table 2.3. Ellipsometric thicknesses and advancing water contact angles of 3-mercaptopropyltrimethoxysilane (MPTMS) thin films on Si, PBd-terminated MPTMS/Si surfaces, and PBd/MPTMS/Si surfaces after exposure to DNA-SH and DNA. 'Si' indicates silicon surfaces terminated with native oxide.

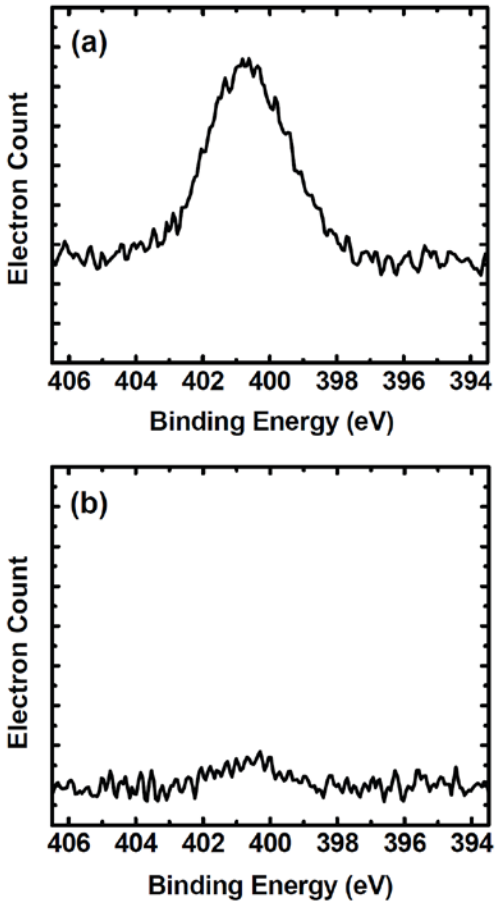

Figure 2.3. N1s XP narrow scans of (a) DNA-SH/PBd/MPTMS/Si and (b) PBd/MPTMS/Si reacted with DNA.

lower binding energy (~285 eV) corresponds to carbon bonded to carbon and/or hydrogen (C-C,H peak). For the PDT/PBd/HDT/Au sample, the relative height of the C-F peak is much less than the C-H peak as there is a huge network of HDT SAM and PBd, which contribute to this signal. In addition, the attachment of PDT to the PBd/HDT/Au surface by thiol-ene chemistry is not expected to yield a densely packed PDT layer (unlike a PDT SAM directly assembled on to a gold surface). As expected, for the PDT/Au sample, C-F peak is more intense than the C-H peak as 8 out of 10 carbon atoms in the PDT molecule are bonded to fluorine atoms. It is also clear that some hydrocarbon surface contamination is contributing to the C-H envelope for the samples analyzed in this section.

To mimic typical storage conditions for many laboratory materials, they were then exposed to air and light for 2 weeks, rinsed with copious quantities of ultrapure water, and reanalyzed by XPS (see Figure 2.4c, d). After exposure to air/light and rinsing, the C-F peak completely disappears from the C1s narrow scan of the PDT/Au monolayer. In contrast, for the PDT/PBd/HDT/Au assembly, the C-F peak is still present and largely unchanged. On the basis of these results we conclude that the PDT/PBd/HDT/Au assembly is much more chemically stable than PDT/Au. We attribute this increased stability to indirect surface anchoring of PDT through PBd, where the PBd in turn should be bonded to the surface at multiple points. The increased molecular weight of the adsorbate (the PDT/PBd adduct) no doubt also contributes to the observed stability. Hence, although the thiol groups of HDT may oxidize, they could still serve to anchor (and preserve) the assembly through multiple, weak interactions.

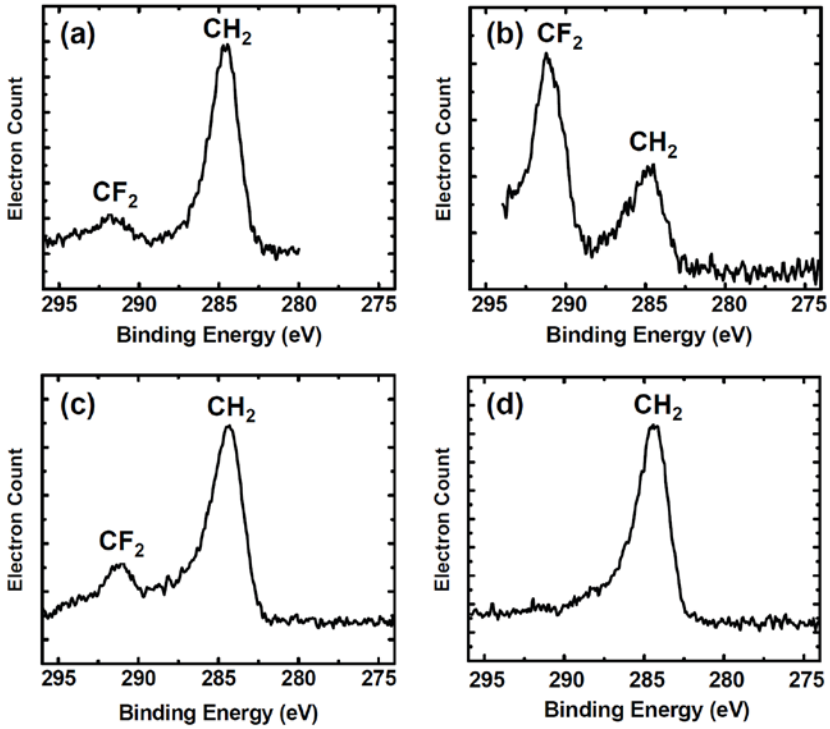

Figure 2.4. C1s XP narrow scans of (a) PDT/PBd/HDT/Au and (b) PDT/Au immediately after preparation and (c) PDT/PBd/HDT/Au and (d) PDT/Au after exposure to light and air for 2 weeks followed by rinsing with water.

2.5. Conclusions

We have demonstrated that fresh gold substrates can be successfully functionalized with robust assemblies consisting of dithiols followed by photochemical attachment of PBd, which can be further modified by functional thiols. The same chemistry is also operable on mercaptosilane monolayers on silicon dioxide. The chemisorbed PBd was functionalized with ODT, 1H,1H,2H,2H-perfluoroalkanethiol, and DNA-SH. The PDT/PBd/HDT/Au assembly is more stable in air and light than the thiol directly attached to the gold surface. This more stable assembly may serve as a substrate for a variety of applications, such as sensing, nanotechnology, and biotechnology.

2.6. Acknowledgment

The authors gratefully acknowledge funding from the National Science Foundation (CBET-0708347) and the Max Planck Society. Elisabeth Pound is thanked for her help in providing thiolated and non-thiolated DNA.

2.7. References

1. Nuzzo, R. G.; Allara, D. L. *J.Am.Chem.Soc.* **1983,** *105*, 4481-4483.

2. Ford, M. J.; Masens, C.; Cortie, M. B. *Surf. Rev. Lett.* **2006,** *13*, 297-307.

3. Schreiber, F. *J. Phys. Cond. Mat.* **2004,** *16*, R881-R900.

4. Vericat, C.; Vela, M. E.; Salvarezza, R. C. *Phys. Chem. Che. Phys.* **2005,** *7*, 3258-3268.

5. Love, J. C.; Estroff, L. A.; Kriebel, J. K.; Nuzzo, R. G.; Whitesides, G. M. *Chem. Rev.* **2005,** *105*, 1103-1169.

6. Vericat, C.; Vela M, E.; Benitez, G.; Carro, P.; Salvarezza, R. C. *Chem. Soc. Rev.* **2010,** *39*, 1805-1834.

7. Schreiber, F. *Prog. Surf. Sci.* **2000,** *65*, 151-256.

8. Willey, T. M.; Vance, A. L.; Van Buuren, T.; Bostedt, C.; Terminello, L. J.; Fadley, C. S. *Surf. Sci.* **2005,** *576* 188-196.

9. Lewis, M.; Tarlov, M.; Carron, K. J. *Am. Chem. Soc.* **1995,** *117*, 9574-9575.

10. Zhang, Y.; Terrill, R. H.; Bohn, P. W. *Chem. Mater.* **1999,** *11*, 2191-2198.

11. Ito, E. N., J.; Hara, M. *Chem. Phys. Lett.* **2008,** *462*, 209-212.

12. Garg, N.; Carrasquillo-Molina, E.; Lee, T. R. *Langmuir* **2002,** *18*, 2717-2726.

13. Hutt, D. A.; Leggett, G. J. *J. Phys. Chem.* **1996,** *100*, 6657-6662.

14. Lee, M. T.; Hsueh, C. C.; Freund, M. S.; Ferguson, G. S. *Langmuir* **1998,** *14*, 6419-6423.

15. Flynn, N. T.; Tran, T. N. T.; Cima, M. J.; Langer, R. *Langmuir* **2003,** *19*, 10909-10915.

16. Jans, K.; Bonroy, K.; De Palmas, R.; Reekmans, G.; Jans, H.; Laureyn, W.; Smet, M.; Borghs, G.; Maes, G. *Langmuir* **2008,** *24*, 3949-3954.

17. Chandekar, A.; Sengupta, S. K.; Whitten, J. E. *Appl. Surf. Sci.* **2010,** *256*, 2742-2749.

18. Booth, B. D.; Vilt, S. G.; McCabe, C.; Jennings, G. K. *Langmuir* **2009,** *25*, 9995-10001.

19. Linford, M. R.; Fenter, P.; Eisenberger, P. M.; Chidsey, C. E. D. *J. Am. Chem. Soc.* **1995,** *117*, 3145-3155.

20. Lua, Y.-Y.; Niederhauser, T. L.; Matheson, R.; Bristol, C.; Mowat, I. A.; Asplund, M. C.; Linford, M. R. *Langmuir* **2002,** *18*, 4840-4846.

21. Jiang, G.; Niederhauser, T. L.; Davis, S. D.; Lua, Y.-Y.; Cannon, B. R.; Dorff, M. J.; Howell, L. L.; Magleby, S. P.; Linford, M. R., *Colloids Surf., A* **2003,** *226*, 9-16.

22. Valiokas, R.; Östblom, M.; Svedhem, S.; Svensson, S. C. T.; Liedberg, B. *J. Phys. Chem. B* **2002,** *106*, 10401-10409.

23. Turchanin, A.; El-Desawy, M.; Gölzhäuser, A. *Appl. Phys. Lett.* **2007,** *90*, 053102.

24. Carey, R. I.; Folkers, J. P.; Whitesides, G. M. *Langmuir* **1994,** *10*, 2228-2234.

25. Doneux, T.; Steichen, M.; De Rache, A.; Buess-Herman, C. *J. Electroanal. Chem.* **2010,** *649*, 164-170.

26. Cortes, E.; Rubert, A. A.; Benitez, G.; Carro, P.; Vela M, E.; Salvarezza, R. C. *Langmuir* **2009,** *25*, 5661-5666.

27. Oçafrain, M.; Tran, T. K.; Blanchard, P.; Lenfant, S.; Godey, S.; Vuillaume, D.; Roncali, J. *Adv. Funct. Mater.* **2008,** *18*, 2163-2171.

28. Fujihara, H.; Nakai, H.; Yoshihara, M.; Maeshima, T. *Chem. Commun.* **1999**, 737-738.

29. Liu, H.; Liu, S.; Echegoyen, L. *Chem. Commun.* **1999**, 1493-1494.

30. Kim, T.; Chan, K. C.; Crooks, R. M. *J. Am. Chem. Soc.* **1997,** *119*, 189-193.

31. Ishida, T.; Sano, M.; Fukushima, H.; Ishida, M.; Sasaki, S. *Langmuir* **2002,** *18*, 10496-10499.

32. Tai, Y.; Shaporenko, A.; Grunze, M.; Zharnikov, M. *J. Phys. Chem. B* **2005,** *109*, 19411-19415.

33. Chesneau, F.; Hamoudi, H.; Schüpach, B.; Terford, A.; Zharnikov, M. *J. Phys. Chem. C* **2011**, *115*, 4773-4782.

34. Beyer, A.; Godt, A.; Amin, I.; Nottbohm, C. T.; Schmidt, C.; Zhao, J.; Golzhauser, A. *Phys. Chem. Chem. Phys.* **2008,** *10*, 7233-7238.

35. Clegg, R. S.; Reed, S. M.; Hutchison, J. E. *J. Am. Chem. Soc.* **1998,** *120*, 2486-2487.

36. Zhang, H.; Xia, H.; Li, H.; Liu, Z. *Chem. Lett.* **1997,** *26*, 721-722.

37. Jonkheijm, P.; Weinrich, D.; Köhn, M.; Engelkamp, H.; Christianen, P. C. M.; Kuhlmann, J.; Maan, J. C.; Nüsse, D.; Schroeder, H.; Wacker, R.; Breinbauer, R.; Niemeyer, C. M.; Waldmann, H. *Angew. Chem. Int. Ed.* **2008,** *47*, 4421-4424.

38. Bertin, A.; Schlaad, H. *Chem. Mater.* **2009,** *21*, 5698-5700.

39. Campos, L. M.; Meinel, I.; Guino, R. G.; Schierhorn, M.; Gupta, N.; Stucky, G. D.; Hawker, C. J. *Adv. Mater.* **2008,** *20*, 3728-3733.

40. Smythe, E. J.; Dickey, M. D.; Whitesides, G. M.; Capasso, F. *ACS Nano* **2008,** *3*, 59-65.

41. Campos, L. M.; Truong, T. T.; Shim, D. E.; Dimitriou, M. D.; Shir, D.; Meinel, I.; Gerbec, J. A.; Hahn, H. T.; Rogers, J. A.; Hawker, C. J. *Chem. Mater.* **2009,** *21*, 5319-5326.

42. Wendeln, C.; Rinnen, S.; Schulz, C.; Arlinghaus, H. F.; Ravoo, B. J. *Langmuir* **2010,** *26*, 15966-15971.

43. Niehaus, J. C.; Hirtz, M.; Brinks, M. K.; Studer, A.; Fuchs, H.; Chi, L. *Langmuir* **2010,** *26*, 15388-15393.

44. Gupta, N.; Lin, B. F.; Campos, L. M.; Dimitriou, M. D.; Hikita, S. T.; Treat, N. D.; Tirrell, M. V.; Clegg, D. O.; Kramer, E. J.; Hawker, C. J. *Nat. Chem.* **2010,** *2*, 138-145.

45. Wickard, T. D.; Nelsen, E.; Madaan, N.; Brummelhuis, N. T.; Diehl, C.; Schlaad, H.; Davis, R. C.; Linford, M. R. *Langmuir* **2010,** *26*, 1923–1928.

46. Goldmann, A. S.; Walther, A.; Nebhani, L.; Joso, R.; Ernst, D.; Loos, K.; Barner-Kowollik, C.; Barner, L.; Müller, A. H. E. *Macromolecules* **2009,** *42*, 3707-3714.

47. Diehl, C.; Schlaad, H. *Chem. Eur. J.* **2009,** *15*, 11469-11472.

48. Li, Y.-H.; Wang, D.; Buriak, J. M. *Langmuir* **2010,** *26*, 1232-1238.

49. Khire, V. S.; Harant, A. W.; Watkins, K. S.; Anseth, K. S.; Bowman, C. N. *Macromolecules* **2006,** *39*, 5081-5086.

50. Pound, E.; Ashton, J. R.; Becerril, H. A.; Woolley, A. T. *Nano Lett.* **2009,** *9*, 4302–4305.

51. Liu, J.; Schüpbach, B.; Bashir, A.; Shekhah, O.; Nefedov, A.; Kind, M.; Terfort, A.; Wöll, C. *Phys. Chem. Che. Phys.* **2010,** *12*, 4459-4472.

52. Tsai, M.; Lin, J. *J. Colloid Interface Sci.* **2001,** *238*, 259-266.

53. Smith, T. *J. Colloid Interface Sci.* **1980,** *75*, 51-55.

54. McDermott, C. A.; McDermott, M. T.; Green, J. B.; Porter, M. D. *J. Phys. Chem.* **1995,** *99*, 13257-13267.

55. Ron, H.; Matlis, S.; Rubinstein, I. *Langmuir* **1998,** *14*, 1116-1121.

56. Harant, A. W.; Khire, V. S.; Thibodaux, M. S.; Bowman, C. N. *Macromolecules* **2006,** *39*, 1461-1466.

57. Zhang, F.; Sautter, K.; Davis, R. C.; Linford, M. R. *Langmuir* **2009,** *25*, 1289-1291.

58. Millone, M. A. D.; Hamoudi, H.; Rodriguez, L.; Rubert, A.; Benitez, G. A.; Vela, M. E.; Salvarezza, R. C.; Gayone, J. E.; Sánchez, E. A.; Grizzi, O.; Dablemont, C.; Esaulov, V. A. *Langmuir* **2009,** *25*, 12945-12953.

59. Tarlov, M. J.; Burgess, D. R. F., Jr.; Gillen, G. *J. Am. Chem. Soc.* **1993,** *115*, 5305-5306.

60. Tarlov, M. J.; Newman, J. *Langmuir* **1992,** *8*, 1398-1405.

61. Aldakov, D.; Bonnassieux, Y.; Geffroy, B.; Palacin, S. *Appl. Mater. Interfaces* **2009,** *1*, 584-589.

62. Díaz-González, M.; de la Escosura-Muñiz, A.; González-García, M. B.; Costa-García, A. *Biosens. Bioelectron.* **2008,** *23*, 1340-1346.

63. Zhou, X. C.; Huang, L. Q.; Li, S. F. Y. *Biosens. Bioelectron.* **2001,** *16*, 85-95.

64. Zhou, X.; Wu, L.; Zhou, J. *Langmuir* **2004,** *20*, 8877-8885.

Chapter 3: Complex, Stable Molecular Assemblies Prepared by the Integration of Multiple Surface Reactions: Layer-by-Layer, Thiol-ene, Bioconjugate, and Silanization Chemistries

Note: The work presented in this section is will be submitted to a journal for review as Madaan, N., Tuscano, J., Romriell, N., Schlaad, H., Linford, M. R., Complex, Stable Molecular Assemblies Prepared by the Integration of Multiple Surface Reactions: Layer-by-Layer, Thiol-ene, Bioconjugate, and Silanization Chemistries.

3.1. Abstract

In this work, I explore the formation of complex molecular assemblies prepared from multiple surface chemistries that include: the layer-by-layer (LBL) deposition of polyelectrolytes, thiol-ene chemistry, bioconjugate chemistry, and silanization. More than 100 different polyallylamine hydrochloride (PAH)/polyacrylic acid (PAA) LBL assemblies were prepared at either pH 5 or 8 and their surface properties were averaged and plotted. To the best of my knowledge, this is the largest set of PAH/PAA samples that has been prepared and reported in the literature, and I explore their thermal cross-linking over a wider range of conditions than has been previously reported. The stability of the resulting assemblies was also explored. Even with the monochromatic X-ray source, some sample damage/cross-linking was observed during sample analysis by XPS. Amine groups at the surfaces of these assemblies were converted to –SH groups with Traut's reagent, and this reaction was optimized with regards to temperature, concentration, and pH. The oxidation state of the adsorbed thiols was probed by XPS; sulfur-containing species were found to exist as thiolates ($-S^-$), thiols (-SH), or oxidized sulfur. The $-S^-$ content of the surfaces could be lowered by rinsing with dilute acetic acid. Even relatively limited exposure of these

assemblies to air resulted in oxidation of the thiols and thiolates. Molecular assemblies terminated with –SH could be modified with 1,2-polybutadiene (PBd) via thiol-ene chemistry under 254 nm light. Excessive exposure to UV light damaged the assemblies. A second thiol-ene reaction with a fluorinated thiol could be performed on PBd-terminated assemblies. Surfaces with high water contact angles (ca. 120°) were obtained. After long immersions (9 days) in water, these films lifted off their substrates. Surface silanization with an amino silane prevented this delamination and led to very stable assemblies. Water droplet pinning could be controlled on these hydrophobic assemblies by varying the thermal cross-linking.

3.2. Introduction

For at least the last two decades, surface modification has been a very active area of research in modern science because of the many potential applications of functionalized surfaces in biosensors, fuel cells, photovoltaics, bioconjugate chemistry, molecular electronics, adhesion, and microfluidics.[1] Some of the basic building blocks of such advanced materials are self-assembled monolayers on gold,[2-4] organosilane monolayers on hydroxylated surfaces,[5-9] alkene and alkyne monolayers on hydrogen-terminated silicon,[10-15] phosphonates on alumina, zirconia, and related substrates,[16-19] the many reactions of bioconjugate chemistry,[20] the layer-by-layer assembly of polyelectrolytes and other charged species,[21-24] thiol-ene chemistry,[25-29] and carbon nanotubes.[30-32] Complex molecular assemblies on surfaces may be prepared using combinations of different surface chemistries that are compatible with a specific substrate and each other.

Of all their possible applications, complex molecular assemblies may prove to be of greatest value in the field of molecular electronics.[33-35] That is, with the shrinking feature sizes of modern electronic devices, we are entering the realm of molecular nanotechnology that is well

beyond the diffraction limits of visible and even most UV light. It is conceivable that in this realm devices will increasingly be prepared in a bottom up approach by self-assembly. The realization of this goal will require precise control of molecular components using reliable surface chemistries, where in general, more than one type of molecular component will be deposited and more than one type of surface chemistry will be employed. Much has been done in this regard – some of this research has been performed in Linford's research group at BYU, which I joined as a graduate student in 2008 – and much remains to be undertaken.[1, 36-37]

To continue contributing to this effort, I explore herein and also combine a series of surface chemistries to form a complex molecular assembly. In particular, I explore the capabilities of and interplay between the layer-by-layer (LBL) assembly of polyelectrolytes, a reaction from bioconjugate chemistry (the conversion of an amine to a thiol with Traut's reagent (2-iminothiolane)), thiol-ene chemistry, and surface silanization. Film growth and composition have been confirmed by surface analytical techniques such as X-ray photoelectron spectroscopy (XPS), spectroscopic ellipsometry (SE), atomic force microscopy (AFM), and contact angle goniometry to optimize and understand the experimental conditions at each modification step.

In particular, I begin this study with the layer-by-layer (LBL) deposition of polyallylamine hydrochloride (PAH) and polyacrylic acid (PAA). There are a number of reports of this system in the literature.[38-41] However, here I synthesized and characterized (with the help of other team members) more than 100 different PAH/PAA coated surfaces that were prepared at two different solution pH values: ca. 5 or ca. 8. Consistent with previous observations,[42] exponential film growth was observed. Thicker films began to show visible defects and become rougher, as determined by AFM. These films were then thermally cross-linked.[42] The effect of cure temperature (150 – 250 °C) and time (1 – 3 h) on the extent of thermal cross-linking was investigated. Amide bond

formation was expected here. X-ray photoelectron spectroscopy showed the expected reduction in the quantity of oxygen after cross-linking. Films also decreased in thickness after cross-linking. Uncross-linked PAH/PAA assemblies were stable against sonication in water (20 min), tetrahydrofuran (THF) (15 min), and ethanol (20 min). In a pH 1.68 buffer, the uncross-linked assembly desorbs from the substrate, while the cross-linked assembly is unaffected. Cross-linked assemblies are more stable at elevated pH than their uncross-linked counterparts.

Amine groups at the surfaces of uncross-linked and cross-linked PAH-terminated PAH/PAA assemblies ($(PAH/PAA)_nPAH$) could be converted into thiols using a well-known reagent from bioconjugate chemistry: Traut's reagent.[43-44]

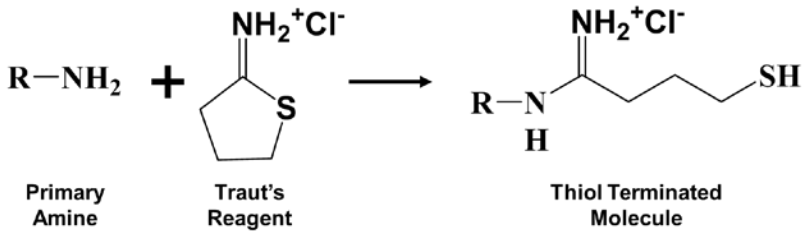

This reaction was explored at two temperatures (0 and 20 °C), at three concentrations of Traut's reagent (0.001, 0.01, and 0.1 M), and at two pH values: 5 and 8. This reaction was favored at higher temperatures, higher concentrations of Traut's reagent, and higher pH values.

Thiols are prone to oxidation, and oxidized thiols are not expected to undergo thiol-ene chemistry. Accordingly, the oxidation states of the thiol-terminated surfaces were investigated. XPS narrow scans of the 2s region of sulfur could be fit to three peaks, suggesting three oxidation states for sulfur that were attributed to oxidized sulfur, –SH groups, and thiolate ($-S^-$) groups. Rinsing of the assemblies in dilute acetic acid converted surface $–S^-$ groups into –SH groups. Even a day or two of exposure to the air resulted in a considerable decrease in the surface thiolate and

thiol concentrations. Thus, the –SH terminated assemblies were used immediately after their preparation.

Thiol-ene reactions constitute an extremely versatile chemistry for creating molecular assemblies and modifying surfaces,[25-26, 29] and thiol-terminated assemblies underwent a reaction with 1,2-polybutadiene (PBd) under UV light. The addition of PBd to the surfaces substantially changed their wetting properties. Excessive exposure to UV light damaged and even destroyed the assemblies.

Obviously not all of the carbon-carbon double bonds in the chemisorbed PBd react with –SH groups from Traut's reagent upon chemisorption because PBd-terminated assemblies undergo further thiol-ene chemistry with perfluorordecanethiol. Surfaces with high water contact angles (ca. 120°) are thus obtained. As before, longer exposures to UV light destroyed the assemblies. After long immersions in water, $(PAH/PAA)_n$/PAH/Traut's reagent/PBd/perfluorordecanethiol assemblies delaminated/lifted off their substrates. Silanization of the substrates with (3-aminopopyl)triethoxysilane (APTES) to form APTES/cross-linked $(PAA/PAH)_n$/Traut's reagent/PBd/perfluorordecanethiol assemblies prevented this delamination, i.e., amide bond formation was expected between the amino groups from the silane and carboxyl groups from the PAA. These assemblies were stable against ethanol wipes and the Scotch tape test. The wetting of these complex assemblies was affected by the degree of cross-linking in them.

I would like to emphasize that the purpose of this work was not to build a molecular assembly with a direct commercial or practical application. Rather, the focus of this work is to explore the interplay between a unique combination of important surface chemistries, while simultaneously providing more extensive surface/material characterization, optimization, and understanding than is currently in the literature. I learnt that application of the right surface

chemical reactions play a very crucial role in overall properties of the molecular assembly. In this work, employing cross-linked LBL layers beneath PDT modified PBd layers imparted unique water droplet pinning properties (tunable) to the whole assembly. Such properties are harder to achieve and usually accomplished by using a tedious patterning procedure. But in this work, such properties were achieved in a very facile manner.

3.3. Experimental

3.3.1. Materials

Polyallylamine hydrochloride (PAH) (M_w~58000), polyacrylic acid (PAA) (M_w~10000), 1,2-polybutadiene (PBd) (approx. 90% 1,2-vinyl), triethanolamine hydrochloride (TEA, ≥ 99.0 %) and 1H,1H,2H,2H-perfluorodecanethiol (PDT, 99.0 %) were purchased from Sigma-Aldrich (St. Louis, MO). Traut's reagent was purchased from ProteoChem (Denver, CO). Ethanol (200 proof) was obtained from Decon Laboratories (King of Prussia, PA). Stabilized THF was obtained from Mallinckrodt, Phillipsburg, NJ. The water (resistivity 18 MΩ-cm) used for making solutions and rinsing surfaces was obtained from a Milli-Q water system by Millipore (Billerica, MA). Silicon wafers (Si/SiO_2), 4 inches in diameter, with (100) crystallographic orientation and native oxide were obtained from University Wafers (Boston, MA).

3.3.2. Electrostatic Layer-by-Layer (LBL) Assembly of PAH and PAA

Aqueous solutions of polyallylamine hydrochloride (PAH) (0.02 M) and polyacrylic acid (PAA) (0.01 M) were prepared in high purity water. The pH values of the PAH and PAA solutions were adjusted using dilute NaOH to ~5 and ~5.7 or to ~8 and 8.7, respectively. Shards of Si(100), ca. 1.5 x 1.5 cm^2, were cleaned either for 1 min with an air plasma cleaner (Model PDC-32G from

Harrick Plasma, Ithaca, NY) or in piranha solution (H_2O_2:H_2SO_4, 30:70) to remove organic contamination. Clean silicon shards were then immersed sequentially in a solution of PAH, ultrapure water, a solution of PAA, and again in ultrapure water. Immersion times were 5 min in each case. Between each immersion, silicon shards were rinsed with copious amounts of Millipore water and dried with a stream of nitrogen (N_2). This LBL deposition of the polyelectrolytes was repeated until the desired thickness of the assembly was obtained. These films were prepared by three different laboratory workers (myself, Joshua Tuscano, and Naomi Romriell), and from solutions prepared on different days. Fresh polyelectrolyte solutions were not prepared if older solutions (1 to 15 days old) were available. Increases in thickness were monitored by spectroscopic ellipsometry (SE) after the majority of the deposition steps for more than 100 individual samples. The samples were also analyzed by XPS and AFM.

3.3.3. Thermal Cross-Linking

The LBL assemblies prepared as described above were placed individually in a glass tube (25 mm inner diameter), and the center portion of the glass tube was wrapped with heating tape. A thermocouple was inserted into the tube to provide feedback to a PID controller to automatically maintain the temperature in it. An inert atmosphere was then created in the tube by flowing N_2 gas through it. In this manner, electrostatic LBL assemblies were heated at 150 °C, 200 °C, and 250 °C for 1, 2, and 3 hrs. The samples were then characterized by SE, XPS, and contact angle goniometry.

3.3.4. Conversion of Amines to Thiols

Amine groups were converted into thiols in an aqueous solution at ca. pH 5 of 0.1, 0.01, or 0.001 M Traut's reagent. The pH of the ultrapure (Millipore) water used to make the solutions was

ca. 5, and no effort was made to adjust the pH of these solutions after addition of Traut's reagent. For the pH 8 reactions, triethanolamine (TEA), 3.73 g, was dissolved in 25 mL of high purity water and the pH of this solution was adjusted to ca. 8.0 using conc. HCl. Traut's reagent was then added to this solution to prepare 0.1, 0.01, or 0.001 M solutions of this reagent. All solutions were made fresh, immediately before they were used. Cross-linked and uncross-linked PAH-terminated LBL assemblies were immersed in 1.5 mL of one of these solutions for 30 min, after which they were rinsed with copious amounts of Millipore water and dried under a stream of N_2 gas. The resulting samples were characterized by XPS, time-of-flight secondary ion mass spectrometry (ToF-SIMS), contact angle goniometry, and SE.

3.3.5. Thiol-ene Chemistry

A UV lamp (254 nm, 18 Watt) was mounted inside a polyethylene glove bag that was continuously purged with N_2. Thiol-terminated LBL assemblies were immersed in 12.5 – 50% w/v PBd/THF solutions in Teflon containers and exposed to UV light for 5 – 11 h. Samples were then rinsed with THF, sonicated in THF for 5 minutes, rinsed with THF again, and dried with a stream of nitrogen. The PBd-terminated samples created in this way were then immersed in neat perfluorordecanethiol (PDT) in Teflon containers and again exposed to UV light for 4 – 12 h in an N_2 purged glove bag. The resulting samples were characterized by SE and contact angle goniometry.

3.3.6. APTES Deposition

Air plasma cleaned silicon substrates were placed in 2% solutions of 3-aminopropyltriethoxysilane (APTES) in toluene for 15 min at 100 °C, after which the surfaces were rinsed thoroughly with toluene.

3.3.7. Sample Characterization

Sessile water contact angles were determined with 20 μL water droplets using a contact angle goniometer (model 100-00, Ramé-Hart Inc., Netcong, NJ). Film thicknesses were measured by spectroscopic ellipsometry (SE) at 70˚ over a wavelength range of ca. 200 – 1000 nm (M-2000D, J. A. Woollam Co., Lincoln, NE). The substrates were modeled using the optical constants of silicon in the instrument software, and the native oxide and polyelectrolyte multilayers were modeled using the optical constants of SiO_2, also from the instrument software. X-ray photoelectron spectroscopy (XPS)[45] was performed with an SSX-100 ESCA spectrometer from Surface Science equipped with a hemispherical analyzer and a monochromatic Al Kα (1486.6 eV) source. Sample roughnesses were determined using a Veeco Dimension V AFM (Digital Instruments Inc., Santa Barbara, CA). ToF-SIMS was performed with a ToF-SIMS IV instrument (ION-TOF, Münster, Germany) with a gallium, Ga^+, liquid metal ion source.

3.4. Results and Discussion

3.4.1. LBL Assembly of Films of PAH and PAA

The LBL deposition of PAH and PAA was explored with solutions of these polyelectrolytes at ca. pH 5.0 and 5.7, respectively.[42, 46] These pH values were previously employed by Bruening et al.[42] A series of assemblies was also prepared at ca. pH 8.0 (PAH

solution) and 8.7 (PAA solution). For this latter set of solutions I preserved the ca. 0.7 pH unit difference between the solutions used at ca. pH 5. At either set of pH values, PAH will exist in a substantially protonated form, and PAA will exist in a substantially deprotonated form. Accordingly, attractive interactions are expected between the cations in the PAH and the anions in the PAA.

The growth of PAH/PAA LBL films was monitored by spectroscopic ellipsometry (SE) for 48 different samples prepared at ca. pH 5 and 60 samples at ca. pH 8. However, more SE measurements were made at pH 5 because the sample thickness was measured after almost every deposition for almost all of the 48 samples, and a larger number of layers (22 vs. 12) was prepared at ca. pH 5 (see Figure 3.1). Interestingly, the layer-by-layer growth at the two solution pH values was very similar. A plot comparing the growth curves at pH 5 and pH 8 are given in Figure 3.2. To this best of my knowledge, this is the most extensive study reported to date of PAH/PAA film growth.

In agreement with previous reports[42], exponential growth was observed for both the ca. pH 5 (see Figure 3.1) and ca. pH 8 solutions (see Figure 3.2). The thinner (< 200 Å) LBL films were pristine (visually appeared as uncoated silicon wafers). On a few of the thicker (> 200 Å) films, defects that looked like water spots were observed. The roughnesses of the LBL films determined by AFM also increased with increasing film thickness, ranging from ca. 1 nm for the thinner films to ca. 6 nm for the thickest. These roughness measurements were made on at least two different spots chosen randomly on at least two different assemblies for every polyelectrolyte deposition. Clearly, the larger SE RSDs and increased number of visible defects in the thicker films are consistent with their greater AFM roughnesses. However, if a series of samples was made at the same time, with the same polyelectrolyte solutions, and also by the same laboratory worker (see

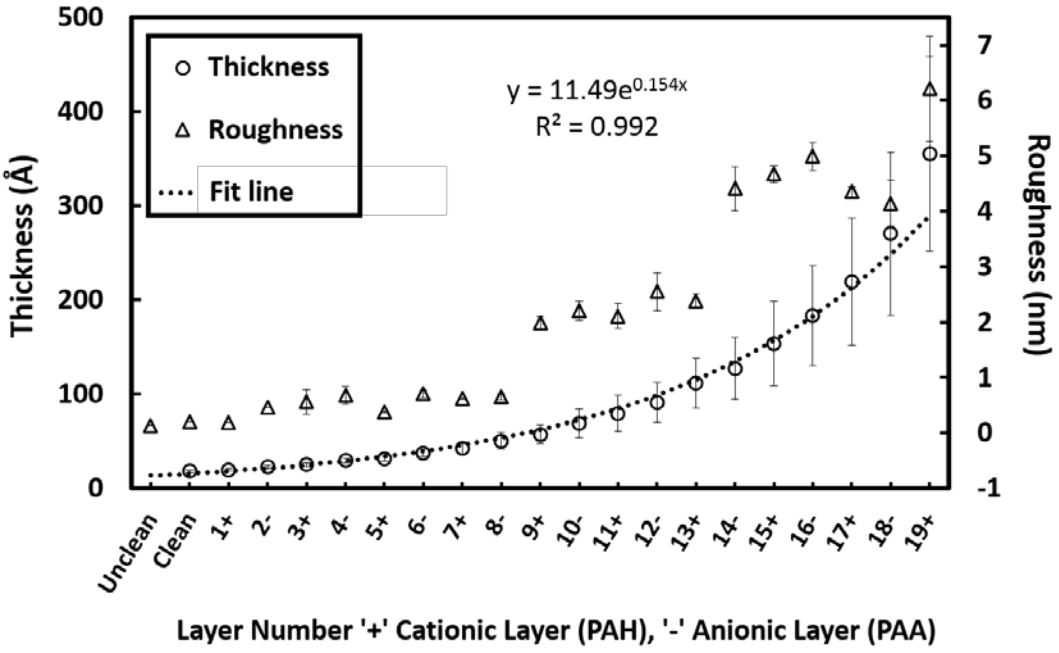

Figure 3.1. Thicknesses and roughnesses of PAH/PAA LBL assemblies prepared at pH 5 on silicon substrates. The numbers on the x-axis represent the total number of adsorbed layers (PAH or PAA). The '+' and '–' symbols on the x-axis labels represent the nature of the final polyelectrolyte layer: cationic (+) or anionic (-).

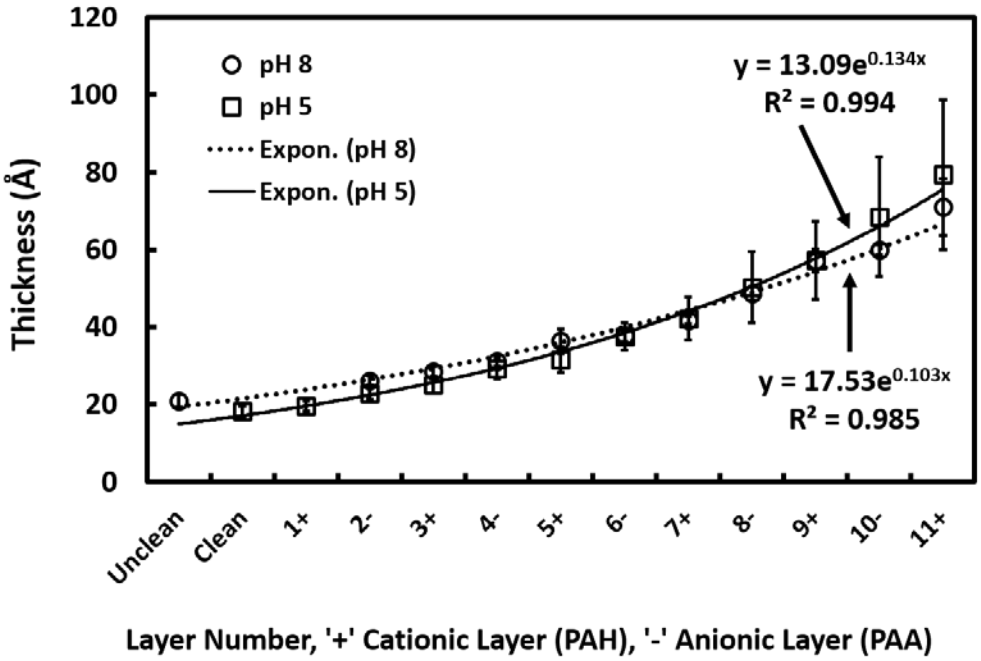

Figure 3.2. Comparison of the thicknesses of PAH/PAA LBL assemblies prepared at pH 8 and pH 5 on silicon substrates. The numbers on the x-axis represent the total number of adsorbed layers (PAH or PAA). The '+' and '–' symbols on the x-axis labels represent the nature of the final polyelectrolyte layer: cationic (+) or anionic (-).

Experimental for description of deposition conditions), the RSDs of the resulting thicknesses would vary over a narrower range: from ca. 1% for the thinner films to ca. 5% for the thickest. That is, small changes in solution concentration, the age of the solution, and/or subtle user-to-user differences in sample preparation appear to affect film growth, where these changes become most apparent after many growth cycles. Nevertheless, these results indicate that, overall, reasonable reproducibility is obtained with these depositions, especially for the thinner films.

3.4.2. Stability of LBL PAH/PAA Assemblies to XPS Analysis

The stability of LBL PAH/PAA assemblies to XPS/high vacuum analysis was tested. Initially, the compatibility of the sample to the vacuum environment was evaluated. After 26 h under high vacuum (ca. 10^{-8} Torr), the thickness of PAH/PAA films decreased by only 2 ± 1% That is, samples showed good stability in the vacuum, and this small decrease in thickness is attributed to the loss of water/film dehydration. A sample was then analyzed at the same spot thrice – the sample was not moved between analyses so the beam continually irradiated it at this point. Each analysis consisted of a survey scan and a set narrow scans. The resulting N 1s peak envelopes are shown in Figure 3.3. In all cases, they can be well fit by two 100% Gaussians constrained to have equal widths. The use of 100% Gaussians seemed appropriate in light of Crist's suggestion to use 100:0 or 90:10 Gaussian:Lorentzian peaks to fit narrow scans of polymeric materials.[47-48] (No doubt, an underlying reason for Crist's recommendation is the significant degree of disorder in most polymers.) Interestingly, the N 1s narrow scans did not stay constant during the scans; the peak at lower binding energy grew in size throughout the analyses. The O 1s/ N 1s ratios (based on narrow scans and corrected for atomic sensitivity factors, etc.) also changed, dropping from 2.31 initially to 2.06 and then 1.97 after the second and third scans, respectively. This drop in

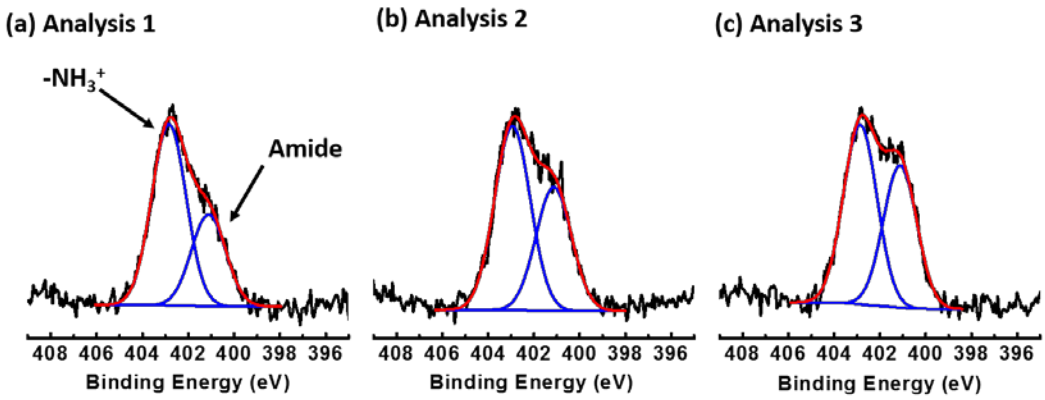

Figure 3.3. XPS N 1s narrow scans fitted with two 100% Gaussians of equal width from three identical analyses performed sequentially on the same spot on uncross-linked LBL samples. The peak positions of the '-NH_3^+' and 'Amide' signals were allowed to float in the fitting. The signals of these peaks were 402.8 eV and 401.1 eV, 402.9 eV and 401.1 eV, and 402.9 eV and 401.1 eV in Analyses 1, 2, and 3, respectively.

oxygen is consistent with amide bond formation. Accordingly, the higher binding energy peaks in Figure 3.3 are assigned to $-NH_3^+$ moieties in the PAH, and the peaks at lower binding energy to amide nitrogen.[49-53] The clear implication of these assignments is that the N 1s narrow scan of Figure 3.3a is not a true representation of a pristine PAH/PAA assembly. Rather, it appears to represents an assembly that has been perturbed to some degree by the measurement. SE further confirmed loss of material during XPS analysis. Indeed, after analysis, PAH/PAA films were found to be about 9 ± 2% thinner by spectroscopic ellipsometry. To the best of my knowledge, this is the first report of electron/X-ray induced damage/cross-linking of a PAH/PAA LBL assembly. Parenthetically, sample damage during XPS occurs more by photoelectrons than by X-rays.[54] In addition, It has been previously shown that sample damage to organic monolayers on silicon during XPS with a monochromatic Al Kα source is low.[55]

3.4.3. Thermal Cross-Linking of LBL Films of PAH and PAA

It has previously been shown that LBL films of PAH and PAA will thermally condense to form amide bonds with elimination of water:[42]

(1) $RNH_3^+ + R'COO^- \rightarrow R\text{-}NH\text{-}CO\text{-}R' + H_2O$

It would also be expected that cross-linked PAH/PAA assemblies would be more stable than uncross-linked assemblies. To explore this reaction, an experiment was undertaken on ca. 40 nm PAH/PAA assemblies prepared at ca. pH 5 in a star-type experimental design[56] (see Table 3.1) where three cure temperatures (150, 200, and 250 °C) and three cure times (1, 2, and 3 h) were

		Thickness (Å)		XPS O 1s/N1s Ratio	
Temperature (°C)	Time (h)	Before Cross-linking	After Cross-linking	Before	After
150	2	223.79	170.35	2.04	1.81
200	1	-	-	1.89	1.90
200	2	389.34	335.41	1.89	1.68
200	2	428.48	381.81	1.87	1.68
200	2	374.88	318.36	1.93	1.68
200	3	213.16	173.92	2.08	1.46
250	2	146.56	115.91	2.10	1.29

Table 3.1. Initial and final ellipsometric thicknesses and XPS O 1s/N 1s ratios for PAH/PAA LBL films before and after thermal treatment. Times and temperatures were chosen to conform to a star-shaped experimental design. Three replicates were performed in the center of the design (at 200 °C and 2 h). The average O1s/N 1s ratio before cross-linking was 1.97, and the standard deviation and relative standard deviation for this set of data were 0.10 and 5.00%, respectively.

considered. To the best of our knowledge, this is the widest/most complete range of temperatures and times considered for this reaction.

Figure 3.4 shows representative XPS N 1s narrow scans of the uncross-linked film (Figure 3.4a), and films heated to 150, 200, or 250 °C for 2 h (Figures 3.4b-d). The narrow scan of the uncross-linked film in Figure 3.4a agrees well with the corresponding spectrum in Figure 3.3a, despite the fact that it was taken at a different resolution setting on the instrument. However, the other three narrow scans in Figure 3.4 differ substantially from Figure 3.4a (or Figure 3.3a). In these narrow scans, the amount of signal at lower binding energy, which was attributed to amide nitrogen, increases steadily with increasing temperature. This result is consistent with the expected, thermally driven amidation of the films. After treatment at 250 °C for 2 h this process appears to be essentially complete.

As shown in Table 3.1, the O 1s/ N 1s ratios for the films follow the amidation expected from the N 1s narrow scans in Figure 3.4. That is, the film treated at 250 °C has the lowest O 1s/N 1s ratio of those studied in the experimental design, again suggesting the greatest degree of amidation at the highest cure temperature. Table 3.1 also shows that, in all cases, there is a decrease in film thickness after the thermal treatments, which is again consistent with the amidation predicted herein. Two other results of this XPS analysis are noteworthy. First, the N 1s/ C 1s ratios in the films did not change after cross-linking, indicating that nitrogen is not lost from the films either during analysis or during thermal treatments. Second, no Si 2p signal is discernable in the spectra, which suggests that (i) signals from the substrate, e.g., O 1s photoelectrons, are attenuated to the degree that they do not contribute to the analysis, and (ii) that the films are quite uniform, i.e., they contain very few pinholes or thin spots. Because of the significant amount of cross-linking

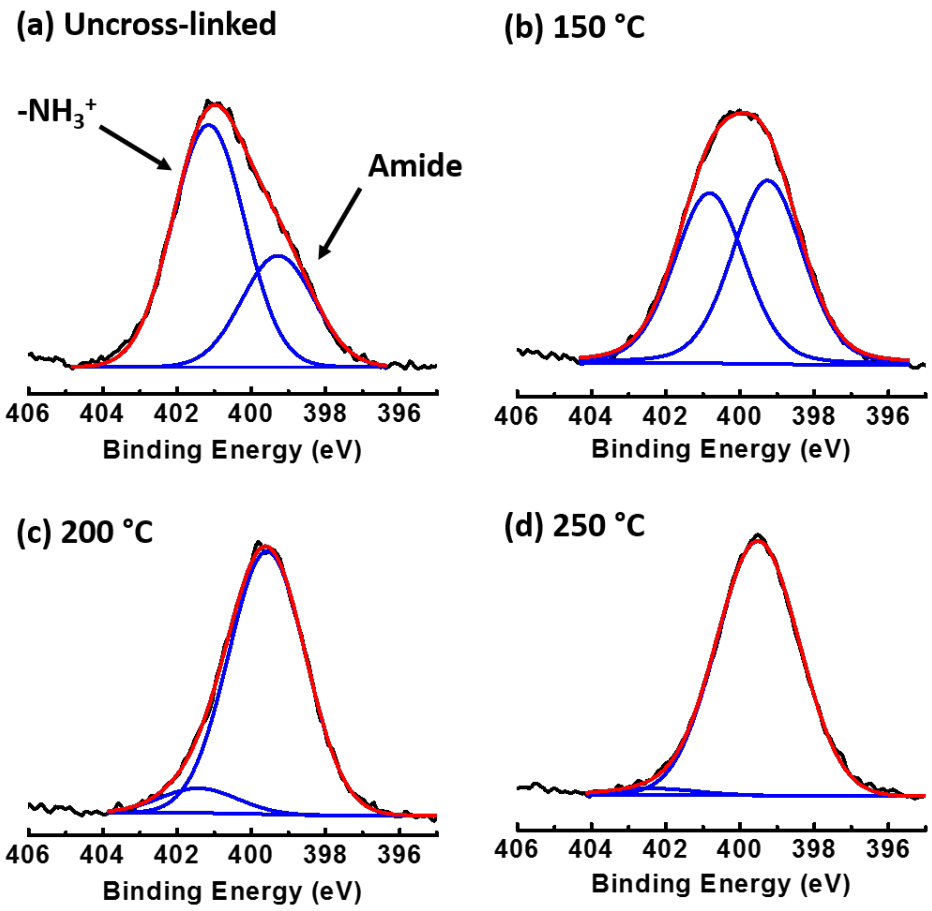

Figure 3.4. XPS N 1s narrow scans fitted with two 100% Gaussians of equal width for (a) an uncross-linked PAH/PAA LBL assembly, and (b, c, and d) PAH/PAA LBL assemblies cross-linked for 2 h at 150 °C, 200 °C, and 250 °C, respectively. The Gaussian at higher binding energy is assigned to ammonium ($-NH_3^{+}$), and the Gaussian at lower binding energy to amide, -NH-C(O)-, nitrogen. The peak positions of the '$-NH_3^{+}$' and 'Amide' signals were allowed to float in the fitting. The signals of these peaks were (a) 401.2 and 399.3, (b) 400.8 and 399.2, (c) 401.4 and 399.6, and (d) 402.4 and 399.5. These spectra were reference to the C 1s peak, which is why their peak positions are lower than those in Figure 3.3, which were not referenced.

suggested at 250 °C, all of the cross-linked assemblies described in the remainder of this chapter were heated to this temperature for at least 2 h (see Table 3.2).

3.4.4. LBL Film Stability in Solvents and at Low and High pH

Stable thin films are important in many applications, e.g., in chromatography and for hydrophobic coatings.[57-59] The stability of uncross-linked PAH/PAA LBL assemblies (final thickness ca. 70 Å – 80 Å) was first evaluated by sonicating them in water for 20 min, THF for 15 min, and ethanol for 20 min. These assemblies were completely stable under these conditions, as indicated by constant ellipsometric thicknesses (see Figure 3.5). Uncross-linked and cross-linked assemblies were then exposed to aqueous buffers under acidic (pH 1.68, 25 min) and basic (pH 10, 20 min; and pH 13, 20 min) conditions. In the low pH buffer, more than 73% of uncross-linked thin film is removed from the substrate, while the cross-linked assembly remains intact. Under elevated pH conditions (10 and 13), the uncross-linked films are almost entirely removed (less than 17% of it remains) and about half (~48%) of the cross-linked film remains. In these experiments, the same cross-linked film was used – it was first immersed in the low pH buffer and then in the high pH buffers (see Figure 3.5). In summary, cross-linking does not appear to be necessary for the assemblies to be stable in water and organic solvents, but it makes a significant difference at low and high pH. Under alkaline conditions, the observed instability may be due, at least in part, to dissolution of the underlying native SiO_2 layer as a black discoloration was observed on the sample. To the best of my knowledge, this is the first report of the stability testing of PAH/PAA assemblies in a series of solvents and at different pH values.

		Thickness (Å)	
Temperature (°C)	Time (h)	Before Cross-linking	After Cross-linking
250	2	158.10	114.31
250	2	220.55	166.93
250	3	209.59	163.65
250	3	225.92	168.70
250	3	205.81	156.08
250	3	183.01	140.98
250	3	108.57	84.98
250	3	255.61	200.39
250	3	267.70	214.00
250	3	108.41	92.44
250	3	150.18	123.16
250	2.6	66.54	28.93
250	2.6	66.29	29.61
250	3	97.10	43.32

Table 3.2. Ellipsometric thicknesses of LBL assemblies before and after thermal cross-linking at 250° C for at least for 2 h.

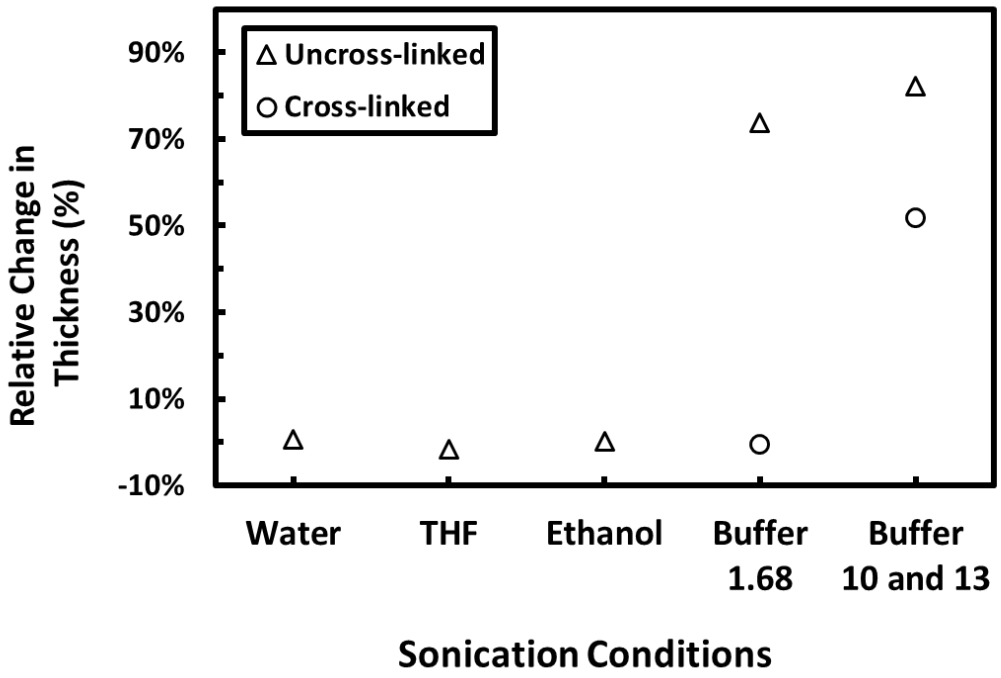

Figure 3.5. Stability of uncross-linked (triangles) and cross-linked (circles) LBL assemblies before and after sonication in water for 20 min, THF for 15 min, and ethanol for 20 min, and after exposure to aqueous buffers at pH 1.68, 10, and 13.

3.4.5. Thiol Termination of PAH-Terminated PAH/PAA LBL Assemblies

PAH-terminated LBL assemblies ought to possess unreacted amine groups at their surfaces, i.e., this should definitely be the case for uncross-linked assemblies, but even cross-linked assemblies should possess some free amine groups. Traut's reagent (2-iminothiolane) is a well-known, cyclic reagent that is frequently used in bioconjugate chemistry. It works through a ring opening mechanism to convert amine groups into thiol (-SH) moieties. The interest in –SH groups comes from the many facile reactions they undergo in thiol-ene chemistry.[25-26, 29] Here the reaction between Traut's reagent and PAH-terminated LBL assemblies was studied via XPS and SE as a function of the solution pH (5 or 8), reaction temperature (0 or 20 °C), concentration of Traut's reagent (0.001, 0.01, or 0.1 M), and degree of thermal cross-linking of the LBL assembly (cross-linked or not). The exposure time to Traut's reagent was 30 min in all cases. To the best of my knowledge, this is the first report of the direct reaction between Traut's reagent and a PAA/PAH assembly. I am, however, aware of a somewhat related study in which LBL assemblies of silica nanoparticles and poly(ethyleneimine) (PEI) were deposited onto another LBL assembly of PEI and poly(sodium 4-styrenesulfonate) (PSS). The silica nanoparticles were then functionalized with an amino silane, which in turn was reacted with Traut's reagent.[60]

It has previously been reported that Traut's reagent reacts well with primary amines at pH 7 – 9.[43-44] However, this reaction may occur with the primary amines of PAH at even lower pH values because there may still be free amine groups on the polyelectrolyte below pH 7. That is, neighboring, positively charged amino groups on PAH are expected to interact with each other and perturb (lower) each other's pK_a values.[61] Accordingly, the reaction between Traut's reagent and PAH-terminated, uncross-linked PAH/PAA assemblies was attempted at pH 5. Figure 3.6 indicates that some reaction does take place under these conditions, as measured by XPS S 2s/N

1s ratios and changes in film thickness, which correlate reasonably well. However, Figure 3.6 also shows that, as expected, the reactions run more efficiently at pH 8, even when the concentration of Traut's reagent is quite low.

The reaction of Traut's reagent with a cross-linked PAH-terminated PAH/PAA assembly was also studied (Figure 3.6). Here, some reaction again appears to take place, but to a lesser degree than for the uncross-linked films. These results are reasonable. Cross-linking is expected to decrease the number of amine groups available at the surfaces, and also decrease the ability of Traut's reagent to diffuse within the PAH/PAA assemblies, i.e., these results constitute a chemical test that is consistent with the thermal cross-linking of PAH/PAA assemblies. Finally, Figure 3.6 shows that the reaction between Traut's reagent and the PAH-terminated surfaces is more efficient at higher concentrations of Traut's reagent and with increased reaction temperature. Both of these results are consistent with the general theory of chemical reactivity. As a control, uncross-linked PAH/PAA samples were exposed to a solution without Traut's reagent at pH 8 and 20 °C. Here, SE showed a negligible change in film thickness (0.36 Å), and XPS showed an insignificant S 2s/N 1s ratio of 0.034. The best conditions found for the Traut's reagent/PAH reaction are pH 8, 20 °C, and 0.1 M, i.e., the highest pH, temperature, and concentration studied.

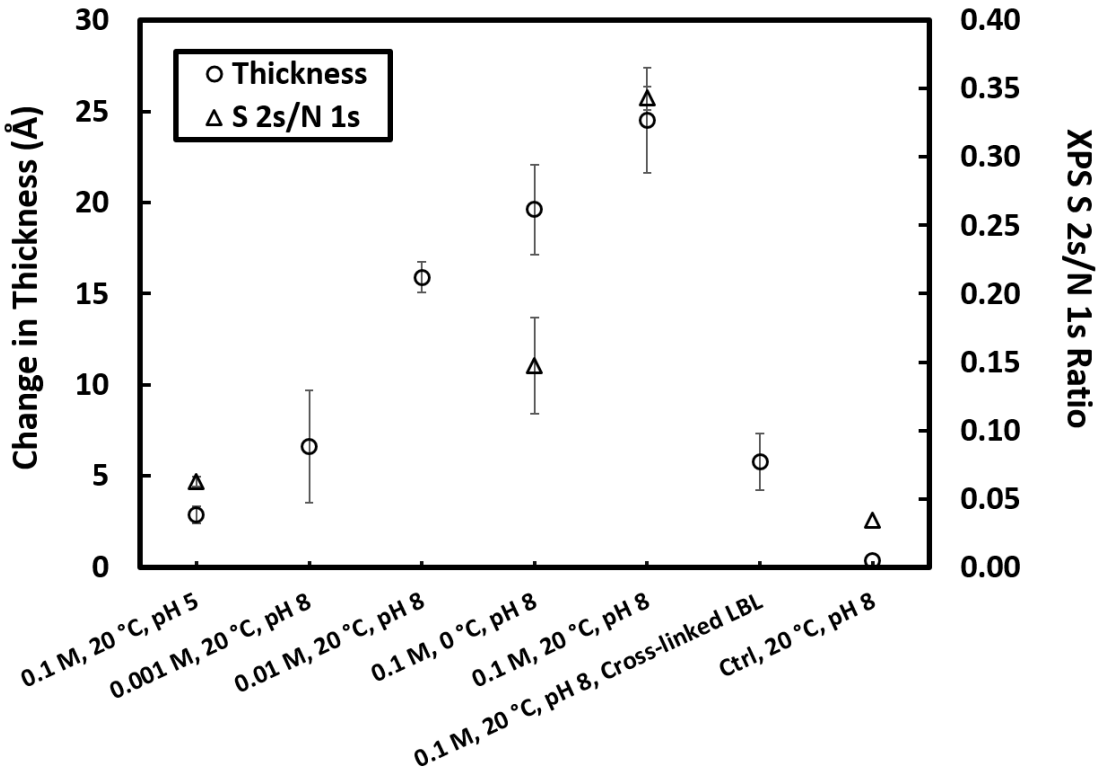

Figure 3.6. Thickness changes by ellipsometry (circles) and S 2s/N 1s ratios (triangles) for PAH-terminated PAH/PAA assemblies treated with Traut's reagent under different conditions, as indicated above. All LBL assemblies were uncross-linked, except as indicated above. All exposures were for 30 min. This XPS analysis was carried out only for the uncross-linked LBL assemblies reacted with 0.1 M Traut's reagent, as shown in this figure.

3.4.6. Analysis and Prevention of –SH Group Oxidation

Thiol terminated assemblies prepared in the previous step were carried forward to the next step for thiol-ene chemistry. However, thiol groups are prone to oxidation so it is important to ensure that they have not oxidized prior to attempting thiol-ene chemistry.[20, 25-26, 62] Understanding the stability of thiol groups would allow one to determine if thiol terminated assemblies could be stored or should be used immediately after they are prepared. This topic is considered important in bioconjugate chemistry,[20] and there has been some mention of it with regards to surfaces. For example, Halliwell and Cass[63] studied mercaptosilane-terminated surfaces.[64] They noted the possibility of thiol oxidation, and cited a private communication that suggested that oxidation of –SH groups on surfaces takes place rapidly above 115 °C, and that this process can be followed by XPS. Fierro and coworkers modified silica with a mercaptosilane and oxidized the resulting –SH groups using hydrogen peroxide.[65] There do not appear to be very many of such studies in the literature, and I am not aware of any on thiol-terminated surfaces prepared with Traut's reagent. I have also not been able to find any work related to the very important issue of the simple exposure of –SH terminated surfaces to the air under ambient conditions.

To understand their stability against oxidation, PAH/PAA LBL assemblies treated with Traut's reagent (at pH 8, 20 °C, and 0.1 M) were exposed to the air (and light) for 24 or 48 h and then analyzed by XPS. Changes in the S 2s/N 1s ratio were used to determine any loss of sulfur from the surfaces, which did occur and can be attributed to oxidation of thiol groups. Peak fitting of the S 2s envelope was used to assay any changes in the oxidation state of the remaining sulfur. The S 2s peak was used in this analysis instead of the more intense S 2p peak (i) to avoid any possible overlap of the S 2p (160-169 eV) region with the Si 2s (155-165 eV) signal from the substrate,[66] and (ii) because it appears as a simpler, single peak, and not a spin-orbit doublet. Peak

fitting was performed with three 80:20 Gaussian-Lorentzian peaks constrained to have equal widths (see Figure 3.7a-c).

After exposure to the air, both a loss of sulfur from the surfaces and a change in the chemical state of the remaining sulfur were observed. Based on decreasing S 2s/N 1s ratios, 15% of the sulfur was lost after the first exposure to air, and 36% after the second. To assay the chemical state of sulfur in/on the assemblies after these stability tests, the XPS S 2s signals from the surfaces were fit to three Gaussian-Lorentzians of equal width that were allowed to float in position (see Figure 3.7). The result of this exercise was three peaks at nearly the same binding energy (231.5 ± 0.2 eV) that were assigned to oxidized sulfur, three peaks at nearly the same binding energy that were assigned to thiol (-SH) groups (227.6 ± 0.1 eV), and three peaks at nearly the same binding energy that were assigned to thiolate ($-S^-$) groups (225.4 ± 0.4 eV).[66] The standard deviation for the thiolate measurement is larger because of the uncertainty associated with the position of the very small thiolate signal in the 48 h sample in Figure 3.7C (the peak positions of the thiolate signals for Figures 3.7A and 3.5B were both 225.7 eV). Based on the peak areas from this fitting exercise, the fraction of thiolate groups on the surfaces decreased from 26% to 7% after 24 h of exposure to the laboratory environment and finally to 3% after 48 h of exposure. The fraction of thiol groups at the surfaces also decreased: from 55% to 43% after 24 h and finally to 36% after 48 h of air exposure. Finally, the fraction of sulfur in an oxidized state increased from 19% initially to 50% after 24 h, and finally to 61% after 48 h. These results indicate that thiolate groups on PAA/PAH assemblies are more prone to oxidation than thiols, but that the thiols also oxidize to a significant extent. Both of these results are chemically reasonable. Thus, to avoid degradation of the reduced sulfur species (thiols and thiolates) at the surface, PAA/PAH assemblies treated with Traut's reagent were used immediately after their preparation.

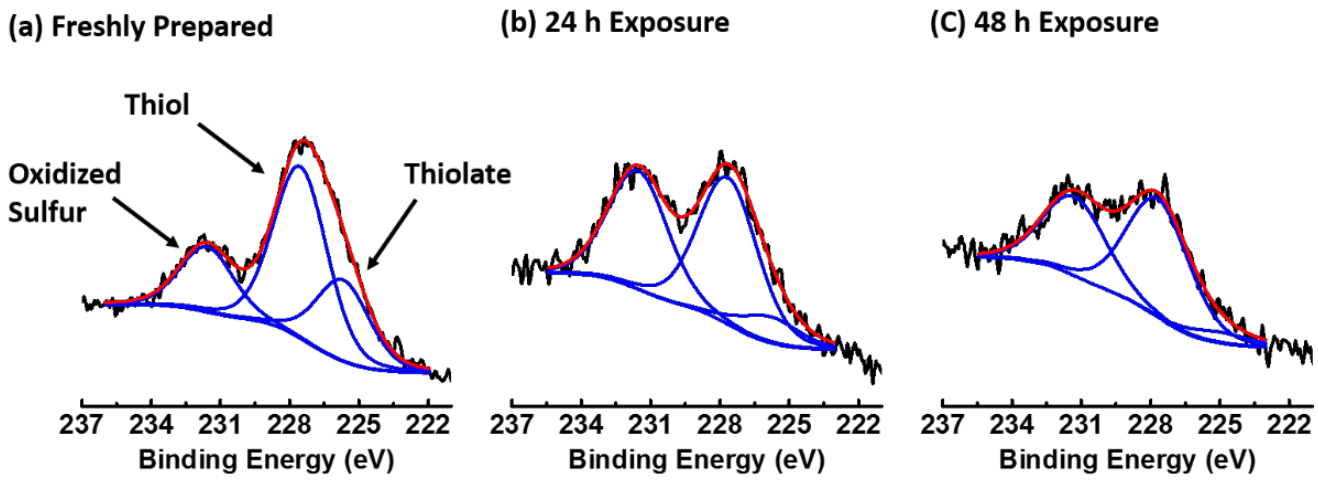

Figure 3.7. XPS S 2s narrow scans of thiol-terminated samples before and after 24 h and 48 h exposures to air and light. The S 2s peak is fitted with three 80:20 Gaussian:Lorentzian peaks of equal width. The peaks are designated as oxidized sulfur, thiol (-SH), or thiolate ($-S^-$).

3.4.7. Rinsing of Thiol Terminated Assemblies with Acetic Acid

The –SH moiety is expected to be more stable in air than the $–S^-$ group. In addition, simple acid-base chemistry suggests that rinsing an –SH/$–S^-$ surface with an acid should convert the $–S^-$ groups into –SH moieties. Accordingly, PAH/PAA assemblies reacted with Traut's reagent were rinsed with 0.1 M acetic acid for 30 s or 60 s, or immersed in the solution for 5 min (see Figure 3.8). In all three cases, the fraction of thiolate groups at the surfaces dropped from 26% to 11-13%, and at the same time, the fraction of –SH groups increased from 55-57% to 66-67%. Concomitant with these reactions, the amount of oxidized sulfur on these surfaces also increased by a relatively small amount: from 17-19% to 20-23%. The XPS S 2s/N 1s ratios for these surfaces remained essentially constant, indicating that this process did not remove sulfur from the surfaces. Ultimately, because a polymeric reagent with multiple attachment points was reacted with the –SH terminated surfaces, this added rinsing step was not employed before thiol-ene chemistry was performed.

3.4.8. Thiol-Ene Attachment of 1,2-Polybutadiene to –SH Terminated Assemblies

Cross-linked LBL assemblies terminated with –SH groups from Traut's reagent were reacted with different concentrations of 1,2-polybutadiene (PBd) in THF (12.5% – 25% w/v) for different amounts of time (~6 to ~11 h). These experiments were performed under irradiation of 254 nm UV light in an inert (N_2) atmosphere. The chemisorption of 1,2-PBd was confirmed by sessile water contact angles (20 μL water drops) and by SE film thickness measurements. Figure 3.9 reveals that low exposures of UV light and/or low concentrations of PBd lead to rather thin films of adsorbed PBd (< 10 Å) with contact angles below 100°. Higher concentrations (~25%) of

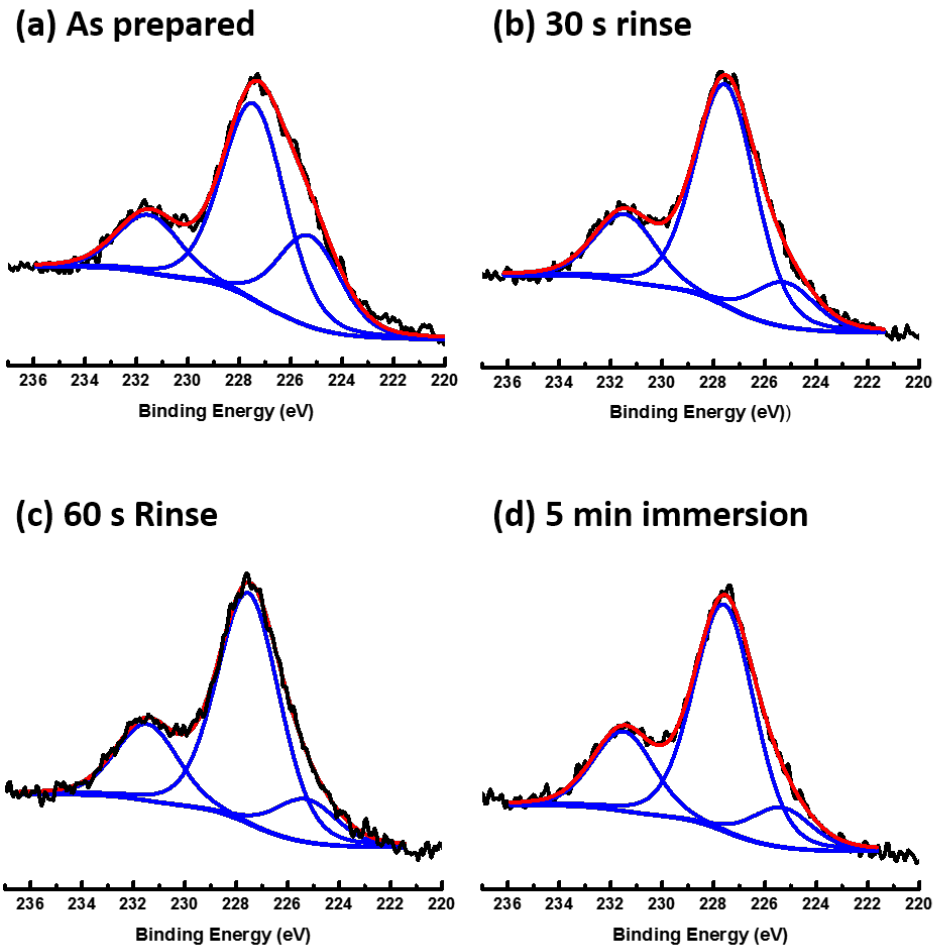

Figure 3.8. XPS 2s narrow scans of –SH terminated assemblies before and after rinsing with dilute (0.1 M) acetic acid for varying amounts of time.

the polymer and/or longer exposure times typically produced 5 – 8 nm films with water contact angles above 100°. For comparison, an uncross-linked assembly terminated with –SH groups was also reacted (four days after its preparation) with a more concentrated solution of PBd in THF (50% w/v), see data points with the asterisk (*) in Figure 3.9. This reaction was carried out with 254 nm UV light without a blanket of N_2. Under these conditions, the thiol groups would be expected to oxidize readily. That is, the smaller number of attachment points that are expected here is consistent with the lower film thickness obtained. Nevertheless, attachment of PBd was successful on both cross-linked and uncross-linked films, whether in the air or not, presumably because the polymers are large and do not require a high density of attachment points.

3.4.9. Thiol-ene Attachment of Perfluorodecanethiol to PBd Terminated Assemblies

The PBd-terminated assemblies described in the previous section underwent a second thiol-ene reaction with neat perfluorordecanethiol (PDT). Reaction times were 4, 5, 8, and 12 h under 254 nm UV light and a blanket of N_2. Increases in film thickness of ~4 Å and water contact angles of ca. 120° were observed for the 4 – 8 h exposures on cross-linked and uncross-linked LBL assemblies terminated with PBd (see Figure 3.10). One cross-linked assembly showed much higher thickness of PDT layer ~ 12.75 Å. I am not completely comfortable removing this data point as an outlier because of the difficulty in controlling this chemistry. The high water contact angles obtained at these moderate UV exposures suggest that a large number of sites (carbon-carbon double bonds) are available on adsorbed PBd for binding to a thiol. However, after 12 h of UV exposure, the film was catastrophically damaged. This suggests that the long exposures of the films to UV light could damage the films, decreasing their thicknesses and leaving them

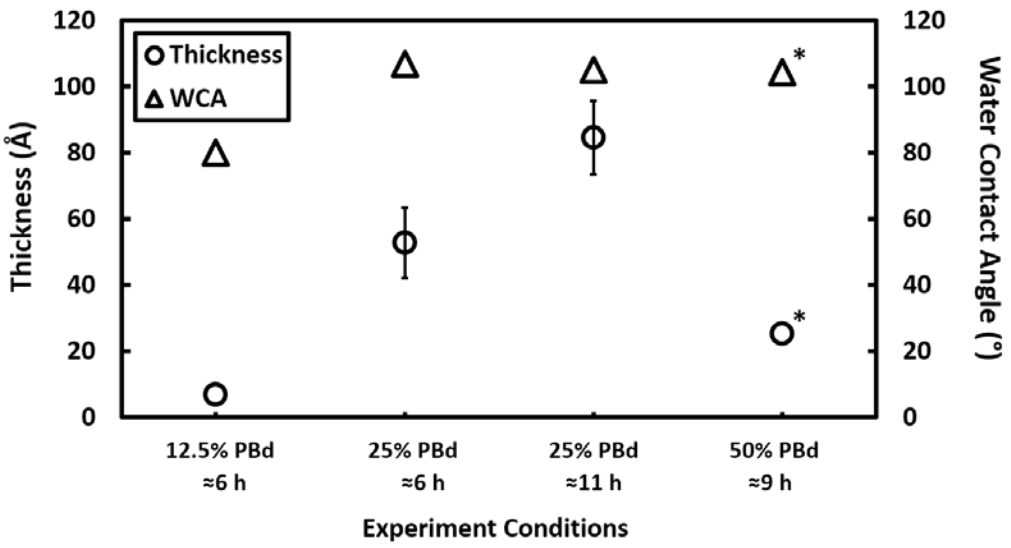

Figure 3.9. Ellipsometric thicknesses and water contact angles after reaction of –SH terminated cross-linked with 1,2-polybutadiene (PBd) under different experimental conditions. The data points marked with '*' are for –SH terminated uncross-linked assemblies reacted in air instead of inert atmosphere.

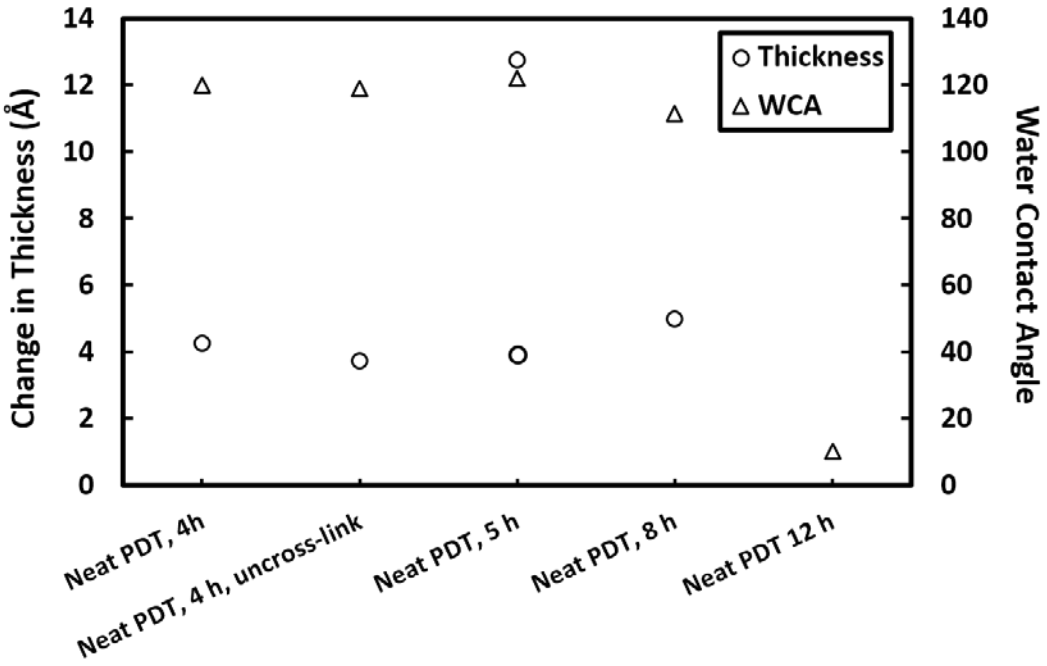

Figure 3.10. Ellipsometric thicknesses and water contact angles of PBd coated surfaces reacted with perfluorordecanethiol (PDT) under different experimental conditions.

hydrophilic. Obviously, these results also imply that some damage to the assemblies is always taking place. That is, the ability of PBd and PDT to impart hydrophobicity and stability (vide infra) appear to outweigh any film damage at lower exposures.

3.4.10. Stability of Hydrophobic Assemblies, Including Prevention of Film Delamination by Substrate Silanization

As an additional stability test, the cross-linked, hydrophobic surfaces prepared with PBd and the perfluorordecanethiol described above were floated upside down on the surface of water for an extended period of time. After ca. seven days, the hydrophobic layers delaminated from their silicon substrates to produce free-standing films. I hypothesized that delamination was due to a lack of covalent bonds between the film and the substrate. Accordingly, a thin layer (1 – 2 nm) of a silane coupling agent,[67] 3-aminopropyltriethoxysilane (APTES),[6] was deposited on the substrates. The LBL of PAA and PAH was then performed as before, followed by depositions of Traut's reagent, PBd, and PDT. This tethered layer did not delaminate when floated upside down in water for 9 days in water. The same sample was then floated upside down in an acidic buffer (pH 1.68) for 30 days. No delamination occurred. Periodically, during this 30-day stability test, the surface was removed, rinsed, dried, and characterized by ellipsometry and wetting. Essentially no change in its thickness occurred during this time, although its water contact angle decreased modestly from 122° to 112°. However, the original contact angle could be recovered simply by drying the sample for 1 – 2 h at 70 °C.

The stabilities of complete hydrophobic assembles tethered through APTES were also tested by swabbing with ethanol and by the Scotch tape test. For the ethanol swabs, a sponge was dipped in ethanol and then gently rubbed across the surface of the film. In the Scotch tape test, a

piece of Scotch tape was pressed against the sample surface and then pulled off, where this test was performed multiple times on the same sample. In neither case was any change in water contact angle or ellipsometric thickness observed.

3.4.11. Controlling Surface Wetting with Cross-Linking

Complete, hydrophobic molecular assemblies were prepared as described above, but only a fraction of them were cross-linked. The final water contact angles (20 μL drops) were ~120° for both surfaces. However, test water droplets were pinned very strongly to the uncross-linked surfaces, e.g., droplets did not move when the samples were turned upside down. On the other hand, the water droplets rolled off the cross-linked surfaces when they had a critical volume of 30 μL and were at a tilt angle of 70°. For volumes less than 30 μL, no roll off was observed. These results suggest that there is an opportunity to control the pinning of water droplets through the extent of thermal cross-linking.

3.5. Conclusion

A complex molecular assembly was prepared on a silicon surface using a combination of thermally cross-linked polyelectrolyte multilayers, bioconjugate chemistry with Traut's reagent (2-iminothiolane), and thiol-ene chemistry with polybutadiene and fluorinated thioalkane. The LBL process was explored at two pH values. The assemblies were studied at each step of the surface modification process. For example, the growth rate of the LBL assemblies, as monitored by SE, became exponential for large number of layers, damage to the materials during XPS analysis was observed and studied, and the oxidation of thiol-terminated assemblies exposed to the air was carefully monitored by XPS. The final assemblies showed good hydrophobic properties

(WCA 120°), which could be tuned by the changing the extent of thermal cross-linking. Hydrophobic assemblies held to the substrate through a silane coupling agent showed good stability when immersed in an acidic (pH 1.68) solution for 30 days. They also resisted rubbing with ethanol swabs, and the Scotch tape test.

3.6. References

1. Gooding, J. J.; Ciampi, S. *Chem. Soc. Rev.* **2011,** *40* (5), 2704-2718.

2. Allara, D. L.; Nuzzo, R. G. *Langmuir* **1985,** *1*, 45-52.

3. Carey, R. I.; Folkers, J. P.; Whitesides, G. M. *Langmuir* **1994**, 10 (7), 2228-2234.

4. Offord, D. A.; John, C. M.; Linford, M. R.; Griffin, J. H. *Langmuir* **1994**, 10, 883-889.

5. Offord, D. A.; John, C. M.; Griffin, J. H. *Langmuir* **1994**, 10 (3), 761-766.

6. Zhang, F.; Sautter, K.; Larsen, A. M.; Findley, D. A.; Davis, R. C.; Samha, H.; Linford, M. R. *Langmuir* **2010,** *26* (18), 14648-14654.

7. Barness, Y.; Gershevitz, O.; Sekar, M.; Sukenik, C. N. *Langmuir* **2000,** *16* (1), 247-251.

8. Gun, J.; Iscovici, R.; Sagiv, J. *J. Colloid Interface Sci.* **1984,** *101* (1), 201-213.

9. Pomerantz, M.; Segmüller, A.; Netzer, L.; Sagiv, J. *Thin Solid Films* **1985,** *132* (1), 153-162.

10. Linford, M. R.; Fenter, P.; Eisenberger, P. M.; Chidsey, C. E. D. *J. Am. Chem. Soc.* **1995,** *117*, 3145-3155.

11. Manova, R.; van Beek, T. A.; Zuilhof, H. *Angew. Chem., Int. Ed.* **2011,** *50* (24), 5428-5430.

12. Wagner, P.; Nock, S.; Spudich, J. A.; Volkmuth, W. D.; Chu, S.; Cicero, R. L.; Wade, C. P.; Linford, M. R.; Chidsey, C. E. D. *J. Struct. Biol.* **1997,** *119*, 189-201.

13. Sieval, A. B.; Demirel, A. L.; Nissink, J. W. M.; Linford, M. R.; van der Maas, J. H.; de Jeu, W. H.; Zuilhof, H.; Sudhölter, E. J. R. *Langmuir* **1998,** *14* (7), 1759-1768.

14. Linford, M. R.; Chidsey, C. E. D. *Langmuir* **2002,** *18*, 6217-6221.

15. Huck, L. A.; Buriak, J. M. *Langmuir* **2012,** *28* (47), 16285-16293.

16. Attavar, S.; Diwekar, M.; Linford, M. R.; Davis, M. A.; Blair, S. *Appl. Surf. Sci.* **2010,** *256* (23), 7146-7150.

17. Yang, H. C.; Aoki, K.; Hong, H. G.; Sackett, D. D.; Arendt, M. F.; Yau, S. L.; Bell, C. M.; Mallouk, T. E. *J.Am.Chem.Soc.* **1993,** *115* (25), 11855-11862.

18. Aoki, K.; Brousseau, L. C.; Mallouk, T. E. *Sens. Actuators, B* **1993,** *14* (1-3), 703-704.

19. Hong, H. G.; Sackett, D. D.; Mallouk, T. E. *Chem.Mater.* **1991,** *3* (3), 521-527.

20. Hermanson, G. T., *Bioconjugate techniques*. 3rd ed.; Academic press: 2013.

21. Schütte, M.; Kurth, D. G.; Linford, M. R.; Cölfen, H.; Möhwald, H. *Angew. Chem., Int. Ed.* **1998,** *37* (20), 2891-2893.

22. Linford, M. R.; Auch, M.; Möhwald, H. *J. Am. Chem. Soc.* **1998,** *120*, 178-182.

23. Caruso, F.; Trau, D.; Möhwald, H.; Renneberg, R. *Langmuir* **2000,** *16* (4), 1485-1488.

24. Lvov, Y.; Decher, G.; Möhwald, H. *Langmuir* **1993,** *9*, 481-486.

25. Madaan, N.; Terry, A.; Harb, J.; Davis, R. C.; Schlaad, H.; Linford, M. R. *J. Phys. Chem. C* **2011,** *115* (46), 22931-22938.

26. Bertin, A.; Schlaad, H. *Chem. Mater.* **2009,** *21* (24), 5698-5700.

27. Brummelhuis, N. T.; Diehl, C.; Schlaad, H. *Macromolecules* **2008,** *41*, 9946-9947.

28. Justynska, J.; Hordyjewicz, Z.; Schlaad, H. *Polymer* **2005,** *46* (26), 12057-12064.

29. Wickard, T. D.; Nelsen, E.; Madaan, N.; ten Brummelhuis, N.; Diehl, C.; Schlaad, H.; Davis, R. C.; Linford, M. R. *Langmuir* **2009,** *26* (3), 1923-1928.

30. Song, J.; Jensen, D. S.; Hutchison, D. N.; Turner, B.; Wood, T.; Dadson, A.; Vail, M. A.; Linford, M. R.; Vanfleet, R. R.; Davis, R. C. *Adv. Funct. Mater.* **2011,** *21* (6), 1132-1139.

31. Jensen, D. S.; Kanyal, S. S.; Gupta, V.; Vail, M. A.; Dadson, A. E.; Engelhard, M.; Vanfleet, R.; Davis, R. C.; Linford, M. R. *J. Chromatogr. A* **2012,** *1257* (0), 195-203.

32. Fan, S.; Chapline, M. G.; Franklin, N. R.; Tombler, T. W.; Cassell, A. M.; Dai, H. *Science* **1999,** *283* (5401), 512-514.

33. Tour, J. M. *Acc. Chem. Res.* **2000,** *33* (11), 791-804.

34. Low, P. J. *Dalton Trans.* **2005,** (17), 2821-2824.

35. Chen, X.; Jeon, Y.-M.; Jang, J.-W.; Qin, L.; Huo, F.; Wei, W.; Mirkin, C. A. *J. Am. Chem. Soc.* **2008,** *130* (26), 8166-8168.

36. Pearson, A. C.; Linford, M. R.; Harb, J. N.; Davis, R. C. *Langmuir* **2013,** *29* (24), 7433-7438.

37. Pearson, A. C.; Pound, E.; Woolley, A. T.; Linford, M. R.; Harb, J. N.; Davis, R. C. *Nano Lett.* **2011,** *11* (5), 1981-1987.

38. Zhai, L.; Berg, M. C.; Cebeci, F. C.; Kim, Y.; Milwid, J. M.; Rubner, M. F.; Cohen, R. E. *Nano Lett.* **2006,** *6* (6), 1213-1217.

39. Zhai, L.; Cebeci, F. Ç.; Cohen, R. E.; Rubner, M. F. *Nano Lett.* **2004,** *4* (7), 1349-1353.

40. Wood, K. C.; Chuang, H. F.; Batten, R. D.; Lynn, D. M.; Hammond, P. T. *Proceedings of the National Academy of Sciences* **2006,** *103* (27), 10207-10212.

41. Bračko, I.; Jančar, B.; Logar, M.; Caglič, D.; Suvorov, D. *Nanotechnology* **2011,** *22* (8), 085705.

42. Harris, J. J.; DeRose, P. M.; Bruening, M. L. *J. Am. Chem. Soc.* **1999,** *121* (9), 1978-1979.

43. Traut, R. R.; Bollen, A.; Sun, T.-T.; Hershey, J. W.; Sundberg, J.; Pierce, L. R. *Biochemistry* **1973,** *12* (17), 3266-3273.

44. Jue, R.; Lambert, J. M.; Pierce, L. R.; Traut, R. R. *Biochemistry* **1978,** *17* (25), 5399-5406.

45. Gupta, V.; Ganegoda, H.; Engelhard, M. H.; Terry, J.; Linford, M. R. *J. Chem. Educ.* **2013,** *91* (2), 232-238.

46. Kim, T.-H.; Sohn, B.-H. *Appl. Surf. Sci.* **2002,** *201* (1), 109-114.

47. Crist, B. V. *J. Surf. Anal* **1998,** *4* (3), 428-34.

48. Linford, M. R. *Vacuum & Coating Technology* July, 2014, pp 27-34.

49. Polzonetti, G.; Battocchio, C.; Iucci, G.; Dettin, M.; Gambaretto, R.; Di Bello, C.; Carravetta, V. *Materials Science and Engineering: C* **2006,** *26* (5–7), 929-934.

50. Graf, N.; Yegen, E.; Gross, T.; Lippitz, A.; Weigel, W.; Krakert, S.; Terfort, A.; Unger, W. E. S. *Surf. Sci.* **2009,** *603* (18), 2849-2860.

51. Perruchot, C.; Khan, M. A.; Kamitsi, A.; Armes, S. P.; Watts, J. F.; von Werne, T.; Patten, T. E. *Eur. Polym. J.* **2004,** *40* (9), 2129-2141.

52. An, Y.; Chen, M.; Xue, Q.; Liu, W. *J. Colloid Interface Sci.* **2007,** *311* (2), 507-513.

53. Wu, J.; Zhang, L.; Wang, Y.; Long, Y.; Gao, H.; Zhang, X.; Zhao, N.; Cai, Y.; Xu, J. *Langmuir* **2011,** *27* (22), 13684-13691.

54. Heister, K.; Zharnikov, M.; Grunze, M.; Johansson, L.; Ulman, A. *Langmuir* **2001,** *17* (1), 8-11.

55. Jiang, G.; Niederhauser, T. L.; Davis, S. D.; Lua, Y.-Y.; Cannon, B. R.; Dorff, M. J.; Howell, L. L.; Magleby, S. P.; Linford, M. R. *Colloid Surface A* **2003,** *226* (1-3), 9-16.

56. Brereton, R. G., *Chemometrics. Data Analysis for the Laboratory and Chemical Plant.* John Wiley & Sons: 2003.

57. Saini, G.; Jensen, D. S.; Wiest, L. A.; Vail, M. A.; Dadson, A.; Lee, M. L.; Shutthanandan, V.; Linford, M. R. *Anal. Chem.* **2010,** *82* (11), 4448-4456.

58. Wiest, L. A.; Jensen, D. S.; Hung, C.-H.; Olsen, R. E.; Davis, R. C.; Vail, M. A.; Dadson, A. E.; Nesterenko, P. N. *Anal. Chem.* **2011,** *83* (14), 5488-5501.

59. Saini, G.; Sautter, K.; Hild, F. E.; Pauley, J.; Linford, M. R. *J. Vac. Sci. Technol. A* **2008,** *26* (5), 1224-1234.

60. Wilson, R.; Mehrabi, M.; Prior, I. A.; Beckett, A.; Hutchinson, A. *Chem. Commun.* **2009,** (18), 2487-2489.

61. Pizem, H.; Sukenik, C. N.; Sampathkumaran, U.; McIlwain, A. K.; De Guire, M. R. *Chem. Mater.* **2002,** *14* (6), 2476-2485.

62. Jonkheijm, P.; Weinrich, D.; Köhn, M.; Engelkamp, H.; Christianen, P. C. M.; Kuhlmann, J.; Maan, J. C.; Nüsse, D.; Schroeder, H.; Wacker, R.; Breinbauer, R.; Niemeyer, C. M. *Angew. Chem. Int. Ed.* **2008,** *47* (23), 4421-4424.

63. Halliwell, C. M.; Cass, A. E. *Anal. Chem.* **2001,** *73* (11), 2476-2483.

64. Quast, A. D.; Zhang, F.; Linford, M. R.; Patterson, J. E. *Appl. Spectrosc.* **2011,** *65* (6), 634-641.

65. Cano-Serrano, E.; Campos-Martin, J.; Fierro, J. *Chem. Commun.* **2003,** (2), 246-247.

66. Bukhtiyarova, G. A.; Bukhtiyarov, V. I.; Sakaeva, N. S.; Kaichev, V. V.; Zolotovskii, B. P. *J. Mol. Catal. A: Chem.* **2000,** *158* (1), 251-255.

67. Plueddemann, E. P., *Silane Coupling Agents*. Plenum Press: New York, 1991.

Chapter 4: Fluorine Plasma Treatment of Bare and Nitrilotris(methylene) triphosphonic acid (NP) Protected Aluminum. An XPS and ToF-SIMS Study.

4.1. Abstract

Nitrilotris(methylene)triphosphonic acid (NP) is a technologically important molecule that has been used for years as a corrosion inhibitor and/or adhesion promoter on aluminum and other metal surfaces. However, to best of my knowledge, the detailed surface characterization of NP adsorbed on aluminum, or on any other surface, has not been reported. The primary motivation for this work originated as an effort to identify the cause of corrosion driven structural damage on NP coated, aluminum-based devices that were treated with a fluorinated plasma as a part of their fabrication process. Herein I report an X-ray photoelectron spectroscopy (XPS) and time-of-flight secondary ion mass spectrometry (ToF-SIMS) analysis of a series of untreated and NP-coated aluminum substrates that were exposed to the downstream products of a fluoroalkane + oxygen plasma for different amounts of time (from 0 s to 20 s), where NP forms a protective/passivation layer on aluminum. As indicated by P 2p, N 1s, Al 2p, O 1s, and F 1s narrow scans, even a 4 s plasma treatment significantly damages the NP protective layer and converts the native aluminum oxide into aluminum oxyfluoride. Heat treatment of the fluorine plasma-treated samples in the air substantially converts the aluminum oxyfluoride back to aluminum oxide, while similar heating under vacuum results in little change to the materials. A slow loss of fluorine from the samples

occurs over the course of weeks when they are stored in the air. A ToF-SIMS analysis reveals sets of signals that are consistent with no surface treatment, NP treatment, or fluorine plasma treatment. A principal components analysis of the negative ion ToF-SIMS spectra from the samples shows the expected differentiation of the samples.

4.2. Introduction

Fluorinated aluminum and alumina find applications in optics, deep ultraviolet and vacuum ultraviolet mirrors, lithography, corrosion resistant coatings, microfabrication, electronics, and catalysis.[1-4] Accordingly, the structures, properties, and behaviors of these materials have been studied as both nanoparticles and surface coatings. Interestingly, some of these applications require controlled fluorination, while in others the removal of fluorine is desirable. For example, fluorination of alumina has been reported to enhance its catalytic activity in isomerization, alkylation, and halogen exchange reactions.[2] The combination of AlF_3, LaF_3, and Al_2O_3 has demonstrated ca. 98% UV reflectivity without manifesting UV induced damage, where such materials are of interest in 193 nm lithographic systems.[5] Fluoride doping of alumina leads to a favorable lowering of its phase transition temperature to that of corundum.[6] In electronics, aluminum oxyfluoride features created on Al-1% Si bond pads by exposure to a $CF_4 + O_2$ plasma show decreased device performance (faster corrosion) so the removal of fluorine in them is desirable.[7-9] In another example, aluminum fluoride was formed on the walls of an aluminum plasma chamber.[10] This layer needed to be regularly removed to ensure a reproducible plasma process. In this case, a $SiCl_4 + Cl_2$ plasma was run in the chamber to reactively etch the aluminum fluoride and form volatile SiF_4 and $AlCl_3$.[11] Aluminum fluoride has high solubility in water, and this property has been exploited to form sharper aluminum features in photolithography; the

residual resist on the side walls of aluminum features has been removed by treating the surface with a fluorinated plasma followed by a water rinse.[12] The creation of aluminum fluoride and/or aluminum oxyfluoride can be achieved by treatment with hydrofluoric acid,[6] by passing fluorinated alkanes over alumina/aluminum at high temperature,[13] or by exposure of aluminum/alumina to a fluorine-containing plasma, e.g., SF_6, $CF_4 + O_2$, NF_3, and fluoroalkanes.[8, 14]

For monolayer and/or ultrathin film deposition on many metal oxides, organophosphonic acids are important alternatives to the well-studied organosilanes. Organophosphonic acid monolayers can be prepared on a variety of hydroxylated surfaces, including the oxides of Al, Zr, Cu, Fe, Si, Ti and ITO.[15-20] In general, these monolayers are more stable than comparable silane monolayers at elevated pH. For example, Pujari and coworkers showed that monolayers of hexadecylphosphonic acid were chemically more robust in water, and at pH 3 and pH 11, than monolayers of octadecyltrichlorosilane on plasma activated CrN.[21] It is also typically the case that organophosphonates are easier to handle than silanes. In comparison to alkoxy- or chlorosilanes, phosphonic acids do not produce a toxic byproduct upon hydrolysis, e.g., HCl, or require anhydrous conditions for deposition.[22] Phosphonic acids adsorb strongly to the native aluminum oxide layer on aluminum substrates.[23, 24] In this regard, nitrilotris(methylene)triphosphonic acid (NP) (see Figure 4.1) is an interesting molecule because it possess three phosphonate groups that bond to native alumina on aluminum to give a very thin corrosion protective layer for aluminum substrates.[25-27] However, while NP has been used for many years for corrosion protection of aluminum oxide and in other applications of technological importance, I am unaware of any detailed surface analysis by X-ray photoelectron spectroscopy (XPS) and/or time-of-flight secondary ion mass spectrometry (ToF-SIMS) of NP adsorbed on a surface.

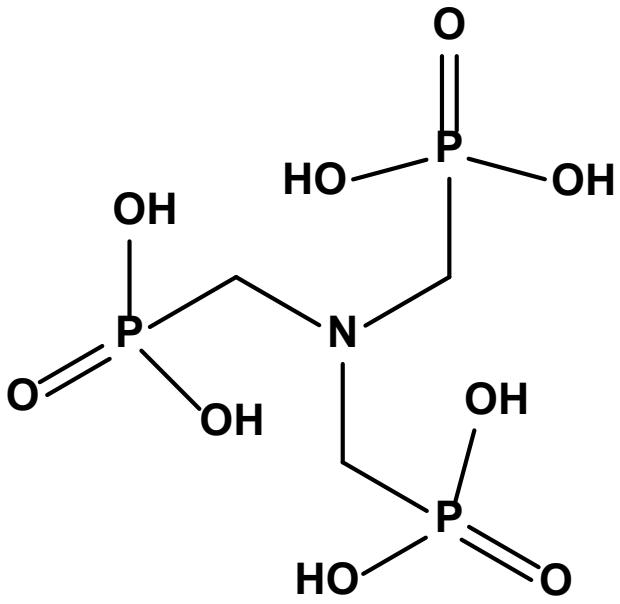

Figure 4.1. Structure of nitrilotris(methylene)triphosphonic acid (NP).

The primary motivation for this work originated from an observation that NP coated aluminum-based commercial devices when exposed to weak downstream fluoroalkane + oxygen plasma demonstrated initial improvement in their performance but later suffered corrosion driven structural damage while sitting in storage that rendered them useless. The immediate aim was to identify, understand, and if possible find a solution to this corrosion problem. Here I report an XPS and ToF-SIMS analysis of untreated and NP coated aluminum surfaces[28] that were exposed for different amounts of time to the products of a fluoroalkane + oxygen plasma. As noted, NP adsorbs to native aluminum oxide through its phosphonate groups to form a corrosion inhibiting layer.[25, 29] XPS was of central importance in this work because (i) it is non-destructive in nature, (ii) its data interpretation is relatively straightforward, (iii) it gives quantitative compositions from the upper ca. 10 nm of materials, and (iv) it informs regarding the chemical environment (oxidation states) of elements vis-à-vis chemical shifts.[30] XPS confirmed NP adsorption to the aluminum surfaces. It further showed that the fluorine plasma caused significant sample damage/modification. The hot/cold stage on the ToF-SIMS instrument allowed to demonstrate that fluorine removal does not take place from samples when they are heated under vacuum, while fluorine removal does take place readily in the air at 150-300 °C. A chemometric, principal components analysis (PCA)[31-33] of the negative ion ToF-SIMS data differentiated the samples according to their expected chemistries. PCA is an appropriate statistical analysis tool for comparing series of SIMS spectra because of the high degree of correlation that exists between the signals within them. That is, while the spectra typically possess many peaks, their inherent dimensionality is often low.[34] The effects of rinsing fluorine plasma-treated samples with ultrapure water, and the slow loss of fluorine that occurs from samples when they are stored in the air is also described.

4.3. Experimental

4.3.1. Samples

Uncoated samples consisted of transparent glass substrates sputter coated with ca. 200 nm of aluminum with/without exposure to the downstream products of a $CF_4 + O_2$ plasma for 8 seconds. These samples are designated 'Al – 0 s' and 'Al – 8 s', respectively. NP-coated samples consisted of the same ca. 200 nm of Al on glass that were treated with an aqueous solution of NP and then exposed to the $CF_4 + O_2$ plasma for 0, 4, 8, 12, 16, or 20 s. These samples are referred to as 'NP – 0 s', 'NP – 4 s', 'NP – 8 s', 'NP – 12 s', 'NP – 16 s', and 'NP – 20 s', respectively.

4.3.2. X-ray Photoelectron Spectroscopy

An SSX-100 X-ray photoelectron spectrometer equipped with a monochromatic Al Kα source (1486.6 eV) was used for the XPS analyses. Accordingly, survey (broad) scans and narrow scans for phosphorus (P 2p), nitrogen (N 1s), aluminum (Al 2p), fluorine (F 1s), oxygen (O 1s), and carbon (C 1s) were collected with an 800 μm spot size at resolution 4. An electron flood gun for charge compensation was not used because a gold-coated holding clip acted as a conductive path between aluminum on the samples and a grounded XPS sample stage. The spectra were referenced to the Al 2p signal taken at 73.00 eV for metallic aluminum. A Shirley background[35] was removed from the spectra for the determination of peak areas of narrow scans. To compare samples, peak area ratios with respect to the Al 2p peak were used: P 2p/Al 2p, N 1s/Al 2p, F 1s/Al 2p, O 1s/Al 2p, and C 1s/Al 2p. The area of the entire Al 2p signal envelope – from both the metallic and oxidized aluminum – was used to calculate these ratios. XPS was performed three times on the samples. The time gap between these analyses was approximately one week and the

samples were stored in the air in our laboratory between analyses. That is, the 'Week 1' analysis was performed two days after the samples were prepared. The 'Week 2' and 'Week 3' samples were then analyzed approximately two weeks and three weeks after the 'Week 1' analysis was performed. For each analysis, a different sample from the same batch of samples was used.

4.3.3. Time-of-flight Secondary Ion Mass Spectrometry (ToF-SIMS)

ToF-SIMS was performed with an ION-TOF (Münster, Germany) ToF-SIMS IV system equipped with a 25 KeV $^{69}Ga^{+}$ primary ion source and an in situ hot/cold stage. Although the films are on insulating glass substrates, no flood gun was necessary as the metallic layers were grounded through a top contact to the sample holder. The pulsed primary ion (target) current was typically ca. 0.36 pA. A short analysis time of 100 s and a large analysis area of 500 X 500 μm^2 (ca. 1.5 X 10^{11} primary ions/cm^2) ensured that the analysis was performed within the static limit. The PCA analysis of the SIMS data, including its preprocessing (normalization and autoscaling), were performed as described previously.[31]

4.4. Results and Discussion

4.4.1. XPS of Surfaces Before and After NP Deposition and Before and After Fluorine Plasma Treatment

XPS revealed the elemental compositions (Figure 4.2) and chemical states (Figure 4.3) of the elements in the uncoated aluminum and NP-coated aluminum samples before and after fluorine plasma treatment. The structure of the NP ligand, which contains three phosphonate groups that should interact strongly with the Al(III) in aluminum oxide, is given in Figure 4.1. Figure 4.2a shows the XPS P/Al ratio for the samples. Interestingly, a small amount of phosphorus appears to

be present as a contaminant in all of the surfaces, and this P is partially removed from the uncoated Al sample when it is treated with the fluorine plasma, cf. the Al-0s and Al-8s results. The source of this phosphorus contamination is unknown. As expected, the NP-coated sample (NP-0s) shows by far the largest P/Al ratio. This ratio then drops precipitously when the samples are exposed to the F plasma; even 4 s of plasma treatment is sufficient to reduce the P/Al ratio to about that of the Al-8s sample, and a longer exposure to this plasma appears to result in the continued, low level loss of phosphorus from the surfaces. The NP molecule also contains nitrogen. The nitrogen content of the untreated aluminum samples (Al-0s) is very low, but it becomes substantial after NP treatment. The theoretical P/N ratio for the NP molecule in Figure 4.1 is 3, and the P/N XPS area ratio of the NP-0s sample is 2.8, which is reasonably close to this value. Somewhat unexpectedly, fluorine plasma treatment also introduces a considerable amount of nitrogen into the samples, i.e., consider the Al-8s and NP-4s – NP-20s samples. The presence of nitrogen on the samples after F plasma treatment suggests the presence of air in the chamber. Comparison of the NP-4s – NP-20s samples indicates a slow removal of nitrogen from the materials with increased F plasma exposure, i.e., the plasma appears to both introduce nitrogen contamination onto the surfaces and then gradually remove it. In summary, these results point to the expected adsorption of NP to the Al surface, its removal by the F plasma, and the introduction of nitrogen to the surfaces during plasma treatment.

Fluorine plasma treatment also leads to substantial changes in the substrate. Figure 4.2b shows the XPS F/Al, O/Al, and C/Al ratios for the samples. The F/Al and O/Al ratios behave in opposing ways. For example, the untreated Al (Al-0s) and NP-coated (NP-0s) samples show high O/Al and very low F/Al ratios. However, after treatment with the F plasma, the F/Al ratios become very large and the O/Al ratios drop substantially. These results suggest loss of oxygen in the

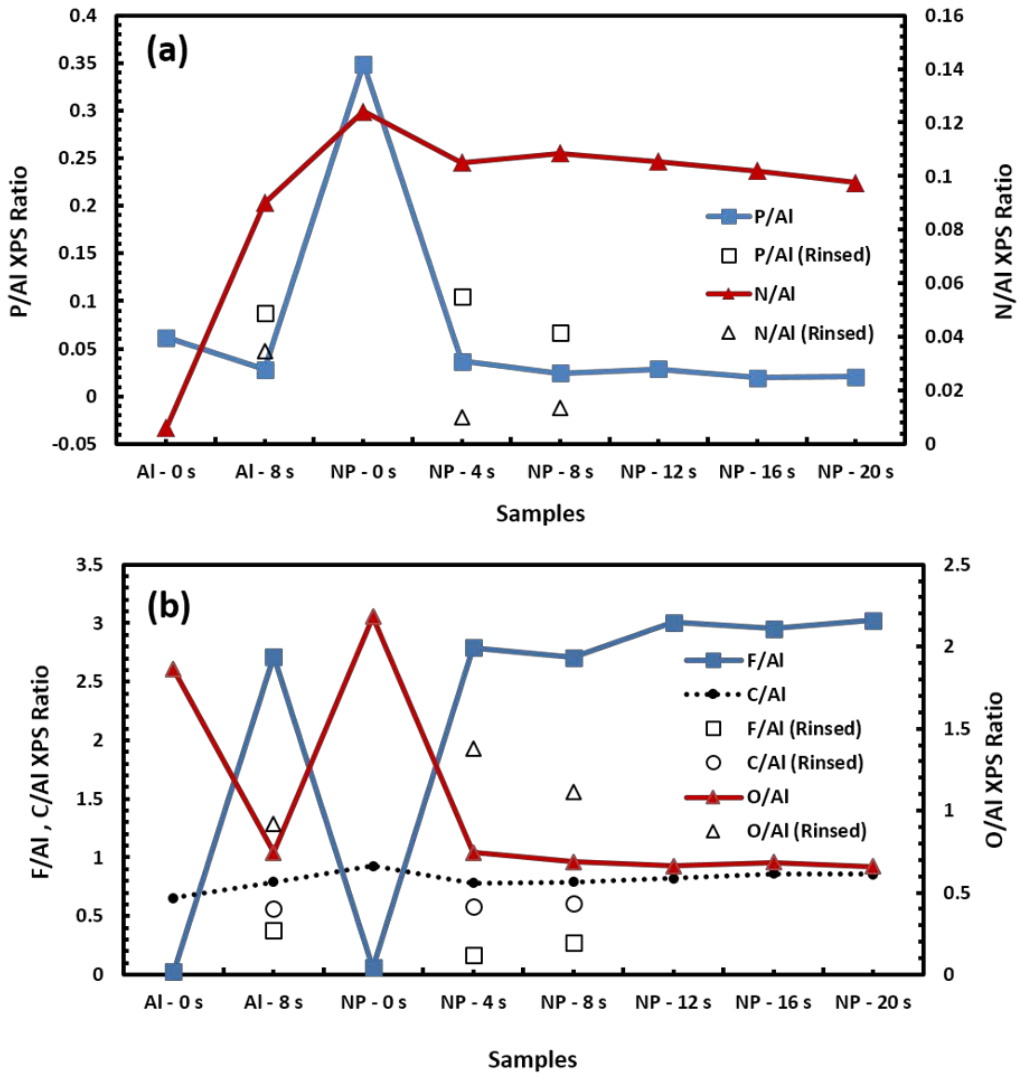

Figure 4.2. (a) P/Al and N/Al, and (b) O/Al, F/Al, and C/Al XPS pear area ratios of bare aluminum (Al-0s), bare aluminum after 8 s of fluorine plasma treatment (Al-8s), aluminum coated with NP (NP-0s), and NP-coated aluminum after exposure to a fluorine plasma for 4s – 20 s before (solid symbols) and after (open synbols) rinsing with water.

substrate and its replacement by fluorine. The F/Al and O/Al ratios in Figure 4.2b further indicate that most of the change in the samples has taken place after 4s of plasma treatment, and that longer exposures to the plasma result in a continued, slow replacement of surface oxygen. Carbon is present on all the samples, and while as expected, the XPS C/Al ratio is highest for the NP-0s sample, comparable amounts of carbon are found on all of the samples. This comes as little surprise because (i) NP deposits as a monolayer and it is a rather small adsorbate, and (ii) aluminum oxide is expected to readily contaminate with hydrocarbon because of its high free energy. Finally, there appears to be a slow increase in the carbon content of the surfaces with fluorine plasma treatment. This result is consistent with the fact that the 'F plasma' contains carbon – it is actually 'CF_4 + O_2'.

The confirmation of and change in elemental compositions suggested in Figure 4.2 are complemented by the corresponding P 2p, N 1s, Al 2p, O 1s, and F 1s narrow scans in Figure 4.3. For example, Figure 4.3a indicates that there are two types of phosphorus in the samples. The first type, Type I, appears at lower binding energy (133.1 – 133.5 eV), and is present on the surfaces that had not been coated with NP or that had been treated with both NP and the fluorine plasma. The second type, Type II, appears at higher binding energy (134.7– 135.3 eV), and corresponds to the rather oxidized form of phosphorus that is in the NP molecule. That is, both carbon and oxygen are more electronegative than phosphorus so if the electrons in the NP phosphorus are assigned to the atoms around it, per the typical rules used to assign oxidation states,[30] phosphorus will be found in a high (+5) oxidation state. As was suggested in Figure 4.2, these results are consistent with the removal of NP from the NP-0s surface during fluorine plasma treatment. In summary, there is some phosphorus contamination on the samples initially, the amount of phosphorus on the samples then increases significantly when NP adsorbs to them, the phosphorus in NP has a different

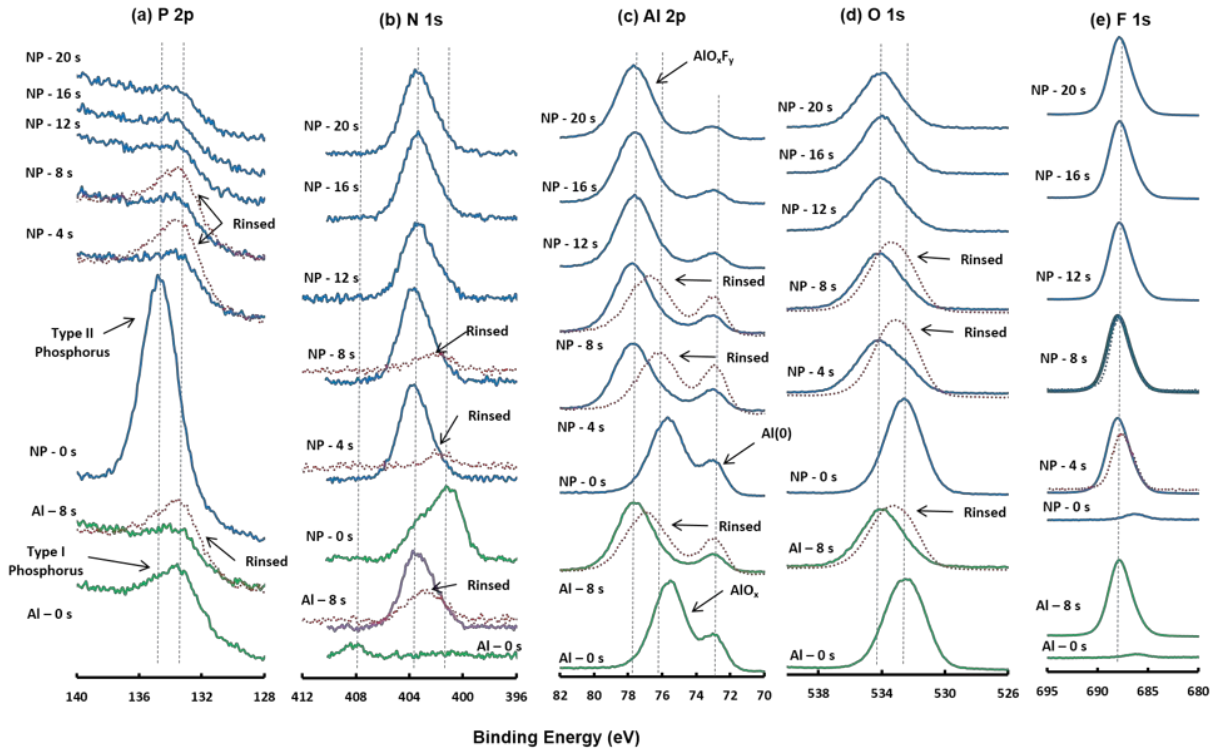

Figure 4.3. (a) P 2p, (b) N 1s, (c) Al 2p, (d) O 1s, and (e) F 1s XPS narrow scans of bare aluminum (Al-0s), bare aluminum after 8 s of fluorine plasma treatment (Al-8s), aluminum coated with NP (NP-0s), and NP-coated aluminum after exposure to a fluorine plasma for 4s – 20 s before (solid lines) and after (dashed lines) rinsing with water.

chemical state from the phosphorus contamination, and phosphorus in the +5 oxidation from NP is not found on the samples after fluorine plasma treatment. Note also that the large signal from the Type II (NP) phosphorus probably masks any smaller signal from Type I phosphorus that may still be present on the samples.

The N 1s narrow scans in Figure 4.3b tell a similar story to the P 2p scans in Figure 4.3a, except that the unmodified Al samples (Al-0s) show very little nitrogen. The small signal that is present in these narrow scans at ca. 408 eV is consistent with nitrogen in a high oxidation state, i.e., probably nitrate (NO_3^-).[36] For the NP-coated sample (NP-0s), the nitrogen appears to be in two oxidation states: one at ca. 401 eV and the other at ca. 403.5 eV. Consistent with literature precedent, I assign the lower energy peak to unprotonated nitrogen in the NP molecule (see Figure 4.1), and the higher energy peak to the same, but protonated, nitrogen.[37, 38] The higher binding energy for the protonated nitrogen is consistent with it generally being more difficult to remove an electron from a positively charged entity than a neutral one. The ratio of the signals from the protonated and unprotonated nitrogen atoms suggests that about one-third of the nitrogen in adsorbed NP is protonated. As previously noted, plasma treatment also appears to introduce nitrogen into the samples. That is, with or without prior adsorption of NP, plasma treated samples show a strong N 1s signal at ca. 403.5 eV, where most of the nitrogen in the plasma treated samples appears to be in this chemical state. The fact that this peak appears on the Al-8s sample, and that its intensity is nearly as great as those from the NP-4s – NP-20s samples, suggests that the plasma also removes the NP nitrogen.

The Al 2p narrow scans in Figure 4.3c consistently show two peaks. The lower energy peak in all the spectra at 73.0 eV is assigned to metallic aluminum, Al(0). Metallic aluminum typically shows a high binding energy tail by XPS,[39, 40] but this tail could not be discerned here because of

the presence of neighboring peaks at higher binding energy in the spectra, of which two types were observed. The first is present in the two samples that had not 'seen' the F plasma: the Al-0s and NP-0s samples. These two spectra show a peak at ca. 75.7 eV, which is known in the literature to correspond to the oxidized aluminum in aluminum oxide.[8, 12, 13, 29, 41] The similarity of the spectra of these two samples implies that deposition of NP does not substantially perturb the aluminum substrate. The second type of signal, which has also been observed previously, is present in samples that have been treated with the F plasma. Here, the oxide peak is shifted to even higher binding energy (ca. 77.7 eV).[8, 12, 13, 41] This result is consistent with an element more electronegative than oxygen binding to aluminum, and/or to the oxygen binding to aluminum. The only element more electronegative than oxygen is fluorine, so these narrow scans suggest that the fluorine plasma treatment of aluminum produces an aluminum fluoride/ oxyfluoride species, which is consistent with the removal of oxygen from the samples and the concomitant gain in fluorine revealed in Figure 4.2. Note also that the Al(0) peaks in the spectra of fluorine plasma-treated samples are responsible for a smaller fraction of the total area of the Al peak envelopes than the Al(0) peaks in the Al-0s and NP-0s spectra. This result indicates that the F plasma oxidizes the aluminum beneath the original oxide. The O 1s narrow scans in Figure 4.3d tell a similar story. The O 1s signals from the Al-0s and NP-0s samples are very similar, and the O 1s signals from the plasma treated samples are also chemically similar, but shifted to higher binding energy. This shift again suggests the formation of oxygen-fluorine bonds. Interestingly, there is a shoulder on the NP-4s O 1s narrow scan that suggests both aluminum oxide and aluminum oxyfluoride in the materials. With additional plasma treatment, i.e., at 8 s of plasma treatment or beyond, this lower energy shoulder disappears. These results are consistent with the gradual decrease in oxygen and increase in fluorine with increased plasma treatment suggested in Figure 4.2b. Finally, the F 1s

narrow scans in Figure 4.3e suggest that the trace fluorine initially present on the Al-0s and NP-0s samples, which is probably F^-, is superseded by a different form of fluorine in the plasma-treated surfaces at higher binding energy, probably oxyfluoride.

4.4.2. Effects of Rinsing

In order to better understand the durability of any modifications made to the surfaces by plasma treatment, three of the samples (Al-8s, NP-4s, and NP-8s) were rinsed with high purity water for 2 min and then analyzed by XPS. The XPS N/Al, P/Al, F/Al, O/Al, and C/Al ratios of these samples are shown in Figure 4.2. In general, the same results were obtained with all three surfaces. That is, this rinse: (i) very substantially reduced the amount of nitrogen on the surfaces, (ii) moderately increased the P/Al ratio, (iii) very substantially reduced the amount of fluorine on the surfaces, (iv) moderately raised the amount of oxygen on the surfaces, and (v) decreased somewhat the amount of carbon. The decrease in the F/Al ratio and concomitant increase in surface oxygen suggests some degree of reversibility to the effects of the fluorine plasma. The only result that was unexpected here was the apparent increase in phosphorus with rinsing. Although the exact cause for the increase in the P/Al ratio is unknown, there is a possibility that the phosphorus exists at the surface as an insoluble species so that as water removes other soluble material around it, the remaining phosphorus is concentrated at the surfaces. In summary, fluorine plasma treatment creates a number of surface species that can be removed by rinsing.[12]

More detailed information about the changes in surface chemistry after rinsing were obtained from the P 2p, N 1s, Al 2p, and O 1s narrow scans of the materials (see dotted lines in Figure 4.3). Figure 4.3a indicates that the chemical state of the phosphorus at the surfaces does not change substantially before and after rinsing. This result would be consistent with the water having

little or no effect on this species. However, the other three elements *do* change their chemical states after rinsing. For example, rinsing, especially in the case of the NP-4s and NP-8s samples, appears to remove the more oxidized form(s) of nitrogen from the samples. Once again in agreement to the argument that rinsing somewhat reverses the effects of the fluorine plasma, Figures 5.3c and 5.3d show shifts in the Al 2p and O 1s narrow scans to lower binding energy after rinsing, which is in the direction of the untreated samples. Figure 4.3c also shows that the Al(0) peak increases in intensity relative to the oxide peak after rinsing, indicating that rinsing removes aluminum oxyfluoride species from the surfaces.

4.4.3. Heating of Plasma-Treated Samples in the Air and Under Vacuum

Gas phase processes are often preferred over wet processes in semiconductor manufacturing. Accordingly, to explore 'dry' methods for removing fluorine from plasma-treated aluminum surfaces, two samples (Al-8s and NP-8s) were heated in the air at 300 °C for 5 h. Figure 4.4 shows the XPS survey and Al 2p narrow scans for these samples before and after this thermal treatment. It is of significance that: the fluorine is almost entirely removed from these surfaces, the XPS F/O ratios of these surfaces reverse (moderately large prior to heating, very small after), the oxyfluoride peaks in the Al 2p narrow scans shift to lower binding energy (consistent with the loss of F from the surfaces), and the Al(0) peak decreases in intensity relative to the oxide peak, suggesting a deeper oxide layer on the surfaces.

To understand and confirm that air (probably water in the air) is necessary for the removal of fluorine from plasma treated surfaces, ToF-SIMS was performed on the Al-8s sample before and after heating at 300 °C for 5 h under vacuum (10^{-8} mbar) and for 5 h in the air (see Figure 4.5). Static SIMS is extremely sensitive to fluorine, and the SIMS spectrum of the Al-8s sample is

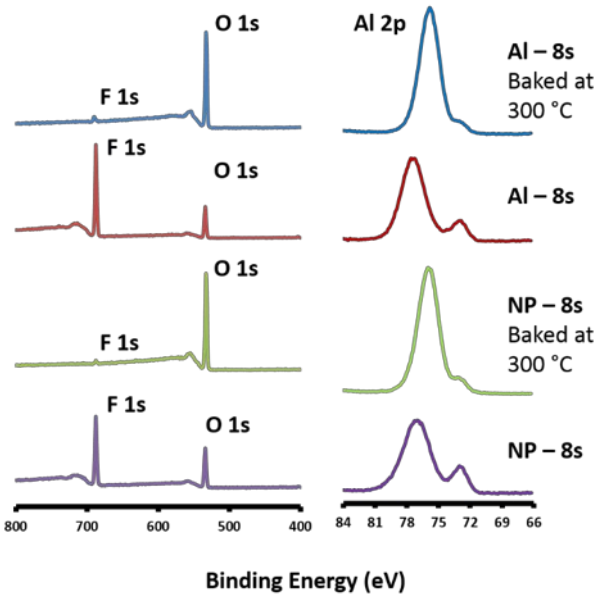

Figure 4.4. Survey and Al 2p narrow scans of bare aluminum and NP-coated aluminum samples treated with fluorine plasma for 8 s followed by baking for 5 hours at 300 °C in air.

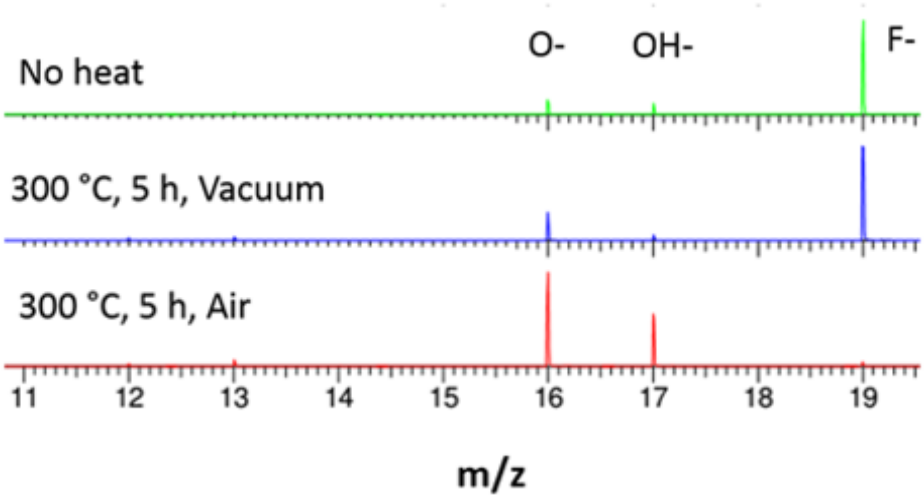

Figure 4.5. ToF-SIMS spectra of the 'Al-8s' sample without any heat treatment (top), after heating at 300 °C in vacuum (middle), and after heating at 300 °C in the air for 5 h (bottom). The '300 °C, 5 h, Vacuum' sample was immediately analyzed without breaking vacuum.

initially dominated by the F^- peak, with small O^- and OH^- signals also present. The spectrum is still dominated by the F^- signal after the sample is heated under vacuum for 5 h, although the O^- signal becomes more intense relative to the OH^- signal after this treatment. At least part of this change may be due to desorption of water from the sample surface. The SIMS spectrum of the sample heated in the air for 5 h is profoundly different from the previous two spectra. Consistent with the results in Figure 4.4, the F^- signal is almost entirely gone and strong O^- and OH^- peaks are present.

4.4.4. Evolution of the Samples with Aging

As previously mentioned, the uncoated and NP-coated samples were analyzed three times by XPS. The time gap between each analysis was ca. one week. Between analyses the samples were stored in the laboratory in covered containers, but they were otherwise exposed to the laboratory air, and no effort was made to shield them from the room lights. Figure 4.6 shows the XPS P/Al, N/Al, F/Al, O/Al, and C/Al ratios for the samples initially (Week 1) and after two weeks of storage (Week 2 and Week 3). For the various samples, there is little or no change in the P/Al, N/Al, and C/Al ratios. However, there are generally noticeable changes in the F/Al and O/Al ratios. That is, in general, the F/Al ratio decreases and the O/Al ratio increases with sample storage. These results suggest slow hydrolysis of fluorine from these samples with time that is consistent with the loss of fluorine from the surfaces that were heated in the air (vide supra).

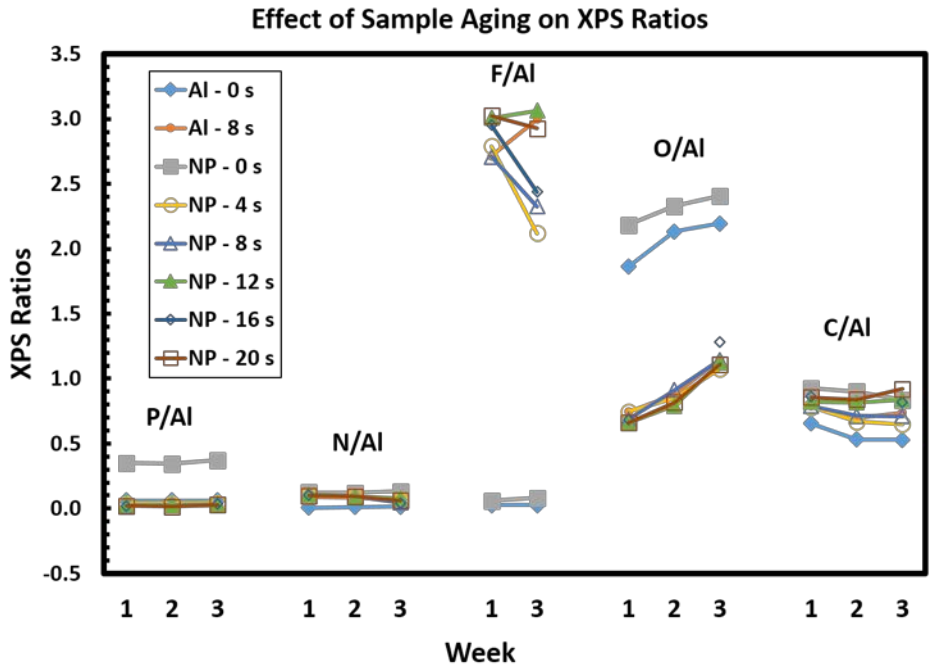

Figure 4.6. Evolution of XPS P/Al, N/Al, F/Al, O/Al, and C/Al ratios of uncoated and plasma treated samples over three weeks.

4.4.5. Comments on the ToF-SIMS Data, Including a PCA Analysis

The surfaces discussed herein were also analyzed by time-of-flight secondary ion mass spectrometry (ToF-SIMS). From each negative ion spectrum, the same 21 peaks were identified and individually integrated: O^-, OH^-, F^-, CN^-, F_2^-, N_2OH^-, NO_2^-, PNH_2^-, NO_3^-, PO_2^-, AlF_2^-, PO_3^-, $H_3O_2AlF^-$, AlF_4^-, $H_6OAl_2F_2^-$, $H_2O_5FAl^-$, $H_4O_6AlF^-$, $H_2O_3AlF_4^-$, $H_4O_7AlF^-$, $H_6O_3F_3Al_2^-$, and $H_3OAl_2F_6^-$ (see Table 4.1). It would be reasonable to expect that these peaks could be divided into three groups corresponding to the surfaces (i) prior to NP treatment (O^-, OH^-, N_2OH^-, NO_2^-, and NO_3^-), (ii) after NP treatment, but before plasma treatment (CN^-, PNH_2^-, PO_2^-, PO_3^-), and (iii) after fluorine plasma treatment (F^-, F_2^-, AlF_2^-, $H_3O_2AlF^-$, AlF_4^-, $H_6OAl_2F_2^-$, $H_2O_5FAl^-$, $H_4O_6AlF^-$, $H_2O_3AlF_4^-$, $H_4O_7AlF^-$, $H_6O_3F_3Al_2^-$, and $H_3OAl_2F_6^-$). The series of $H_xO_yAl_zF_a^-$ type peaks observed here is a confirmation of the aluminum oxyfluoride species predicted above. The PO_2^- and PO_3^- peaks observed here are typically observed in the SIMS of phosphates, e.g., DNA,[42, 43] and the CN^- peak is typical of organic nitrogen-containing compounds.[32, 43] To better understand the relationships between the samples, a principal components analysis (PCA) of the data was performed. PCA is a multivariate analysis technique that allows large sets of data, e.g., spectra or spectral regions, to be compared in a rather straightforward way. PCA analyses on SIMS data sets have been performed in Linford's group, which I joined as a graduate student in 2008. They/I have very consistently found that PCA results agree with the expected chemical differences between the samples.[31-33, 44, 45]

The scores and loadings plots generated in this analysis are presented in Figures 4.7-4.12. The first principal component (PC) accounted for 70.0% of the variation in the data (see Figure 4.7 and 4.8). It divided the data into two groups – the samples that had not undergone fluorine plasma treatment and those that had. In confirmation of the expected chemistry of these surface,

No.	Center Mass (u)	Assignment	
1	15.995	O-	O^-
2	17.003	OH-	OH^-
3	18.999	F-	F^-
4	26.003	CN-	CN^-
5	38.001	F_2-	F_2^-
6	45.000	N_2OH-	N_2OH^-
7	45.995	NO_2-	NO_2^-
8	46.971	PNH_2-	PNH_2^-
9	61.994	NO_3-	NO_3^-
10	62.970	PO_2-	PO_2^-
11	64.973	AlF_2-	AlF_2^-
12	78.967	PO_3-	PO_3^-
13	80.973	H_3O_2AlF-	$H_3O_2AlF^-$
14	102.977	AlF_4-	AlF_4^-
15	113.994	H_6OAl_2F_2-	$H_6OAl_2F_2^-$

16	127.986	H_2O_5FAl-	$H_2O_5FAl^-$
17	145.976	H_4O_6AlF-	$H_4O_6AlF^-$
18	153.003	H_2O_3AlF_4-	$H_2O_3AlF_4^-$
19	161.976	H_4O_7AlF-	$H_4O_7AlF^-$
20	164.943	H_6O_3F_3Al_2-	$H_6O_3F_3Al_2^-$
21	186.939	H_3OAl_2F_6-	$H_3OAl_2F_6^-$

Table 4.1. Peaks from the negative ion spectra selected for a principal components analysis (PCA) of the ToF-SIMS data.

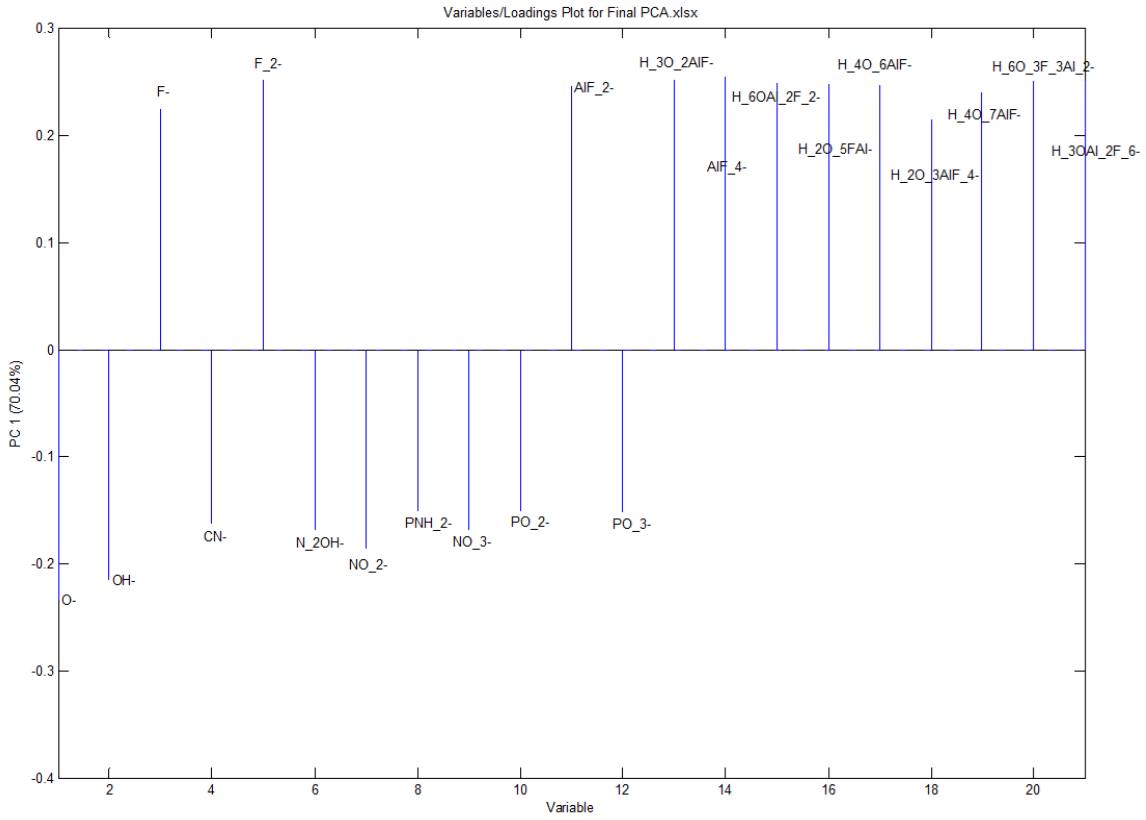

Figure 4.7. The PCA loadings for PC 1, which captured the variation due to the fluorine plasma. The variables are labeled with molecular formulae of the ion observed in the mass spectrum. Note that, for example, 'PO_3-'should be read as 'PO_3^-'. Refer to Table 4.1 for greater clarification. Please note that these are tentative assignments that may be incorrect for variables 13 - 21, which are for the fluorinated peaks.

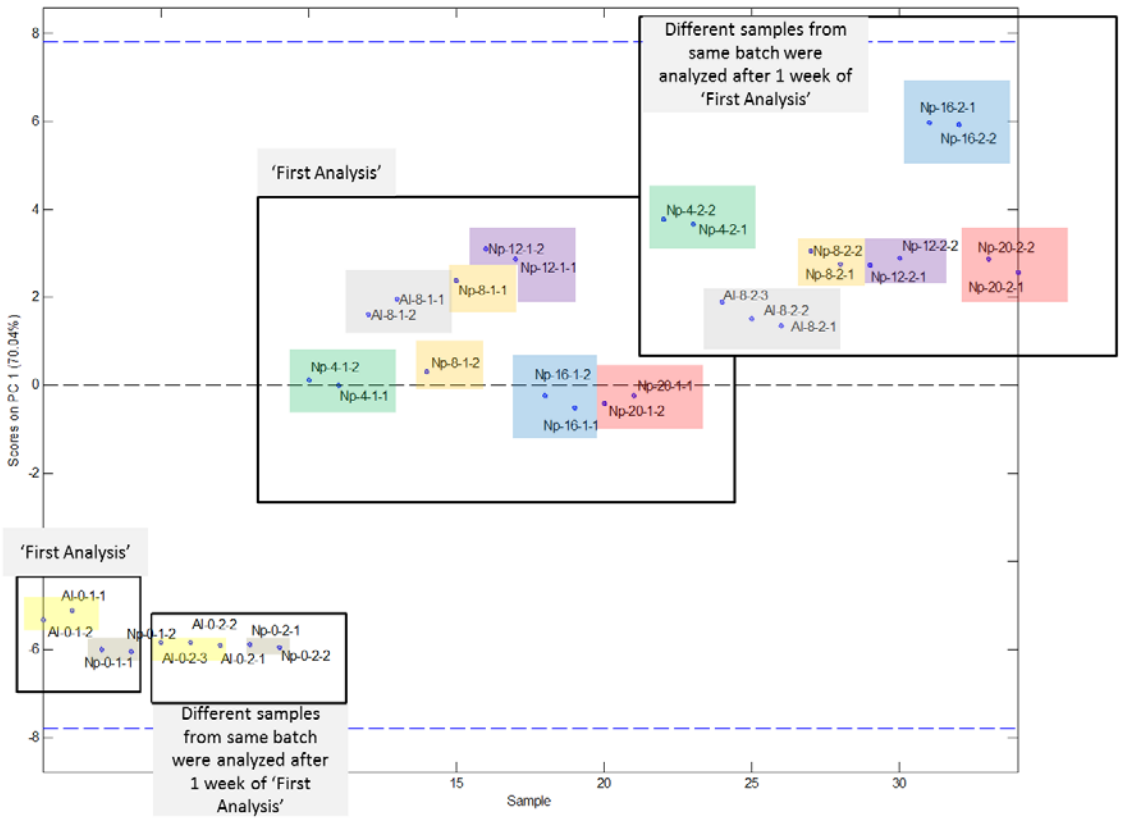

Figure 4.8. The PCA scores for PC 1, which captured the variation in the samples induced by the fluorine plasma. The sample dots are enclosed in color coded boxes for the same type of samples. Two sets of samples from the same batch were analyzed with a one week gap between their analyses. The sample names used here have four parts separated by hyphens: (1) NP and Al for NP coated and bare aluminum, respectively, (2) a number (0, 4. 8, 12, 16, and 20) corresponds to the plasma exposure time in seconds, (3) a second number: '1' or '2' indicates samples analyzed the first or a week after, respectively, and (4) a third number: '1' or '2' that refer to samples numbers for the same type of samples that were analyzed at the same time.

the plot of the loadings on PC1 showed that the spectra of the fluorine plasma treated samples were richer in *all* the ions listed in group (iii) (see previous paragraph), and that the spectra from the untreated samples were richer in *all* the ions from groups (i) and (ii) above. These results are consistent with damage/removal of the NP molecule by the plasma and replacement of oxygen by fluorine. In the plot of the scores on PC1 there is also a hint of a separation between the spectra corresponding to the samples analyzed after their creation and those analyzed a week later. PC2 (see Figure 4.9 and 4.10) accounted for 17.8% of the variation in the data. It cleanly separated the samples into three groups. The untreated, bare aluminum samples, which had negative scores on PC2, the NP-coated aluminum samples, which had positive scores on PC2, and all the samples that had been treated with the fluorine plasma, which showed scores of essentially zero. As expected, the only peaks of significance in the loadings plot for PC2 were from groups (i) and (ii) above. That is, all the peaks in group (i), except oxygen, which showed a very small loading, had negative loadings and corresponded to the untreated samples. In contrast, all the peaks in group (ii) had positive loadings and corresponded to the NP-treated samples. Again, these results are in very good agreement with the expected chemistries of the surfaces, e.g., the NO_2^- and NO_3^- ions are obtained from the untreated samples, which is consistent with the oxidized nitrogen signal at ca. 408 eV from the Al-0s sample (see Figure 4.3b). For PC3, see Figure 4.11 and 4.12, which accounted for 9.6% of the variation in the data, the loading of the F^- signal was negative and all the remaining peaks had positive loadings. The spectra with the most negative scores on this PC were samples treated with the plasma and analyzed soon after their preparation, while those showing more positive scores on PC3 were either not treated with the plasma or analyzed at a later time. In a PCA analysis, higher PCs generally account for less and less of the variation in the data, and any correlation of the sample chemistry to the PCA results becomes more and more tenuous.

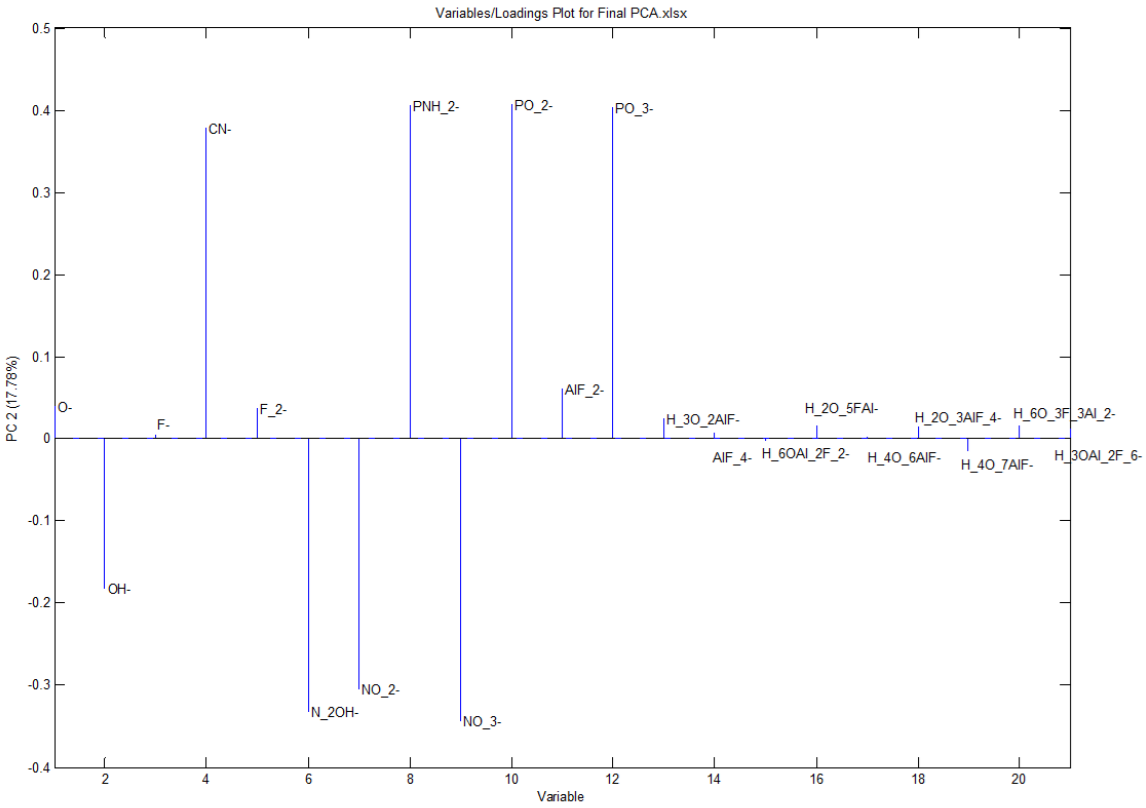

Figure 4.9. The PCA loadings and scores for PC 2, which captured the variation in the NP layer. The variables are labeled with the molecular formulae of the ion observed in the mass spectrum. Note, for example, that 'PO_3-'should be read as 'PO_3^-'. Refer to Table 4.1 for additional clarification. Please note that these are tentative assignments that may be incorrect for variables 13 - 21, which are for the fluorinated peaks.

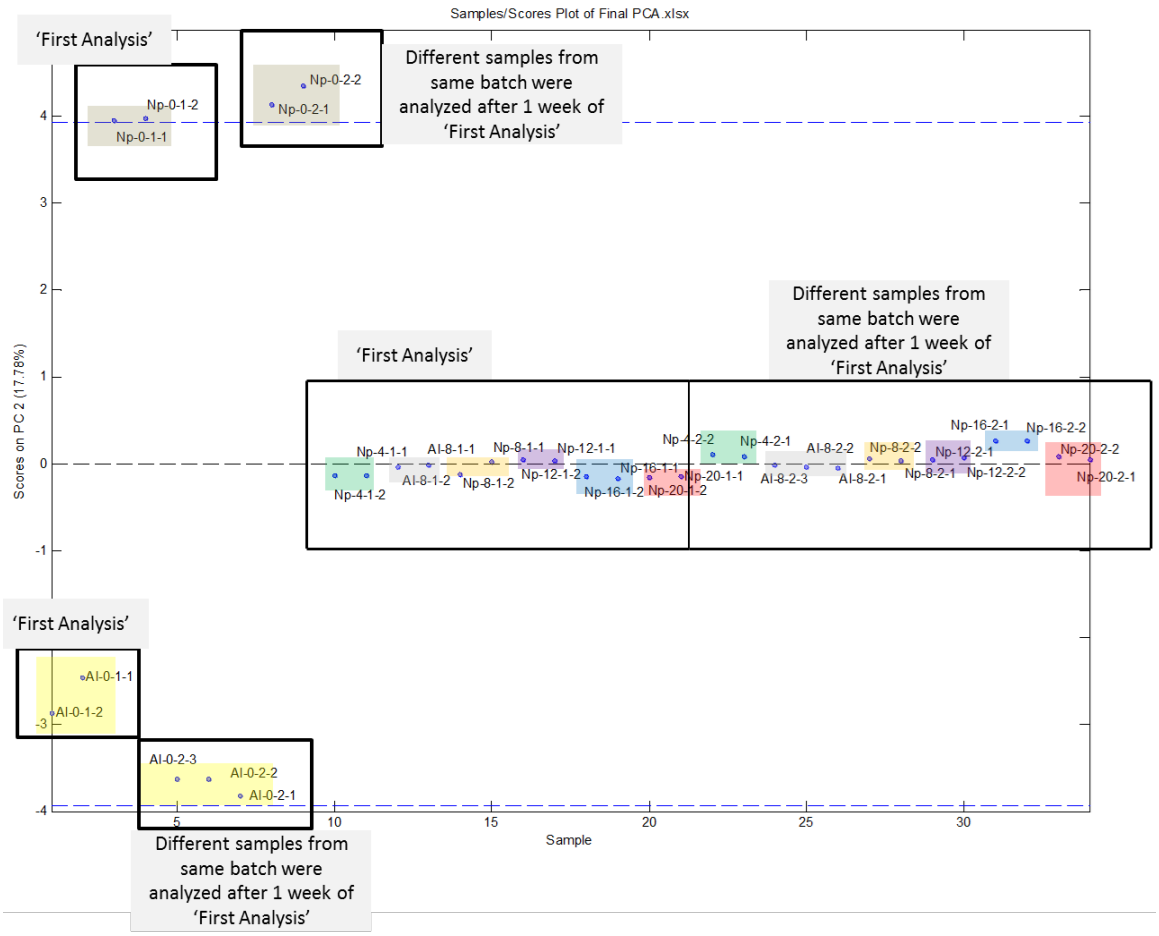

Figure 4.10. The PCA loadings and scores for PC 2, which captured the variation due to the NP layer. The sample dots are enclosed in color-coded boxes for the same type of samples. Two sets of samples from the same batch were analyzed at one week gap. The sample names used here have four parts separated by hyphens: (1) NP and Al for NP coated and bare aluminum, respectively, (2) a number (0, 4. 8, 12, 16, and 20) corresponds to the plasma exposure time in seconds, (3) a second number: '1' or '2' indicates samples analyzed the first or a week after, respectively, and (4) a third number: '1' or '2' that refer to samples numbers for the same type of samples that were analyzed at the same time.

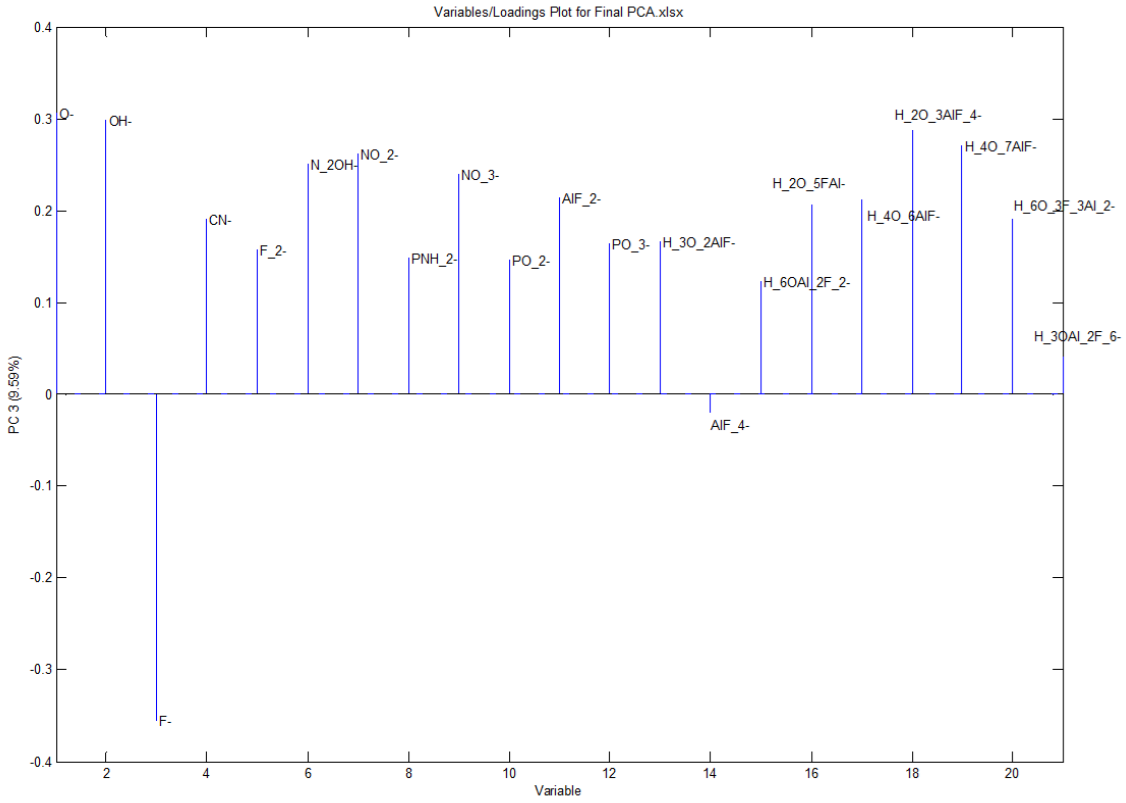

Figure 4.11. The PCA loadings and scores for PC 3, which captured the variation among the samples induced by the fluorine plasma. The variables are labeled with the molecular formulae of the ion observed in the mass spectrum. Note, for example, that 'PO_3-' should be read as 'PO_3^-'. Refer to Table 4.1 for additional clarification. Please note that these are tentative assignments that may be incorrect for variables 13 - 21, which are for the fluorinated peaks.

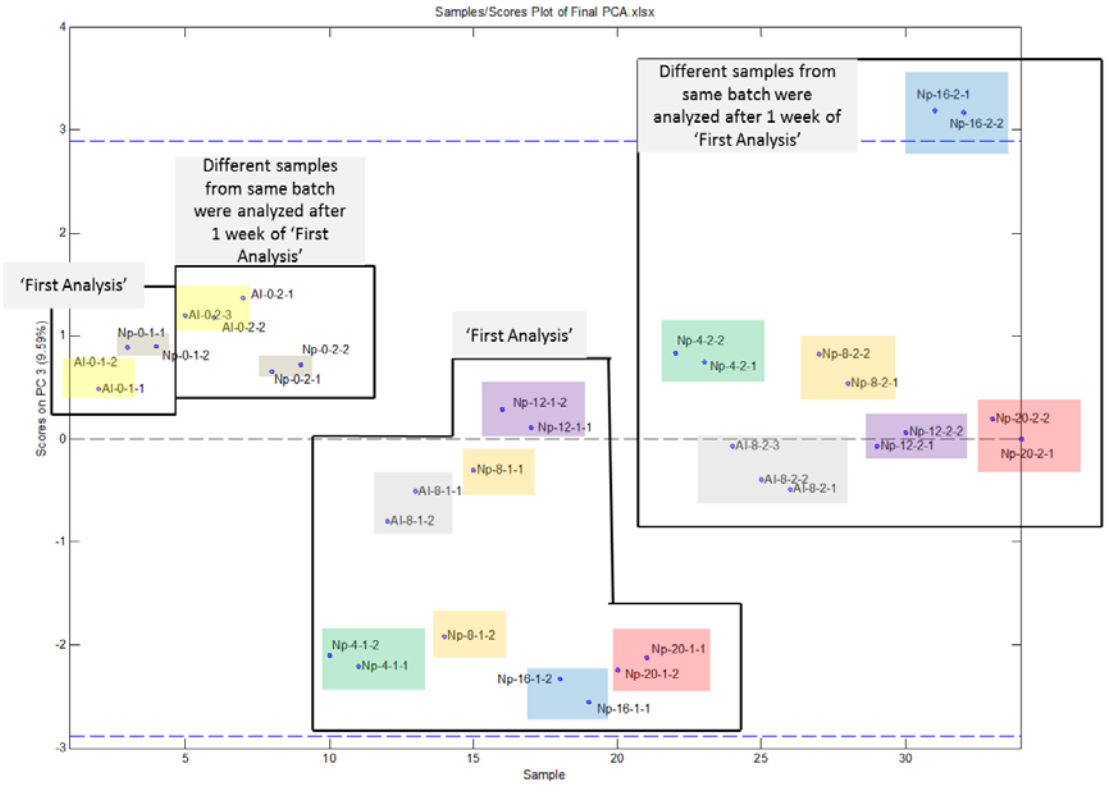

Figure 4.12. The PCA loadings and scores for PC 3, which captured the variation among the samples induced by the fluorine plasma. The sample dots are enclosed in color coded boxes for same type of samples. Two sets of samples from the same batch were analyzed at one week gap. The sample names used here have four parts separated by hyphens: (1) NP and Al for NP coated and bare aluminum, respectively, (2) a number (0, 4. 8, 12, 16, and 20) corresponds to the plasma exposure time in seconds, (3) a second number: '1' or '2' indicates samples analyzed the first or a week after, respectively, and (4) a third number: '1' or '2' that refer to samples numbers for the same type of samples that were analyzed at the same time.

This is the case here – while the results for PC3 agree with the sample chemistry in a fairly general way, the groupings in the scores plot are not as tight as for the first two PCs.

Finally, it was noted that the NH_4^+ peak was observed in all the positive ion spectra from all the samples. However, the fact that no sign of this species is indicated in the N 1s narrow scan from the Al-0s surface (it should appear at roughly the same location as the protonated amine signal in the NP-0s narrow scan in Figure 4.3b) suggests that its concentration is quite low. Perhaps this result can be explained by noting that (i) SIMS has a strong matrix effect, and (ii) silicon surfaces are often exposed to NH_3-containing cleaning solutions.

4.5. Conclusions

NP is a widely used corrosion inhibitor for aluminum that has not been studied to any significant degree by XPS or SIMS. These techniques confirm the deposition of NP on alumina/aluminum and show the expected elements and molecular fragments. NP is substantially damaged by a fluorine plasma. In addition, a fluorine plasma significantly changes the aluminum substrate beneath NP, replacing the oxygen in its native oxide layer with fluorine and/or oxidizing it. ToF-SIMS of fluorine plasma treated NP/aluminum samples reveals a series of $H_xO_yAl_zF_a^-$ type peaks that are consistent with the formation of an aluminum oxyfluoride. All of this is useful information because both fluorine plasmas and aluminum are commonly used in semiconductor processing, and NP is widely believed to protect aluminum. The replacement of oxygen with fluorine appears to be fairly reversible. Rinsing in water substantially removes fluorine from the surface of aluminum oxyfluoride. Fluorine is also slowly replaced by oxygen if an aluminum oxyfluoride material is exposed to the air. This process is accelerated by heating, but strongly inhibited if the heating is performed under vacuum. This study shows that formation of

hygroscopic aluminum oxyfluoride species and damage to the NP layer during fluorine plasma treatment of aluminum based devices renders them vulnerable to corrosion while sitting in storage.

4.6. References

1. Gatto, A.; Yang, M.; Kaiser, N.; Heber, J.; Schmidt, J. U.; Sandner, T.; Schenk, H.; Lakner, H. *Appl. Opt.* **2006,** *45* (7), 1602-1607.

2. Chupas, P. J.; Grey, C. P. *J. Catal.* **2004,** *224* (1), 69-79.

3. Cho, E.; Mun, J.; Chae, O. B.; Kwon, O. M.; Kim, H.-T.; Ryu, J. H.; Kim, Y. G.; Oh, S. M. *Electrochem. Commun.* **2012,** *22* (0), 1-3.

4. S. Choi, I.; C. Park, J. *Surf. Coat. Technol.* **2000,** *131* (1–3), 383-385.

5. Sun, J.; Li, X.; Zhang, W.; Yi, K.; Shao, J. *Opt. Laser Technol.* **2014,** *56* (0), 65-70.

6. Stosiek, C.; Scholz, G.; Eltanany, G.; Bertram, R.; Kemnitz, E. *Chem. Mater.* **2008,** *20* (17), 5687-5697.

7. Chong, Y. F.; Gopalakrishnan, R.; Tsang, C. F.; Sarkar, G.; Lim, S.; Tatti, S. *Microelectron. Reliab.* **2000,** *40* (7), 1199-1206.

8. Kwon, K. H.; Yun, S. J.; Kim, C. I.; Park, J. M.; Baek, K. H.; Yoon, Y. S.; Kim, S. G.; Nam, K. S. *J. Electrochem. Soc.* **1998,** *145* (3), 1044-1048.

9. Tzou, R.; Shih, H. *Corrosion* **1989,** *45* (4), 328-333.

10. Ramos, R.; Cunge, G.; Pelissier, B.; Joubert, O. *Plasma Sources Sci. Technol.* **2007,** *16* (4), 711.

11. Kim, J.-W.; Kim, Y.-C.; Lee, W.-J. *J. Appl. Phys.* **1995,** *78* (3), 2045-2049.

12. Jimbo, S.; Shimomura, K.; Ohiwa, T.; Sekine, M.; Mori, H.; Horioka, K.; Okano, H. *Jpn. J. Appl. Phys.* **1993**, 32, 3045-3045.

13. Hegde, R.; Barteau, M. *J. Catal.* **1989,** *120* (2), 387-400.

14. Lee, Y. H.; Zhou, Z. H.; Danner, D. A.; Fryer, P. M.; Harper, J. M. *J. Appl. Phys.* **1990,** *68* (10), 5329-5336.

15. Gawalt, E. S.; Avaltroni, M. J.; Koch, N.; Schwartz, J. *Langmuir* **2001,** *17* (19), 5736-5738.

16. DeRose, J.; Hoque, E.; Bhushan, B.; Mathieu, H. *Surf. Sci.* **2008,** *602* (7), 1360-1367.

17. Hanson, E. L.; Schwartz, J.; Nickel, B.; Koch, N.; Danisman, M. F. *J. Am. Chem. Soc.* **2003,** *125* (51), 16074-16080.

18. Yee, C.; Kataby, G.; Ulman, A.; Prozorov, T.; White, H.; King, A.; Rafailovich, M.; Sokolov, J.; Gedanken, A. *Langmuir* **1999,** *15* (21), 7111-7115.

19. Hoque, E.; DeRose, J.; Bhushan, B.; Hipps, K. *Ultramicroscopy* **2009,** *109* (8), 1015-1022.

20. Hanson, E. L.; Guo, J.; Koch, N.; Schwartz, J.; Bernasek, S. L. *J. Am. Chem. Soc.* **2005,** *127* (28), 10058-10062.

21. Pujari, S. P.; Li, Y.; Regeling, R.; Zuilhof, H. *Langmuir* **2013,** *29* (33), 10405-10415.

22. McDowell, M.; Hill, I.; McDermott, J.; Bernasek, S.; Schwartz, J. *Appl. Phys. Lett.* **2006,** *88* (7), 073505.

23. Foster, T. T.; Alexander, M. R.; Leggett, G. J.; McAlpine, E. *Langmuir* **2006,** *22* (22), 9254-9259.

24. Luschtinetz, R.; Oliveira, A. F.; Frenzel, J.; Joswig, J.-O.; Seifert, G.; Duarte, H. A. *Surf. Sci.* **2008,** *602* (7), 1347-1359.

25. Lines, M.; Perkins, R. T. Corrosion resistant wire-grid polarizer and method of fabrication. US Patent 6,785,050: 2004.

26. Latos, E. J.; Payne, J. C., Corrosion inhibitors. US Patent 4,409,121:1983.

27. Zanzucchi, P. J.; Thomas III, J. H. *J. Electrochem. Soc.* **1988,** *135* (6), 1370-1376.

28. Madaan, N.; Kanyal, S. S.; Jensen, D. S.; Vail, M. A.; Dadson, A. E.; Engelhard, M. H.; Samha, H.; Linford, M. R. *Surf. Sci. Spectra* **2013,** *20*, 43.

29. Attavar, S.; Diwekar, M.; Linford, M. R.; Davis, M. A.; Blair, S. *Appl. Surf. Sci.* **2010,** *256* (23), 7146-7150.

30. Gupta, V.; Ganegoda, H.; Engelhard, M. H.; Terry, J.; Linford, M. R. *J. Chem. Educ.* **2013,** *91* (2), 232-238.

31. Gupta, V.; Madaan, N.; Jensen, D. S.; Kunzler, S. C.; Linford, M. R. *Langmuir* **2013,** *29* (11), 3604-3609.

32. Zhang, F.; Gates, R. J.; Smentkowski, V. S.; Natarajan, S.; Gale, B. K.; Watt, R. K.; Asplund, M. C.; Linford, M. R. *J. Am. Chem. Soc.* **2007,** *129* (30), 9252-9253.

33. Pei, L.; Jiang, G.; Tyler, B. J.; Baxter, L. L.; Linford, M. R. *Energy Fuels* **2008,** *22* (2), 1059-1072.

34. Beebe, K.; Pell, R.; Seasholtz, *Chemometrics: a practical guide*. John Wiley & Sons: New York: 1998.

35. Shirley, D. A. *Phys.Rev.B* **1972,** *5*, 4709.

36. Rubasinghege, G.; Grassian, V. H. *J. Phys. Chem., A* **2009,** *113* (27), 7818-7825.

37. Arrigo, R.; Havecker, M.; Schlogl, R.; Su, D. S. *Chem. Commun.* **2008,** *0* (40), 4891-4893.

38. Lourenço, J. M. C.; Ribeiro, P. A.; Botelho do Rego, A. M.; Braz Fernandes, F. M.; Moutinho, A. M. C.; Raposo, M. *Langmuir* **2004,** *20* (19), 8103-8109.

39. Sherwood, P. M. *J. Vac. Sci. Technol., A* **1996,** *14* (3), 1424-1432.

40. Jeurgens, L.; Sloof, W.; Tichelaar, F.; Borsboom, C.; Mittemeijer, E. *Appl. Surf. Sci.* **1999,** *144*, 11-15.

41. Miller, A. C.; McCluskey, F. P.; Taylor, J. A. *J. Vac. Sci. Technol., A* **1991,** *9* (3), 1461-1465.

42. Arlinghaus, H.; Ostrop, M.; Friedrichs, O.; Feldner, J.; Gunst, U.; Lipinsky, D. *Surf. Interface Anal.* **2002,** *34* (1), 35-39.

43. Saini, G.; Gates, R.; Asplund, M. C.; Blair, S.; Attavar, S.; Linford, M. R. *Lab Chip* **2009,** *9* (12), 1789-1796.

44. Yang, L.; Lua, Y.-Y.; Tan, M.; Sherman, O. A.; Grubbs, R. H.; Harb, J. N.; Davis, R. C.; Linford, M. R. *Chem. Mater.* **2007,** *19*, 1671 – 1678.

45. Yang, L.; Lua, Y.-Y.; Jiang, G.; Tyler, B. J.; Linford, M. R. *Anal. Chem.* **2005,** *77* (14), 4654-4661.

Chapter 5: Metal-Assisted Secondary Ion Mass Spectrometry (MetA-SIMS) with Bismuth

Note: The work presented in this chapter has been submitted to journal of Surface and Interface Analysis as Madaan, N., Linford, M.R., Metal-Assited Secondary Ion Mass Spectrometry (MetA-SIMS) with Bismuth.

5.1. Abstract

Deposition of thin layers of high Z metals on a sample before its analysis by time-of-flight secondary ion mass spectrometry (ToF-SIMS) leads to significant fragment specific improvements in signal intensities in the mass spectrum. This simple sample preparation technique is known as metal-assisted secondary ion mass spectrometry (MetA-SIMS). Correlating the correct metal layer thickness with the signal enhancement serves as the primary motivation for this work, where I have demonstrated that the most commonly employed QCM method can be a source of error. Accordingly, I introduce interference enhanced spectroscopic ellipsometry as a solution to determining film thicknesses. In addition, I chose a new high Z metal (bismuth) and a relatively high molecular weight polymer: polydiallyldimethylammonium chloride, PDADMAC, (MW ~100,000 – 200,000) to test some of the claims put forward in this work. A signal enhancement of 10 - 1600 was observed for the characteristic positive ions from a polymer with 6 - 10 nm thick bismuth layers. I also demonstrated that MetA-SIMS performed best in the absence of charge compensation using flood gun for a PDADMAC layer spin coated on a thick insulating substrate.

5.2. Introduction

Time of flight secondary ion mass spectrometry (ToF-SIMS) is a powerful analytical tool that exposes surfaces to short pulses of very fast moving primary ions (PI) that upon impact sputter both neutral and ionized atomic and molecular species. The ionized fraction of this sputtered material is analyzed by a time-of-flight mass spectrometer to yield mass spectra from which chemical information can be derived. ToF-SIMS has remarkable surface sensitivity, providing information about the upper few nanometers of sample surfaces. For some species its limit of detection is in the parts per million or perhaps even the parts per billion range. Nevertheless, the technique is limited because: (1) the ionized fraction of the sputtered material is generally quite low – most of the sputtered material is neutral and not detected, and (2) its ionization efficiency is often strongly influenced by the chemical environment of a sample, which means that the signal intensity cannot, in general, be directly correlated with the concentration of an analyte of interest. That is, SIMS has a matrix effect.[1] In order to improve the performance of ToF-SIMS, a significant amount of work has gone in to overcoming these obstacles. Approaches along these lines have included the development of polyatomic and cluster PI sources,[2-4] application of low molecular weight matrices mixed with analyte, i.e., matrix enhanced SIMS (ME-SIMS),[5, 6] preparation of thin layers of analyte on heavy metal substrates such as Au or Ag,[7] and metal assisted secondary ion mass spectrometry (MetA-SIMS). MetA-SIMS is a sample preparation technique that was introduced by Delcorte et al.[8] In MetA-SIMS, a thin (~2-10 nm) layer of a noble metal (Au or Ag) is deposited on a sample surface before ToF-SIMS analysis. Metal nanoparticles/clusters may also be used. Significant enhancements in SIMS signals, up to a few orders of magnitude, have been reported for a variety of materials. MetA-SIMS is the focus of the present work.

Among the above mentioned methods applied to improve ToF-SIMS ionization efficiencies, the application of polyatomic and cluster primary ions (PI) has by far surpassed any other method,[2-4] including MetA-SIMS.[1, 9] Nevertheless, MetA-SIMS offers some unique benefits that motivated me to carry out this work. For example, MetA-SIMS renders static-SIMS more quantitative by reducing its matrix effect.[10, 11] In other studies, successful SIMS analysis of insulating samples was achieved by MetA-SIMS without the need for an electron flood gun.[8, 12] This is a useful feature of the technique because irradiation of a sample with a flood gun may cause chemical damage, which can lead to an erroneous SIMS analysis.[13] MetA-SIMS is also a useful tool for understanding the complex collision cascade mechanism that takes place in a sample upon impact by a PI.[14, 15]

A great deal of sophisticated MetA-SIMS work has been done that has included both experimental studies as well as molecular dynamics simulations.[2, 8, 11, 14, 16-20] Based on a review of the literature, MetA-SIMS has been performed after deposition of thin layers (0 – 40 nm) of metals that include Au, Ag, and Pt. Monatomic, polyatomic, and cluster PI beams have been used in these studies. Samples have consisted of flat substrates spin coated with a variety of polymers (polystyrene,[8] polycarbonate,[15] polyethylene,[16] polyethyleneimine[9]), dyes (carbocyanine[12]), pharmaceuticals (risperidone[7, 21]), and large molecules (Irganox 1010,[8] triacontane[22]). Although a well-defined theoretical model is still lacking to fully explain the mechanism behind secondary ion yield enhancements in MetA-SIMS, multiple hypotheses, based in experimental studies, have been proposed.[18] For example, enhancement in SIMS signal intensities has only been observed when MetA-SIMS is performed with a monatomic PI (Ga^+, In^+, Ne^+, Ar^+, Kr^+, Xe^+, or Bi^+). When a polyatomic PI is used, e.g., Bi_n^+, SF_6^+, or C_{60}^+, a decrease or negligible enhancement in the SIMS signal intensity is observed.[1, 9, 12, 17, 18, 22-24] These results are consistent with the increased stopping

of a monatomic PI by thin metal films or clusters, with deposition of the PI energy in the near surface region resulting in increased sputter yield and enhanced SIMS signal. In contrast, when C_{60}^+ impinges upon a gold nanoparticle, its energy is partially reflected, and partially applied to break bonds in the Au particles. The remaining energy is insufficient to produce an enhanced SIMS signal.[18] Similar effects appear to be at play for other moderately sized polyatomic primary ions such as Bi_n^+ and SF_6^+.[24] On the other hand, a molecular dynamics simulation showed that a Au_{400}^+ polyatomic primary ion would enhance the SIMS signal by MetA-SIMS.[19]

It has consistently been observed in MetA-SIMS that Au outperforms Ag, which is attributed to the higher atomic mass of Au imparting better stopping power to a PI and leading to better dissipation of the PI energy at a surface.[8, 12, 22] However, this effect may not be so simple. In one study, Pt did not show any enhancement in MetA-SIMS.[8] This result suggests that in addition to its atomic mass, the nature of the metal affects the MetA-SIMS enhancement. The signal enhancement is also fragment specific and varies with the thickness of the metal overlayer. To further complicate the situation, the time gap between metal deposition and SIMS analysis and storage temperature can affect the degree of signal enhancement in MetA-SIMS.[12, 25, 26] All of this suggests slow reorganization of the metal-organic interface. In addition to the increased stopping power of metal layers, diffusion of polymeric species over the top of metallic nanoclusters, modification of the ionization efficiency of the sample that is in contact with the metal, and improved conductivity of the sample (making SIMS analysis of insulating samples possible without the need for a flood gun), are other factors that contribute to SIMS signal enhancement by MetA-SIMS.

Typically, in the MetA-SIMS work reported to date, Au or Ag metal layers have been deposited on a sample surface by thermal evaporation. Metal deposition by sputtering, as reported

in a few initial studies,[12, 21] was abandoned to prevent chemical damage to surfaces by energetic projectiles. Metal layer thicknesses have generally been monitored with a quartz crystal microbalance (QCM) under the assumption that the sticking coefficients of sample surfaces and the quartz crystal will be the same, i.e., both unity,[24] which is rarely the case. Indeed, it has been proposed that the sticking coefficient of some sample surfaces can be far below unity.[14] Of course, if metal film thicknesses are not accurately known, it becomes difficult to draw reliable conclusions regarding their effects on ion yield. The fact that suitable thickness values for metal overlayers reported in the literature range from 4 – 24 nm[1, 9, 17, 18, 22, 27] suggests that this may be the case for at least some of this work. Delcorte et al.[14, 15] clearly understood the importance of obtaining accurate metal overlayer thicknesses in MetA-SIMS. In their work they used Tougaard peak shape analysis of X-ray photoelectron spectroscopy (XPS) signals to determine the amount of gold they had deposited,[28, 29] and scanning electron microscopy (SEM) to understand its morphology. When they compared their XPS results to the predictions from QCM they found that the sticking coefficients for gold on two polymeric surfaces were ca. 0.5.

In this work I carried out MetA-SIMS on a thin film of a polyelectrolyte (polydiallyldimethylammonium chloride, PDADMAC, see Figure 5.1) using a high Z metal that, to the best of my knowledge, has not been previously explored – bismuth (Bi). Bismuth should be of fundamental interest here because, as noted above, a different high Z element, Pt, failed to give a signal enhancement in previous MetA-SIMS experiments, and bismuth clusters are currently employed in many SIMS experiments as PI.

For the other important aspect of this work, I used interference-enhanced spectroscopic ellipsometry (SE)[30] to measure the thicknesses of evaporated Bi films and thereby to calibrate our QCM for Bi deposition. Practically speaking, interference enhancement is just SE on a thick,

transparent substrate, e.g., SE on a silicon wafer with a relatively thick oxide layer (hundreds on nanometers thick). The fundamental reason for performing interference enhancement is to introduce an interference pattern into the ψ and Δ parameters obtained in SE, which ultimately has the effect of breaking the correlation that often exists between film optical constants, thicknesses, and other film parameters. This approach is particularly useful for absorbing thin films like the metal layers used in MetA-SIMS. Other than a substrate with a thick oxide (transparent layer), which is not hard to obtain (I used silicon wafers with ca. 510 nm of thermal oxide on them), the only other requirement for interference enhancement is to perform the SE measurement at more than one angle of incidence. This is not a difficult requirement for a technique that can make a measurement in perhaps a few tens of seconds and is performed in the air.

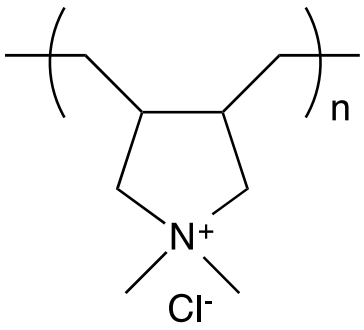

Figure 5.1. Structure of polydiallyldimethylammonium chloride (PDADMAC).

5.3. Experimental

5.3.1. Materials

Silicon wafers, (100) crystallographic orientation, with ca. 510 ± 2 nm of silicon oxide were purchased from WRS Materials, San Jose, CA. Poly(diallyldimethylammonium chloride) (PDADMAC) (MW ~ 100,000 – 200,000, 20% w/v in water) was purchased from Sigma-Aldrich, St. Louis, MO, USA. Stabilized tetrahydrofuran (THF) was obtained from Mallinckrodt, Phillipsburg, NJ. High resistivity (18 MΩ-cm) water used for making solutions and rinsing was obtained from a Milli-Q water system (Millipore, Billerica, MA).

5.3.2. Sample Preparation

Shards of silicon (ca. 1" x 1") were sonicated in methanol, rinsed in methanol, sonicated in water, rinsed in water, and then dried under a stream of N_2. These clean Si(100) substrates were then spin coated using a 1% w/v aqueous solution of PDADMAC at 8000 rpm for 30 s to deposit ca. 45 nm thick PDADMAC layers (determined by SE). Thin films of bismuth (2, 4, 6, 10, and 20 nm) were deposited on both PDADMAC-coated and bare Si(100) substrates in a thermal evaporator. This deposition procedure consisted of watching the output of the QCM in the chamber until the desired film thickness was reached. The shutter separating the Bi source from the samples was then immediately closed. To obtain the best possible results with our chamber, the boat containing the Bi and the samples to be coated should be oriented/positioned in the chamber in the same way in each run.

5.3.3. Time-of-flight Secondary Ion Mass Spectrometry (ToF-SIMS)

ToF-SIMS was performed with a ToF-SIMS IV instrument (ION-TOF, Münster, Germany) equipped with a gallium liquid metal ion source. A 25 KeV Ga^+ ion beam (static primary ion current ~1.2 nA, pulse length 20.3 ns) was rastered over a 500 X 500 μm^2 area at a resolution of 128 X 128 (16384 pixels) with 1 pulse per pixel (pixel width 3.91 μm). For each MetA-SIMS mass spectrum, 140 scans (229.38 s) were collected that account for a total primary ion dose of 1.388 X 10^{11} ions/cm^2, which is well below the static limit of ~10^{13}. No flood gun was used for any of the MetA-SIMS analyses. To study charge compensation of Bi-coated samples, 25 scans (40.96 s, a primary ion dose of 2.5 X 10^{10} ions/cm^2) were collected for each mass spectrum with or without the flood gun operating at a filament current of 2.4 A. Twenty such mass spectra were collected in succession on the same spot to study the evolution of the signal peak intensities with the number of scans, which is equivalent to exposing the sample to a total primary ion dose of 5.0 X 10^{11} ions/cm^2, and is still below the static limit.

5.3.4. Spectroscopic Ellipsometry

Variable angle spectroscopic ellipsometry (VASE) was performed using an M-2000D ellipsometer at four angles of incidence (45˚, 55˚, 65˚, and 75˚) for a beam of light composed of wavelengths from ca. 200 – 1000 nm (see section 1.2.3). The resulting data were analyzed with the WVASE32 (Version: 3.812) software (J. A. Woollam Co., Lincoln, NE). Refer to section 1.2.3 for detailed description of working of spectroscopic ellipsometry (SE).

5.4. Results and Discussion

This section is divided into two parts. The first deals with the calibration of the QCM in the deposition chamber by interference enhanced SE. The second describes the MetA-SIMS signal enhancements provided by Bi.

5.4.1. Determination of Bi Film Thicknesses on the Silicon Substrate and on PDADMAC Layers

Bi film thicknesses were conveniently estimated using a quartz crystal microbalance (QCM) in the deposition system. Because the response of a QCM depends on its position in a chamber, it must be calibrated. Accordingly, 20 and 40 nm films of Bi (by QCM) were deposited onto bare silicon and PDADMAC-coated silicon. The resulting film thicknesses were then measured by SE.

SE is a model-based technique, and the models shown in Figure 5.2 were used to characterize the substrate and then determine the thicknesses of Bi and PDADMAC layers on it. All SE measurements were performed in interference enhancement mode, and Figure 5.2a shows the model for the thick-oxide substrate used for this purpose. This model consists of a thick, opaque silicon base layer, an Si/SiO_2 interface layer,[30] and a thick oxide layer. The optical constants in the instrument software were used for all of these layers, so the only unknown in this model was the thickness of the thick oxide layer. In a typical example, this oxide thickness was found in a 'normal fit' to be 512.6 nm with a reasonable MSE of 6.8.

Figure 5.2b gives the model for the PDADMAC thin film on the thick oxide substrate. This film was prepared by spin coating a 1% w/v solution of aqueous PDADMAC for 30 s at 8000 rpm

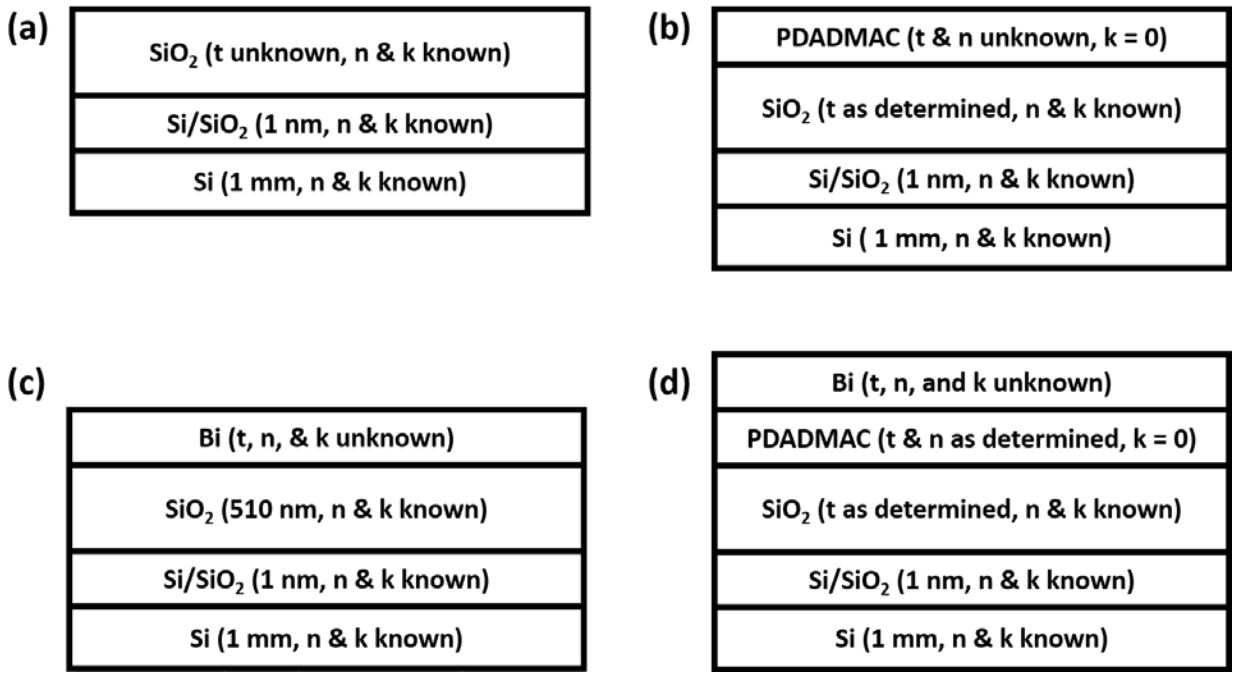

Figure 5.2. SE models used to determine the optical properties/thicknesses of (a) the thick oxide silicon/silica substrate, (b) a PDADMAC layer on the thick oxide silicon/silica substrate, (c) a Bi layer on the thick oxide silicon/silica substrate, and (d) a Bi layer on a PDADMAC film on the thick oxide silicon/silica substrate.

onto a silicon support. In this model, all of the parameters for the clean, thick oxide substrate were fixed to the values found by SE for the clean surface. The PDADMAC layer was then described using a Cauchy model, which describes the index of refraction, n(λ), of a transparent dielectric as a truncated, inverse power series governed by the values of three constants: A, B, and C (see Equation 2).

$$n(\lambda) = A + \frac{B}{\lambda^2} + \frac{C}{\lambda^3} \qquad (2)$$

In this fit, the constant C did not affect the MSE significantly and so it was set to zero. In a representative example, with A and B in Equation 2 allowed to vary, the thickness for the PDADMAC layer was determined to be 45.8 nm (MSE 7.1).

While a thin film of Bi (Figure 5.2c) has more unknowns to model (index of refraction, n(λ), thickness, *and* extinction coefficient k(λ)) compared to only n(λ) and thickness for the PDADMAC films, the interference enhancement of the thick oxide substrate allows all of these parameters to be determined with careful modeling. The general approach I used to tackle this problem was as follows. The film thickness was first set to the value found by QCM, and the optical constants of Bi were approximated as those of another metal (silver, taken from the instrument software). With the thickness of the film fixed, a point-by-point fit of the optical constants was performed, and in a second step, the optical constants and film thickness were allowed to vary. Fits run in this manner showed good MSE values. Thin films of Bi on PDADMAC on silicon (Figure 5.2d) were modeled sequentially using the same procedures outlined herein, i.e., the thickness and optical constants of an underlying layer would be determined and fixed before the thickness and optical constants of the next layer would be determined.

Measuring the optical constants and thicknesses of very thin films can be a challenge for SE. For example, the parameters of the Cauchy model and the thicknesses it predicts are often correlated for films thinner than 10 nm. When the Bi films were thinner than 10 nm (by SE), the MSE values for the SE models we used for it (Figure 5.2) rose substantially. These results may also suggest that the model for the films is incomplete. However, a 'better' model would almost certainly require the addition of additional model parameters, which creates its own issues vis-à-vis the believability of the results. Accordingly, I felt that the calibration of the QCM in the deposition chamber over a range of thicknesses where the ellipsometry was giving reasonable results would be important to measure/predict the true thicknesses of our thinner Bi films. Table 5.1 shows the results of these efforts to calibrate our QCM. When either 20 nm or 40 nm of Bi (by QCM) was deposited onto the silicon substrate or onto PDADMAC, the result was essentially the same: SE registered a Bi film thickness that was half as great as the thickness found by QCM. To check the accuracy of SE, different thicknesses of bismuth (10 – 100 nm based on the QCM readings) were deposited onto a piece of a silicon wafer on which a line had been drawn using a Sharpie marker. The rinsing of these bismuth coated silicon wafers with copious amounts of THF led to the dissolution/removal of the line drawn with the Sharpie marker and removal of the bismuth in that area, which created a step whose height could be measured by atomic force microscopy (AFM). Although, unlike ellipsometry AFM did not show exactly the half values of thicknesses of the bismuth layers, the measured values were close to it (see Table 5.1). The discrepancy between AFM and SE readings could be attributed to some extent to the mechanical nature of the shutter in the evaporator, the position of the sample in the thermal evaporator, the orientation of the tungsten boat with respect to the sample in the evaporator, and the crude rinsing procedure employed.

Sample	QCM Thickness of Bi	AFM Thickness of Bi	SE Thickness of Bi	SE MSE
Si/SiO_2	40 nm	-	20.84 nm	7.09
Si/SiO_2	20nm	-	10.92 nm	12.26
Si/SiO_2/PDADMAC	40 nm	-	19.89 nm	8.97
Si/SiO_2/PDADMAC	20 nm	-	10.27 nm	12.41
Si/SiO_2	50 nm	30 .0nm		
Si/SiO_2	50 nm	22.3 nm		
Si/SiO_2	10 nm	7.2 nm		
Si/SiO_2	100 nm	44.0nm		

Table 5.1. Thicknesses of bismuth layer measured by quartz crystal microbalance and spectroscopic ellipsometry.

Uniqueness testing is commonly performed in SE to check for correlation between parameters in a model. The SE models corresponding to 10 – 20 nm (by SE) of Bi on bare and PDADMAC-coated Si(100) were evaluated in this way (see Figures 5.2b and d, and 5.3). Here, the thickness of the Bi film was fixed at a series of values that ranged around its optimal value, and the remaining parameters in the model were allowed to vary. The MSE for each fit was then plotted as a function of the (fixed) thickness of the Bi film. The general upward, parabolic shapes of the resulting curves confirmed the uniquenesses of the ellipsometric models, i.e., that the model parameters were uncorrelated.

5.4.2. MetA-SIMS Signal Enhancements Provided by Bi

ToF-SIMS was performed on bare and PDADMAC-coated Si(100) shards that were covered with 0, 2, 4, 6, 10, or 20 nm (by SE) of evaporated Bi. To better compare and understand these spectra, a careful, peak-by-peak, comparison of the ToF-SIMS spectra of the surfaces coated with 0 and 6 nm of Bi was undertaken. From this analysis, 24 peaks were identified that appeared to (i) be attributable to the PDADMAC layer, and (ii) show MetA-SIMS enhancement in the Bi-coated PDADMAC surface. The masses and tentative assignments of these signals are given in Table 5.2. Figure 5.4 shows the ToF-SIMS spectra from two of these fragments (m/z ~ 333 ($C_{23}H_{29}N_2^+$) and m/z ~ 279 ($C_{18}H_{35}N_2^+$)) that were obtained under different conditions. In particular, Figure 5.4a shows that intense signals were obtained from a Si(100)/PDADMAC/Bi(6 nm) sample. Figure 5.4b then shows that much smaller signals are produced from a Si(100)/PDADMAC sample (no Bi). Finally, Figure 5.4c – d shows the same spectral regions from bare Si(100) and Si(100)/Bi(6 nm) samples. The m/z ~ 333 and m/z ~ 279 signals in question here do not appear to be present in these spectra.

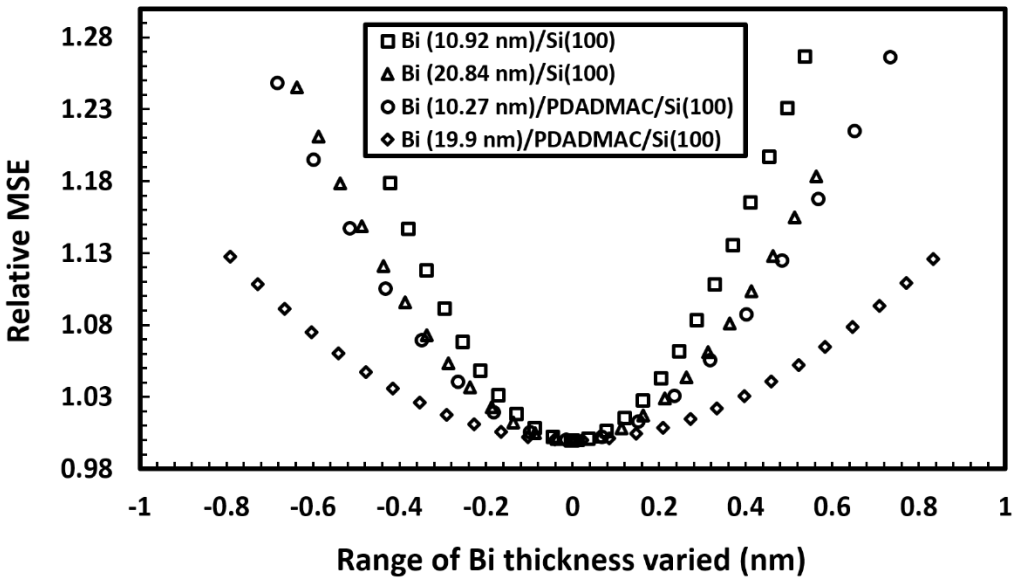

Figure 5.3. Results of SE uniqueness testing on thick oxide silicon/silica substrates coated with Bi or PDADMAC and Bi.

		MetA-SIMS Enhancement		
m/z	Chemical Formula	4 nm Bi	6 nm Bi	10 nm Bi
42.059	$C_2H_4N^+$	4.31	6.31	7.52
58.096	$C_3H_8N^+$	11.66	19.14	17.23
68.094	$C_4H_4N^+$	6.30	9.89	12.80
82.1	$C_5H_8N^+$	7.87	12.19	10.93
84.116	$C_5H_{10}N^+$	13.91	23.95	44.83
94.105	$C_6H_8N^+$	7.32	11.82	8.85
96.121	$C_6H_{10}N^+$	10.29	17.40	13.11
98.138	$C_6H_{12}N^+$	12.06	18.55	14.28
110.14	$C_7H_{12}N^+$	13.35	23.04	24.17
112.157	$C_7H_{14}N^+$	16.25	27.70	21.57
126.173	$C_8H_{16}N^+$	47.14	84.87	202.52
127.175	$C_8H_{17}N^+$	43.98	78.75	181.39
128.189	$C_8H_{18}N^+$	36.33	59.71	100.23
140.2	$C_9H_{18}N^+$	22.99	39.02	33.18
152.201	$C_{10}H_{18}N^+$	16.43	26.79	13.63
154.215	$C_{10}H_{20}N^+$	24.76	44.59	10.76
162.167	$C_{11}H_{16}N^+$	38.56	67.03	91.09
166.22	$C_{11}H_{20}N^+$	26.20	41.31	29.09
168.239	$C_{11}H_{22}N^+$	33.73	56.13	62.62
169.241	$C_{11}H_{23}N^+$	37.91	63.71	68.76

184.232	$C_{12}H_{26}N^+$	53.48	86.56	75.64
230.146	$C_{17}H_{12}N^+$	192.16	346.25	1218.85
279.357	$C_{18}H_{35}N_2^+$	37.76	52.61	12.92
333.333	$C_{23}H_{29}N_2^+$	335.73	688.85	1539.00

Table 5.2. Ions from PDADMAC that showed significant signal enhancement in Bi MetA-SIMS with possible molecular assignments.

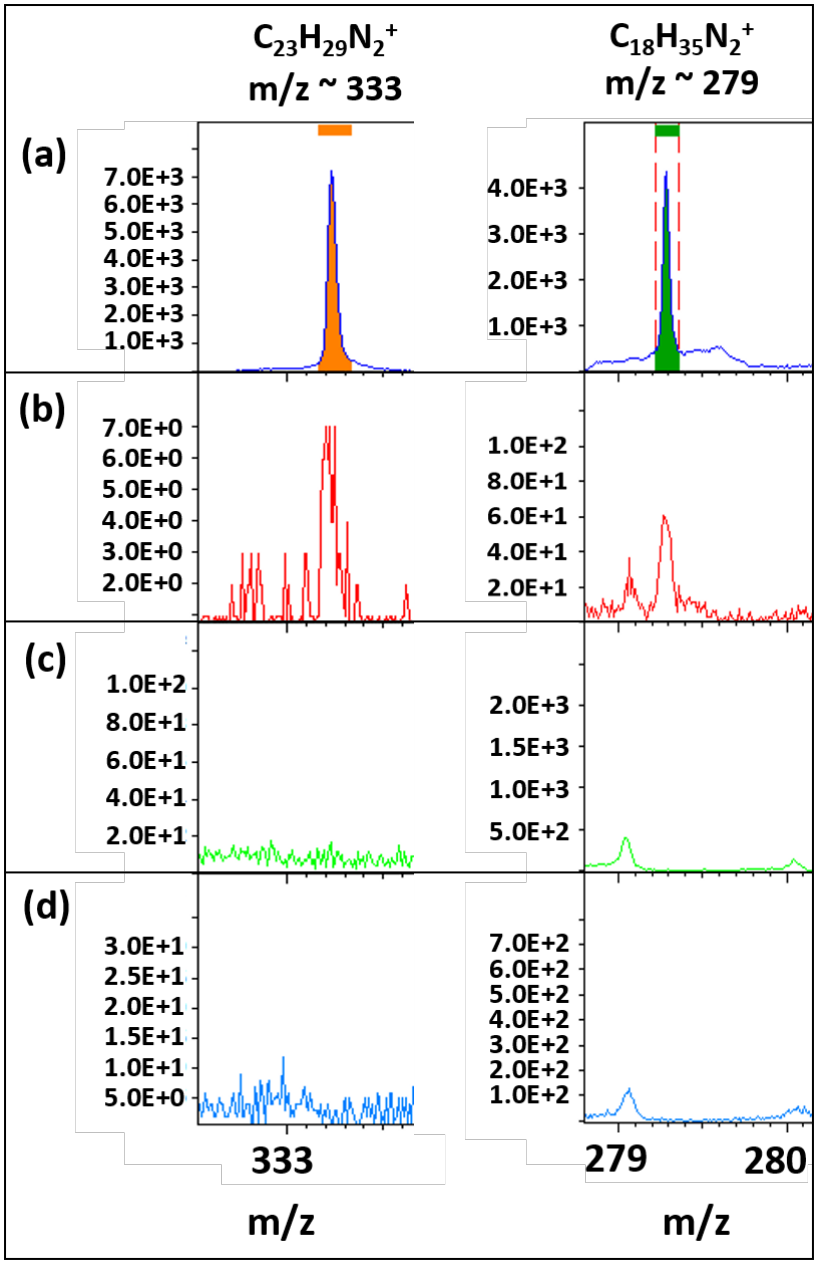

Figure 5.4. ToF-SIMS signals assigned to $C_{23}H_{29}N_2^+$ (m/z 333) (left column) and $C_{18}H_{35}N_2^+$ (m/z 279) (right column) for (a) Si(100) spin coated with PDADMAC and 6 nm of Bi, (b) Si(100) spin coated with PDADMAC, (c) bare Si(100), and (d) Si(100) coated with 6 nm of Bi.

The MetA-SIMS enhancement factors for the 24 signals identified in Table 2 were calculated by dividing the areas of the signals obtained from the Bi-coated PDADMAC samples by the corresponding signals obtained from the uncoated PDADMAC samples. Figure 5.5a shows the MetA-SIMS enhancement factors for 19 out of the 24 signals identified in Table 1. A maximum signal enhancement of ca. 10 - 100 takes place for these fragments for 6 – 10 nm of Bi. Figure 5.5b shows the enhancement factors of the remaining 5 fragments as a function of Bi overlayer thickness. For two of these fragments, enhancement factors of over 1000 were observed.

In the analysis of the PDADMAC fragments in Table 5.2, it was noticed that the heavier m/z fragments seemed to show higher MetA-SIMS enhancements. The plot of MetA-SIMS enhancement vs. fragment mass in Figure 5.5c confirms this general trend. This result is significant because higher m/z fragments tend to be more characteristic of materials. Finally, while this work is focused on the signal enhancements that can be obtained via Bi MetA-SIMS, it was noted that PDADMAC samples coated with 2 nm of Bi actually showed small decreases in their signal intensities. This may be because 2 nm of Bi has poor stopping power and thus only serves to inhibit ion formation/release from surfaces.

The relatively thick PDADMAC layer (~45 nm) spin-coated onto Si(100) should be insulating, and all of the silicon substrates used in this study had a thick (ca. 510 nm) layer of oxide on them. Accordingly, charge compensation was expected to be necessary for a good analysis of these PDADMAC films. Figure 5.6a shows the results from analyzing this film when no charge compensation was employed. Here, 20 series of mass spectra were collected from a single spot on the sample. The total number of ions that irradiated the surface during these analyses was ca. 5 X $10^{11}/cm^2$, which should put this overall analysis well within the static limit. Charging appears to be taking place on these samples, as there is a steady decrease in the intensities of the various ions

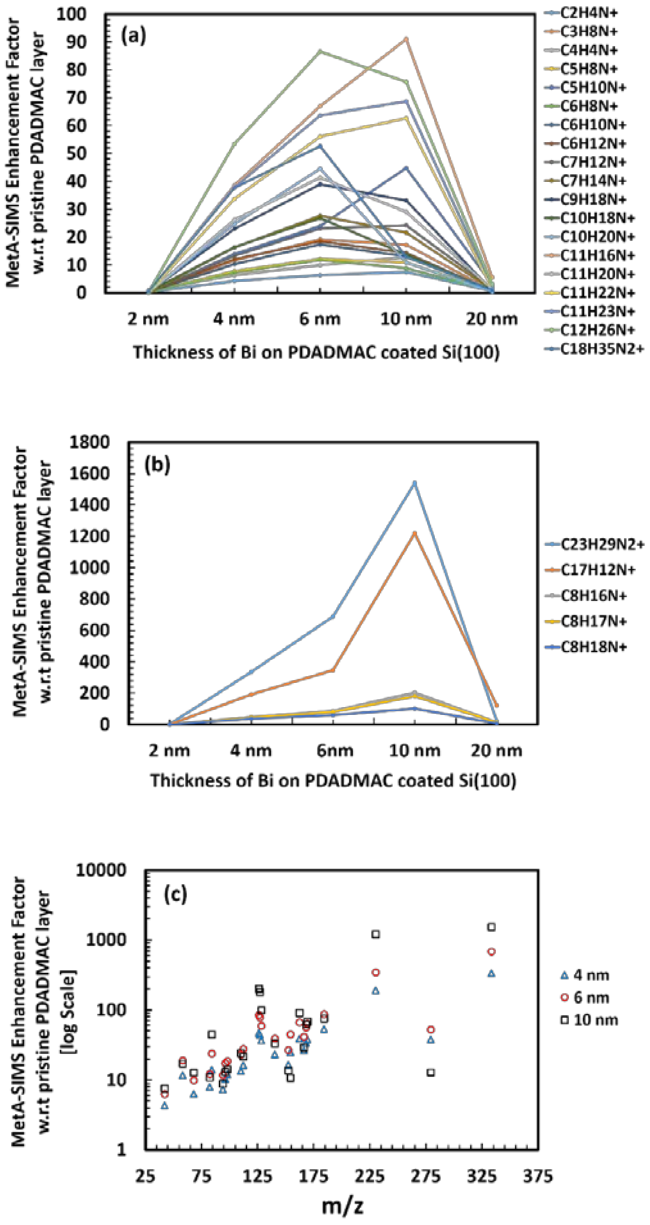

Figure 5.5. (a) MetA-SIMS enhancement factors in the range of ca. 10 – 100 for various ions from a PDADMAC sample coated with different thicknesses of bismuth, (b) MetA-SIMS enhancement factors in the range of ca. 100 – 1600 for various ions from a PDADMAC sample coated with different thicknesses of bismuth, and (c) Plot of MetA-SIMS enhancement factors vs. ion m/z value.

as a function of sample irradiance. Figure 5.6b shows the same analysis with charge compensation (an electron flood gun). While the signals are by no means constant in every case, they are more consistent than those that were obtained without charge compensation, and most of the signals do not change by more than ca. ± 20% over the course of the analysis. Figure 5.6c shows the evolution of signals that were obtained from PDADMAC coated with 6 nm of Bi without charge compensation. The most consistent signals are obtained here. Finally, Figure 5.6d shows the analysis of the same PDADMAC/Bi(6 nm) sample with charge compensation. While the signals are certainly more consistent here than in Figure 5.6b, they are not as good as those obtained in Figure 5.6c. Thus, charge compensation is (i) strongly advised for insulating PDADMAC samples, although it is not quite as effective as might be hoped, and (ii) discouraged for Bi-coated PDADMAC samples because the Bi on them already appears to be conductive so any additional charge compensation only appears to perturb the samples. This general approach of coating insulators with Bi may prove useful for the analysis of other insulators.

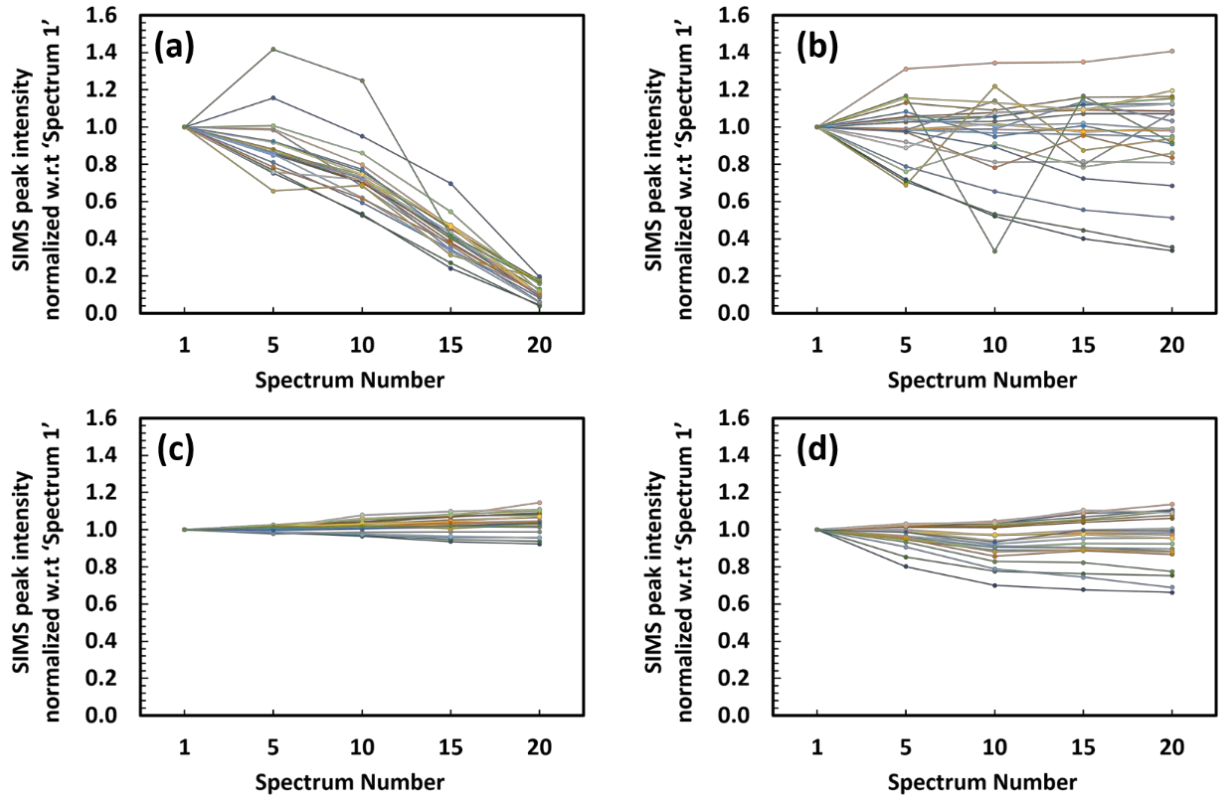

Figure 5.6. The evolution of positive ion mode ToF-SIMS signals (see Table 1) with time for PDADMAC polymer while the flood gun is (a) off, (b) on. The evolution of positive ion mode meta-SIMS signals (see Table 1) with time for PDADMAC polymer coated with 6 nm of bismuth layer while the flood gun is (c) off, (d) on.

5.5. Acknowledgements

A special thanks to Nathan Havercroft, Vice-President/ General Manager (ION-TOF USA) and Ron Synowicki, Application Engineer (J.A. Woollam Co., Inc. Lincoln, NE, USA) for their help with off campus access to SurfaceLab 6 and WVASE32 data analysis software. We appreciate very much the outstanding customer service of both of these organizations.

5.6. References

1. Delcorte, A.; Yunus, S.; Wehbe, N.; Nieuwjaer, N.; Poleunis, C.; Felten, A.; Houssiau, L.; Pireaux, J.-J.; Bertrand, P. *Anal. Chem.* **2007,** *79* (10), 3673-3689.

2. Touboul, D.; Kollmer, F.; Niehuis, E.; Brunelle, A.; Laprévote, O. *J. Am. Soc. Mass Spectrom.* **2005,** *16* (10), 1608-1618.

3. Weibel, D.; Wong, S.; Lockyer, N.; Blenkinsopp, P.; Hill, R.; Vickerman, J. C. *Anal. Chem.* **2003,** *75* (7), 1754-1764.

4. Davies, N.; Weibel, D.; Blenkinsopp, P.; Lockyer, N.; Hill, R.; Vickerman, J. *Appl. Surf. Sci.* **2003,** *203*, 223-227.

5. Wu, K. J.; Odom, R. W. *Anal. Chem.* **1996,** *68* (5), 873-882.

6. Lua, Y.-Y.; Yang, L.; Pew, C. A.; Zhang, F.; Fillmore, W. J. J.; Bronson, R. T.; Sathyapalan, A.; Savage, P. B.; Whittaker, J. D.; Davis, R. C. *J. Am. Soc. Mass Spectrom.* **2005,** *16* (10), 1575-1582.

7. Grade, H.; Winograd, N.; Cooks, R. G. *J.Am.Chem.Soc.* **1977,** *99* (23), 7725-7726.

8. Delcorte, A.; Bertrand, P. *Appl. Surf. Sci.* **2004,** *231*, 250-255.

9. Heile, A.; Muhmann, C.; Lipinsky, D.; Arlinghaus, H. *Surf. Interface Anal.* **2011,** *43* (1-2), 20-23.

10. Inoue, M.; Murase, A. *Surf. Interface Anal.* **2005,** *37* (12), 1111-1114.

11. Becker, N.; Wirtz, T. *Anal. Chem.* **2012,** *84* (14), 5920-5924.

12. Adriaensen, L.; Vangaever, F.; Gijbels, R. *Anal. Chem.* **2004,** *76* (22), 6777-6785.

13. Gilmore, I.; Seah, M. *Appl. Surf. Sci.* **2002,** *187* (1), 89-100.

14. Nittler, L.; Delcorte, A.; Bertrand, P.; Migeon, H. N. *Surf. Interface Anal.* **2013,** *45* (1), 18-21.

15. Nittler, L.; Delcorte, A.; Bertrand, P.; Migeon, H. N. *Surf. Interface Anal.* **2011,** *43* (1-2), 103-106.

16. Restrepo, O. A.; Delcorte, A. *Surf. Interface Anal.* **2011,** *43* (1-2), 70-73.

17. Wehbe, N.; Mouhib, T.; Prabhakaran, A.; Bertrand, P.; Delcorte, A. *J. Am. Soc. Mass Spectrom.* **2009,** *20* (12), 2294-2303.

18. Restrepo, O.; Prabhakaran, A.; Hamraoui, K.; Wehbe, N.; Yunus, S.; Bertrand, P.; Delcorte, A. *Surf. Interface Anal.* **2010,** *42* (6-7), 1030-1034.

19. Restrepo, O. A.; Delcorte, A. *J. Phys. Chem. C* **2011,** *115* (26), 12751-12759.

20. Delcorte, A.; van Hoecke, E.; Restrepo, O. **2013,** *303*, 174-178.

21. Adriaensen, L.; Vangaever, F.; Lenaerts, J.; Gijbels, R. *Appl. Surf. Sci.* **2006,** *252* (19), 6628-6631.

22. Wehbe, N.; Heile, A.; Arlinghaus, H. F.; Bertrand, P.; Delcorte, A. *Anal. Chem.* **2008,** *80* (16), 6235-6244.

23. Heile, A.; Lipinsky, D.; Wehbe, N.; Delcorte, A.; Bertrand, P.; Felten, A.; Houssiau, L.; Pireaux, J.-J.; De Mondt, R.; Van Vaeck, L. *Appl. Surf. Sci.* **2008,** *255* (4), 941-943.

24. Heile, A.; Lipinsky, D.; Wehbe, N.; Delcorte, A.; Bertrand, P.; Felten, A.; Houssiau, L.; Pireaux, J. J.; De Mondt, R.; Van Royen, P. *Surf. Interface Anal.* **2008,** *40* (3-4), 538-542.

25. De Mondt, R.; Adriaensen, L.; Vangaever, F.; Lenaerts, J.; Van Vaeck, L.; Gijbels, R. *Appl. Surf. Sci.* **2006,** *252* (19), 6652-6655.

26. De Mondt, R.; Van Vaeck, L.; Lenaerts, J. *J. Am. Soc. Mass Spectrom.* **2007,** *18* (3), 382-384.

27. Prabhakaran, A.; Yunus, S.; Wehbe, N.; Bertrand, P.; Delcorte, A. *Surf. Interface Anal.* **2011,** *43* (1-2), 74-77.

28. Tougaard, S.; Hansen, H. *Surf. Interface Anal.* **1989,** *14* (11), 730-738.

29. Tougaard, S. *J. Vac. Sci. Technol., A* **1996,** *14* (3), 1415-1423.

30. Hilfiker, J. N.; Singh, N.; Tiwald, T.; Convey, D.; Smith, S. M.; Baker, J. H.; Tompkins, H. G. *Thin Solid Films* **2008,** *516* (22), 7979-7989.

Chapter 6: Conclusions and Future Work

6.1. Conclusions

In my PhD research work I focused on the construction and characterization of complex molecular structures with desired chemical and mechanical properties on planar gold, silicon dioxide, and aluminum surfaces. The molecular constructs were assembled using a combination of different surface chemical reactions in a sequential manner. Each chemical modification step was monitored/optimized with the help of various surface analytical techniques – X-ray photoelectron spectroscopy (XPS), time-of-flight secondary ion mass spectrometry (ToF-SIMS), ellipsometry, contact angle goniometry, and atomic force microscopy. I demonstrated successful functionalization of gold surfaces by dithiol self-assembled monolayers (SAMs) followed by a photochemical thiol-ene reaction with 1,2-polybutadiene (PBd). The PBd terminated gold surfaces could further be modified with thiolated chemical moieties e.g. DNA-SH and a perfluoroalkanethiol. The final assemblies showed higher chemical stability when exposed to air and light compared to the more commonly employed alkylthiol SAMs. Silicon dioxide surfaces were coated with a tunable hydrophobic thin film that was prepared by application of thermally cross-linked polyelectrolyte multilayers, bioconjugate chemistry, and thiol-ene chemistry. The hydrophobic film demonstrated excellent chemical and mechanical stability. The hydrophilic/hydrophobic contrast of the final assembly could be tuned in a facile manner by varying the extent of heat treatment during cross-linking of the polyelectrolyte layers and did not require tedious patterning steps. In the part of my work that focused on surface characterization, a sophisticated XPS and ToF-SIMS study was carried out to understand the effects of a downstream fluorinated plasma on aluminum surfaces. The aluminum surfaces with/out a corrosion protective coating of nitrilotris(methylene)triphosphonic acid were used for this study. The techniques

confirmed significant damage to the corrosion protective coating and formation of aluminum oxyfluoride within the first few seconds of the plasma treatment. It was discovered that corrosion prone aluminum oxyfluoride could be easily converted back to aluminum oxide by heating in the presence of air. In a separate effort, metal-assisted secondary ion mass spectrometry (MetA-SIMS) was performed for the first time using thin layers of bismuth metal on poly(diallyldimethylammonium) chloride coated silicon dioxide surfaces. An enhancement by a factor of 10-1600 was observed in positive ion mode SIMS signal intensities. There was no need for charge compensation on Bi coated surfaces. Interference enhanced spectroscopic ellipsometry was successfully incorporated for the first time to accurately measure the thickness of bismuth metal layers directly over the sample surface. I believe that my research findings are an important contribution to surface science.

6.2. Future Recommendations

In the research work presented in this dissertation, multiple surface chemical reactions were employed. Among them self-assembled monolayers of thiols on gold, the layer-by-layer deposition of polyelectrolytes, and a reaction with Traut's reagent demonstrated excellent consistency and reproducibility. On the other hand, executing thiol-ene chemistry was a challenging task. Although, a great deal of literature is available on thiol-ene chemistry that is performed in conventional organic chemistry laboratory, the claimed click nature and high yields of these reactions were not evident when performed on surfaces. These results raise the need for more in depth experimentation on this topic. It would be an informative study to determine the yield of the thiol-ene reaction of a 1,2-polybutadiene coated surface with a thiolated molecule vs. a thiol terminated surface reacted with 1,2-polybutadiene. The reaction yields could be studied under

irradiation by different wavelengths of light (254 nm, 365 nm, and 550 nm) for different durations of time. The hydrophobic coating discussed in Chapter 3 demonstrated interesting water droplet pinning and flow properties that could be controlled by the extent of thermal cross-linking. It would be interesting to further explore this avenue by conducting a more thorough experimentation to precisely control the flow of water on the surface of these thin films. This could have direct application in the field of microfluidics. In addition, introduction and experimentation with a roughness parameter is another logical direction to further modify the hydrophobic profile of the prepared coating. The optimization of the thiol-ene reaction to give high yields in combination with the introduction of roughness can lead to development of a super-hydrophobic surface with unique flow properties.

In consideration of the available literature on MetA-SIMS, I have reported some new, interesting, and to some extent contrasting results in Chapter 5 of my dissertation. These results are encouraging, but suggest that more detailed studies should be undertaken. The 10 – 20 nm thick bismuth layers deposited on bare and polymer coated silicon substrates should be analyzed by scanning electron microscopy and atomic force microscopy. The cross-section of bismuth layers should also be studied with focused ion beam and scanning electron microscopy. These results would shed some light on the porosity and growth profile of bismuth. In addition, the oxidation of the bismuth layer should be monitored with X-ray photoelectron spectroscopy. All of this information could then be applied together to improve the accuracy of ellipsometric modeling. It is expected that the bismuth layers used in this work were oxidized to a certain extent as they were exposed to the atmosphere. In addition to quantifying the extent of bismuth oxidation by XPS, it would be useful to find out if this oxidation plays any role in the observed MetA-SIMS signal enhancement. The introduction of oxygen due to oxidation of bismuth could also improve

the secondary ion yield in negative ion mode ToF-SIMS spectra. To understand these possibilities, a comparative MetA-SIMS study should be performed with metallic and oxidized bismuth layers. In addition, a similar MetA-SIMS study could also be performed with other metals, e.g., Au, Ag, and Pt. These finding would be very helpful to further understand the mechanism of signal enhancement in MetA-SIMS.

Appendix A: Regression of Experimental Electron Binding Energies with Matrix Algebra. Semiempirical Predictions of Bohr's Theory to Multielectron Atoms

Note: The work presented in this appendix will be submitted to an educational journal in future.

A.1. Abstract

Bohr's atomic theory in 1913 gave a new dimension to our understanding of atomic structure. In particular, he predicted a Z^2/n^2 dependence to electron binding energies, where Z is the atomic number of the atom and n is the principal quantum number of the electron in question. Here I investigate, in a semiempirical sense, the Z^2 dependence of the electron binding energies in multielectron atoms. I fit experimental binding energies to three models: the Bohr equation, AZ^2, and $AZ^2 + BZ + C$. I introduce a matrix algebra formalism for performing the regressions. Because of its simplicity and usefulness in other fitting problems, I have found that an understanding of this matrix algebra tool is valuable for advanced undergraduate and graduate students in chemistry. The application of matrix algebra to this particular problem also strengthens students' understanding of Bohr Theory.

A.2. Introduction

In 1913,[1] Niels Bohr proposed "the first really successful theory of atomic structure".[2] This new model overcame the shortcomings of the models of his day, which included, among quite a few others, Thomson's plum pudding model, Nagaoka's saturnian model, and Rutherford's nuclear atom.[2] Based on the assumption of the quantization of electron orbital angular momentum,

his model accurately predicts the electron binding energies of one-electron atoms, e.g., H, He^{+}, Li^{2+}, etc., as:

(1) $E_n = -13.6\ Z^2/n^2$ eV

Where Z is the atomic number of the atom and n is the principal quantum number of the electron. As noted, Bohr's model was a huge step forward in our understanding of the atom. Indeed, in their discussion of his contribution in their classic book on quantum mechanics, Pauling and Wilson wrote: "The successful effort of Bohr in 1913, despite its simplicity, may well be considered the greatest single step in the development of the theory of atomic structure."[3] Bohr received the Nobel Prize in 1922 for his monumental contribution.

While the Bohr model was a great step forward, it has its shortcomings, not the least of which is that it breaks down for atoms that contain more than one electron. It has, therefore, been supplanted by the more complete theory of quantum mechanics. Nevertheless, Bohr theory remains valuable for a variety of reasons. It serves as an important pedagogical tool at many levels of chemistry and physics, especially general chemistry, helping students understand fundamental concepts, such as the existence of quantized energy levels in atoms and the electronic transitions between them. Bohr theory also allows more advanced students of science and engineering to calculate, in a rather straightforward way, properties of atoms and materials that often prove to be fairly reasonable estimates for their actual behavior.[4] Finally, as noted, it is of historical importance.

In this contribution I examine one of the predictions of Bohr theory, which is the Z^2 dependence of the binding energies of electrons in atoms. I explore this prediction, in a semiempirical way, for atoms with multiple electrons. In particular, I fit the binding energies of core electrons from a series of atoms and for two different values of 'n' using Bohr's theory, and

to AZ^2 and $AZ^2 + BZ + C$, where I use matrix algebra to perform these regressions. I have found that this matrix algebra approach is powerful for students to understand because it applies generally to many other data fitting problems. The exercise of comparing the binding energies of atoms to the predictions of Bohr's theory and fitting them to Z^2-type polynomials will also strengthen students' understanding of Bohr theory.

Some matrix algebra will be introduced in the examples below. It is believed that most advanced undergraduates in chemistry will have had enough matrix algebra to follow them. If, however, the reader is unable to follow what is presented here, he/she may wish to consult a textbook on linear algebra.

Finally, this document is deliberately written in a conversational way in the hope that it will be readable/accessible to undergraduate and graduate students interested in this topic.

A.3. Solving a Simple Problem with Matrix Algebra

I'll first demonstrate the use of matrix algebra to find the intercept of the following two lines:

(2) $y = x + 1$

(3) $y = -x + 1$

Clearly, I am looking for the values of x and y at their crossing point. I begin by rewriting Equations 2 and 3 as:

(4) $x - y = -1$

(5) $x + y = 1$

I then reformulate Equations 4 and 5 as a single matrix algebra problem:

(6) $$\begin{pmatrix} 1 & -1 \\ 1 & 1 \end{pmatrix} \begin{pmatrix} x \\ y \end{pmatrix} = \begin{pmatrix} -1 \\ 1 \end{pmatrix}$$

where the coefficients of x and y in Equations 4 and 5 have been represented as the matrix:

(7) $$\begin{pmatrix} 1 & -1 \\ 1 & 1 \end{pmatrix}$$

One method of solving Equation 6 for x and y is to left multiply both sides of it by the inverse of the matrix in Equation 7. I won't worry here about how to find this inverse. There are mathematical methods to find it by hand, and of course there are programs like Excel, Matlab, and Mathematica that will, in general, determine it much more quickly. Thus, using one of these tools I find the inverse of Equation 7 to be:

(8) $$\begin{pmatrix} 0.5 & 0.5 \\ -0.5 & 0.5 \end{pmatrix}$$

Left multiplying both sides of Equation 6 by this matrix gives:

(9) $$\begin{pmatrix} 0.5 & 0.5 \\ -0.5 & 0.5 \end{pmatrix}\begin{pmatrix} 1 & -1 \\ 1 & 1 \end{pmatrix}\begin{pmatrix} x \\ y \end{pmatrix} = \begin{pmatrix} 0.5 & 0.5 \\ -0.5 & 0.5 \end{pmatrix}\begin{pmatrix} -1 \\ 1 \end{pmatrix}$$

which upon simplification leaves me with the identity matrix on the left:

(10) $$\begin{pmatrix} 1 & 0 \\ 0 & 1 \end{pmatrix}\begin{pmatrix} x \\ y \end{pmatrix} = \begin{pmatrix} 0 \\ 1 \end{pmatrix}$$

which of course reduces to:

(11) $$\begin{pmatrix} x \\ y \end{pmatrix} = \begin{pmatrix} 0 \\ 1 \end{pmatrix}$$

Equation 11 tells me that x = 0 and y = 1, which satisfy Equations 2 and 3, i.e., you may wish to plug these values into these equations to convince yourself that this is the case.

A.4. Fitting a Series of Data Points to a Straight Line using Matrix Algebra

Let's now solve the more complicated, and interesting, problem of fitting a set of points to a straight line. Let's take the points: (0, 0.1), (0.9, 1.1), (2.2, 1.9), (3.0, 2.7), and (4.1, 4.2). They're plotted in Figure A.1. Now, it turns out that I can model this problem as follows:

(12) $y_i = mx_i + b$

where each x_i and y_i in Equation 12 are a pair of the (x, y) points above, and m and b are the slope and intercept of the line that best fits these points. Thus, I can write:

(13) $0.1 = m*0 + b$

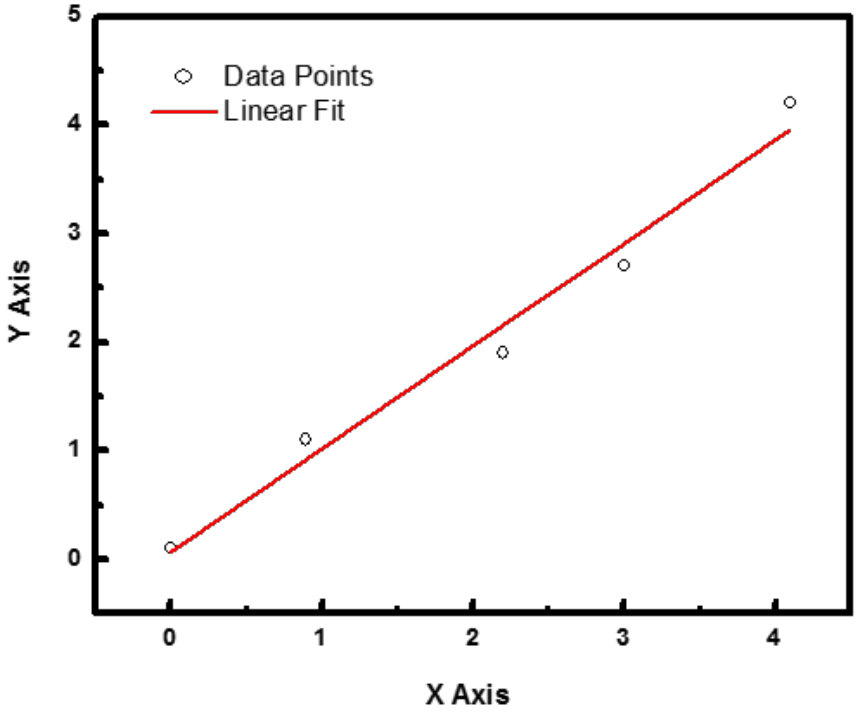

Figure A.1. Graph of the points: (0, 0.1), (0.9, 1.1), (2.2, 1.9), (3.0, 2.7), and (4.1, 4.2), and the linear fit to them.

(14) $1.1 = m*0.9 + b$

(15) $1.9 = m*2.2 + b$

(16) $2.7 = m*3.0 + b$

(17) $4.2 = m*4.1 + b$

I now rewrite all five of these equations as a single matrix algebra problem:

(18) $$\begin{pmatrix} 0.1 \\ 1.1 \\ 1.9 \\ 2.7 \\ 4.2 \end{pmatrix} = \begin{pmatrix} 0 & 1 \\ 0.9 & 1 \\ 2.2 & 1 \\ 3.0 & 1 \\ 4.1 & 1 \end{pmatrix} \begin{pmatrix} m \\ b \end{pmatrix}$$

Ideally, to solve this problem I would do what I did before. I would find the inverse of the 5 x 2 matrix on the right side of Equation 18 and left multiply both sides of Equation 18 by this matrix. But there's a significant problem here. Only square matrices have inverses. But, there is a simple solution to this problem. First, let me rewrite Equation 18 in an abbreviated fashion as follows:

(19) $Y = XM$

where Y, X, and M represent the 5 x 1, 5 x 2, and 2 x 1 matrices in Equation 18, respectively.

Now as it is known that any time two matrices are multiplied together, the number of columns in the matrix on the left must be equal to the number of rows in the matrix on the right. This was the case in Equation 6 – I multiplied a 2 x 2 matrix by a 2 x 1 matrix. There are two columns in the first matrix and two rows in the second one. Notice that when I multiplied these two matrices together we got a 2 x 1 matrix. That is, the second '2' in the first set of dimensions and the first '2' in the second set of dimensions needed to be the same, and then 'disappeared' to leave the outer numbers: 2 x 1. The same thing happens on the left of Equation 18. Here I am multiplying a 5 x 2 matrix by a 2 x 1 matrix. Again we see that the '2's 'disappear' leaving us with a 5 x 1 matrix. That is, to multiply an i x j matrix by an m x n matrix, j must equal m, and if this is the case you end up with an i x n matrix.

Next I recall what the transpose of a matrix is. Essentially, in this operation, the rows of a matrix become its columns, and vice versa. That is, the transpose of the following 5 x 2 matrix:

(20) $$\begin{pmatrix} 0 & 1 \\ 0.9 & 1 \\ 2.2 & 1 \\ 3.0 & 1 \\ 4.1 & 1 \end{pmatrix}$$

is following 2 x 5 matrix:

(21) $$\begin{pmatrix} 0 & 0.9 & 2.2 & 3.0 & 4.1 \\ 1 & 1 & 1 & 1 & 1 \end{pmatrix}$$

So I can see from this example that if we transpose an i x j matrix we get a j x i matrix.

Now we use the following elegant trick. We will left multiply both sides of Equation 19 by the transpose of matrix X: X^T:

(22) $X^TY = X^TXM$

and notice in this process that the product of X^T with X will be a square matrix (a square matrix always has equal number of columns and rows). And while it is true that not all square matrices have inverses, only square matrices have inverses, so this trick provides me with a way of moving forward. Accordingly, the inverse of X^TX, assuming it exists, will be represented as $(X^TX)^{-1}$. Thus, I left multiply both sides of Equation 22 by this matrix to get:

(23) $(X^TX)^{-1}X^TY = (X^TX)^{-1}X^TXM$

which, again assuming (X^TX) has an inverse, reduces to the solution of Equation 19:

(24) $(X^TX)^{-1}X^TY = M$

So plugging the matrices in Equation 18 into Equation 24 and running the appropriate operations on them gives: m = 0.9472 and b = 0.0676. If you are not familiar with this mathematics it would probably be a good idea for you to solve this problem. This fit line (y = mx + b) is shown in Figure A.1. It is significant that it is the same I would have obtained using the standard least squares procedure taught in analytical chemistry courses.

A.5. Extending this Procedure to a Polynomial

So far I have only considered linear systems. Now, what if I wished to fit a set of data points to a polynomial, e.g., $y = ax^2 + bx + c$. How could I do this? I'd basically use the same procedure I just discussed. For the points (x_1, y_1), (x_2, y_2), etc., I would first write:

(25) $y_1 = ax_1^2 + bx_1 + c$

(26) $y_2 = ax_2^2 + bx_1 + c$

etc.

I would then reformulate these equations into a matrix algebra problem as I did before:

(27) $$\begin{pmatrix} y_1 \\ y_1 \\ \dots \end{pmatrix} = \begin{pmatrix} x_1^2 & x_1 & 1 \\ x_2^2 & x_2 & 1 \\ \dots & \dots & \dots \end{pmatrix} \begin{pmatrix} a \\ b \\ c \end{pmatrix}$$

If I have more than three data points to fit, the matrix on the right side of Equation 27 will not be square. However, following the procedure used in the previous section, I can still manipulate Equation 27 so that I end up with an Equation like Equation 24 that will give us the values of a, b, and c. Obviously these principles also apply to fitting with higher order polynomials as well as to fitting to equations with fewer parameters. That is, if I had desired to fit our data to $y = ax^2$, I would have reformulated the problem as:

(28) $y_1 = ax_1^2$

(29) $y_2 = ax_2^2$

etc. to obtain:

(30) $$\begin{pmatrix} y_1 \\ y_1 \\ \dots \end{pmatrix} = \begin{pmatrix} x_1^2 \\ x_2^2 \\ \dots \end{pmatrix} (a)$$

For n pairs of x,y values, I would then have an n x 1 matrix on the right side of Equation 30. I could still follow the general approach outlined herein and multiply it by its transpose: a 1 x n matrix, which will allow us to find the parameter a.

A.6. Comparing/Fitting the 1s Binding Energies of the Elements to Bohr's Theory, AZ^2, and $AZ^2 + BZ + C$

Figure A.2 contains a plot of the binding energies (circles) of the 1s electrons of the Z = 1 – 92 elements, as obtained from the literature.[5-8] As expected, these binding energies increase monotonically with increasing nuclear charge, i.e., it becomes progressively harder to remove an electron from an atom with more and more protons. Here I compare these experimental binding energies to (i) the values predicted by Bohr's theory (Equation 1 with n = 1), (ii) a semiempirical fit with one adjustable parameter: AZ^2, and (iii) a semiempirical fit with three adjustable

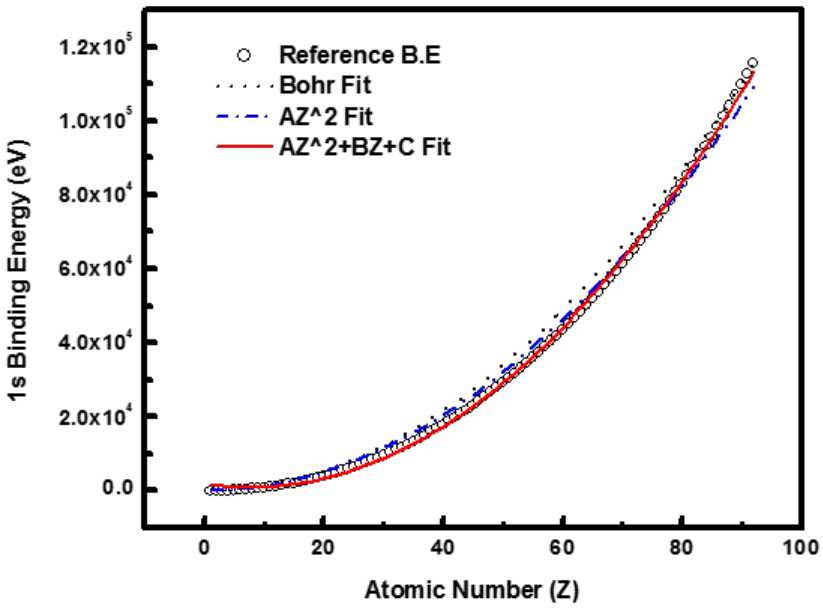

Figure A.2. Binding energies of the 1s electrons in the elements with Z = 1 to 92. The black dotted line represents the $-13.6Z^2/n^2$ (n = 1 for the 1s electrons) predictions from Bohr's theory. The dashed line represents a one-parameter Z^2 model, and the solid red line represents a three-parameter Z^2 model.

parameters: $AZ^2 + BZ + C$. A few things are obvious here. First, Bohr theory does not explain the data. It isn't supposed to. Second, however, the Bohr fit is 'in the ballpark'. It fits the data reasonably well at lower and higher Z values, and moderately in between. The semiempirical AZ^2 and $AZ^2 + BZ + C$ fits then seems to be an improvement over the Bohr results, and, as expected, the equation with the largest number of adjustable parameters appears to give the best fit.

Figure A.3 shows the $2p_{1/2}$ binding energies of the elements[5-8] from Z = 10 - 92 and three fits to this data: the Bohr equation (for n = 2), AZ^2, and $AZ^2 + BZ + C$. In this case, Bohr's theory does a very poor job of estimating the experimental results, significantly overestimating them. Part of the reason for this overestimation is no doubt the fact that Bohr theory does not take into account the screening of the nucleus by inner shell electrons, i.e., the 1s electrons here. The AZ^2 equation then does a moderately good job of fitting the experimental results, and the three parameter $AZ^2 + BZ + C$ equation fits the data reasonably well. While it is clear that Bohr theory no longer provides a good estimate of the experimental values, the fact that the three-parameter semiempirical equation fits the data as well as it does points again to a general Z^2 dependence of the electron binding energies, which can be viewed as being generally consistent with Bohr's theory.

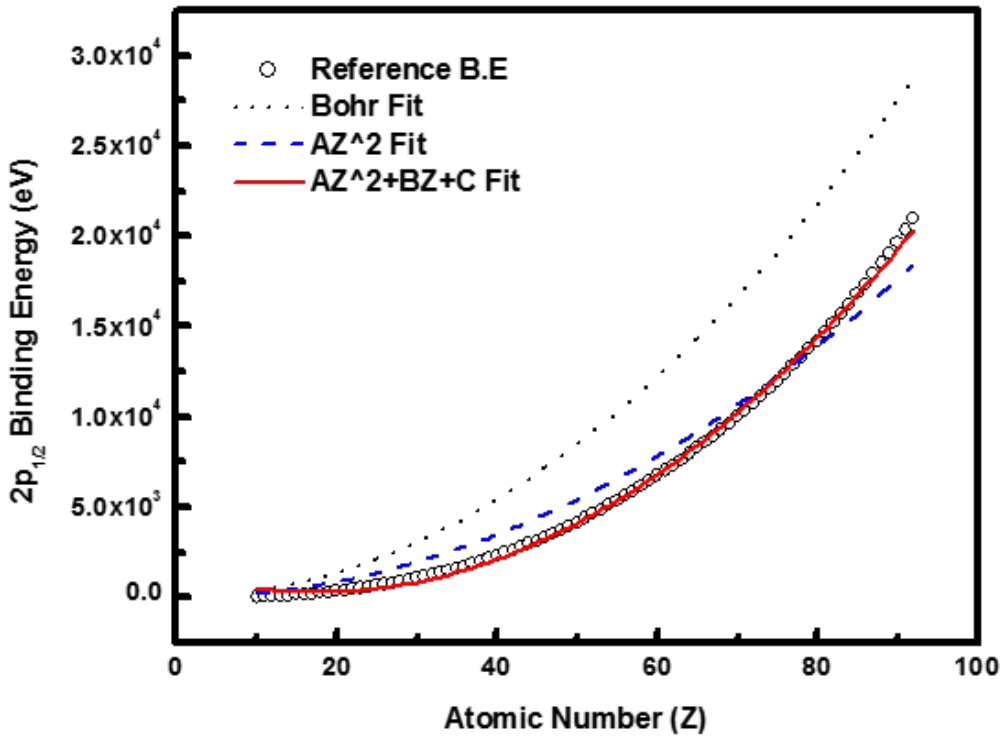

Figure A.3. Binding energies (open circles) of the $2p_{1/2}$ electrons in the elements with Z = 10 to 92. The dotted line represents the $-13.6Z^2/n^2$ (n = 2 for the $2p1_{/2}$ electrons) predictions from Bohr's theory. The dashed line represents a one-parameter Z^2 model, and the solid red line represents a three-parameter Z^2 model.

A.7. References

1. Bohr, N., I. On the constitution of atoms and molecules. *The London, Edinburgh, and Dublin Philosophical Magazine and Journal of Science* **1913,** *26* (151), 1-25.

2. Kragh, H., Before Bohr: Theories of atomic structure 1850-1913. *RePoss: Research Publications on Science Studies* **2010,** *10*.

3. Pauling, L.; Wilson Jr, E., Introduction to Quantum Mechanics, with Applications to Chemistry, 1935. Dover, New York.

4. Alford, T. L.; Feldman, L. C.; Mayer, J. W., *Fundamentals of nanoscale film analysis*. Springer: 2007; Vol. 1.

5. Williams, G. P., X-ray data booklet. *X-RAY DATA BOOKLET* **2001**.

6. Bearden, J.; Burr, A., Reevaluation of X-ray atomic energy levels. *Reviews of Modern Physics* **1967,** *39* (1), 125.

7. Cardona, M.; Ley, L., Photoemission in solids I. *Photoemission in Solids I: General Principles* **1978,** *1*.

8. Fuggle, J. C.; Mårtensson, N., Core-level binding energies in metals. *J. Electron Spectrosc. Relat. Phenom.* **1980,** *21* (3), 275-281.

Appendix B: Abbreviations

Abbreviation	Definition
AFM	Atomic force microscopy
APTES	(3-aminopopyl)triethoxysilane
Au(111)	Gold surface prepared by depositing 10-20 nm of chromium followed by 200 nm of gold on a piece of silicon wafer.
Au-S	Gold-sulfur
Bi	Bismuth metal
BPT	1,1'-biphenyl-4-thiol
CVD	Chemical vapor deposition
DNA	Deoxyribonucleic acid
DNA-SH	Thiolated DNA
DNA-S-S-DNA	Thiolated DNA molecules that have formed disulfide linkages.
DTT	Dithiothreitol
EtOH	Ethanol
HDT	1,6-hexanedithiol
HDT/Au	Gold surface functionalized with HDT SAM.
ITO	Indium tin oxide
LBL	Layer-by-layer
MetA-SIMS	Metal assisted secondary ion mass spectrometry
MPTMS	3-mercaptopropyltrimethoxysilane
MPTMS/SiO2/Si	Silicon wafer functionalized with MPTMS
NBPT	4'-nitro-1,1'-biphenyl-4-thiol
NP	Nitrilotris(methylene)triphosphonic acid
ODT	Octadecanethiol
ODT/Au	Gold surface functionalized with ODT SAM.

P/N	Phosphorus/Nitrogen
PAA	Polyacrylic acid
PAH	Polyallylamine hydrochloride
PAH/PAA	LBL assembly of alternating layers of PAH and PAA.
(PAH/PAA)nPAH	PAH-terminated PAH/PAA assemblies.
PBd	1,2-polybutadiene
PBd/HDT/Au	HDT/Au surface functionalized with PBd.
PBd/MPTMS/SiO2/Si	MPTMS/SiO2/Si surface reacted with PBd.
PCA	Principal component analysis
PDADMAC	Polydiallyldimethylammonium chloride
PDDT	1H,1H,2H,2H-perfluorododecanethiol
PDDT/PBd/HDT/Au	PBd/HDT/Au surface functionalized with PDDT
PDT	1H,1H,2H,2H-perfluorodecanethiol
PDT/Au	Gold surface functionalized with PDT SAM.
PDT/PBd/HDT/Au	PBd/HDT/Au surface functionalized with PDT
PEG	polyethylene glycol
PFO	Perfluorooctane
PI	Primary ion
PID	Proportional-integral-derivative
QCM	Quartz crystal microbalance
RSD	Relative standard deviation
-S-	Thiolate
SAM	Self-assembled monolayer
SAMs	Self-assembled monolayers
SE	Spectroscopic ellipsometry
Si/SiO2	Silicon wafer
SiO2/Si	Silicon Wafer

TCEP	tris(2-carboxyethyl)phosphine
TEA	Triethanolamine hydrochloride
THF	Tetrahydrofuran
ToF-SIMS	Time-of-flight secondary ion mass spectrometry
TPDMT	[1,1';4',1"-terphenyl]-4,4''-dimethanethiol
UV	Ultraviolet
XPS	X-ray photoelectron spectroscopy